OPTIMIZATION OF A MAGNETOPLASMADYNAMIC ARC THRUSTER

by

Matthew Joseph Krolak

A Thesis

Submitted to the Faculty

of the

WORCESTER POLYTECHNIC INSTITUTE

in partial fulfillment of the requirements for the

Degree of Master of Science

in

Electrical Engineering

by

Matthew Krolak   4/26/07

May 2007

APPROVED:

A. Emanuel

Professor Alexander E. Emanuel, Thesis Advisor

Robert Labonté

Professor Robert C. Labonté, Committee Member

Sergey Makarov

Professor Sergey N. Makarov, Committee Member

I

DEDICATION

To Dad

ABSTRACT

As conventional chemical rockets reach the outer limits of their abilities, significant research is going into alternative thruster technologies, some of which decouple the maximum thrust and efficiency from the propellant's internal chemical energy by supplying energy to the propellant as needed. Of particular interest and potential is the electrically powered thruster, which promises very high specific thrust using relatively inexpensive and stable propellant gasses. Some such thrusters, specifically ion thrusters, have achieved significant popularity for various applications. However, there exist other classes of electrical thrusters which promise even higher levels of efficiency and performance.

This thesis will focus on one such thruster type – the magnetoplasmadynamic thruster – which uses an ionized propellant flow and large currents to accelerate the propellant gas by electrical and magnetic force interactions. The necessary background will be presented in order to understand and characterize the operation of such devices, and a theoretical model will be developed in order to estimate the levels of performance which can be expected. Simulations will be performed and analyzed in order to better understand the principles on which these devices are designed.

Finally, a thruster package will be designed and built in order to test the performance of the device and accuracy of the model. This will include a high-current power supply, ignition circuit, gas delivery system, and nozzle. Finally, the measured performance of this thruster package will be measured and compared to the theoretical predictions in order to validate the models constructed for this type of thruster.

ACKNOWLEDGEMENTS

I would like to acknowledge and thank everyone whose support, contributions, and advice made this project an interesting and worthwhile experience. In particular I would like to thank my thesis advisor Professor Emanuel, who's years of friendship and tutelage I have benefited from immeasurably. Under his supervision I have been able to investigate many subjects of personal interest above and beyond what might be expected to be included in a typical electrical engineering education. I am extremely grateful for the experience and the opportunity to have worked with him for so long.

I would also like to thank Rob Doughty for his inspiration that lead to such an unexpected and thoroughly enjoyable academic endeavor. It seems unlikely that I would have come upon the idea for this project except for his interest in the subject.

Finally I would like to thank my friends and family for their support understanding of the long hours in the lab that were needed to accomplish this work.

TABLE OF CONTENTS

LIST OF FIGURES

LIST OF SYMBOLS

All units are MKS unless otherwise noted. Pressure is in atmospheres, temperature is in Kelvin, and gaseous quantities are in moles.

a	Area, Radius
A	Acceleration, Constant, $6.02 \times 10^5 \ A/(m^2 \cdot K^2)$
A_{arc}	Arc cross-sectional area
b_o	Constant, $\phi_0 e/k$
B	Magnetic flux density
B_0	Inlet magnetic flux density
c	Ratio of velocity to most probable velocity
c_p	Constant pressure specific heat
c_0	Most probable velocity
$\bar{c}$	Average velocity
C	RMS velocity
C_1	Constant
C_2	Constant
C_3	Constant
d	Distance, Mean free path
e	Charge of an electron $= 1.602 \times 10^{-19} C$
e_a	Arc voltage
e_{column}	Positive column voltage
e_i	Voltage due to ionization
ε_i	Ionization energy
ε_0	Dielectric permittivity of free space $8.854 \times 10^{-12} \ F/M$
E	Electric field
$E_{\perp}$	Perpendicular electric field
E'	Effective electric field
f	Function
f_+^i	Internal part of positive ion partition function
f_+^t	Translational part of positive ion partition function
f_A^i	Internal part of neutral atom partition function
f_A^t	Translational part of neutral atom partition function
f_e^i	Internet part of electron partition function
f_e^t	Translational part of electron partition function
f_r	Radial force density
fz	Z-Axis force density
F	Force
F_+	Partition function for positive ions
F_A	Partition function for neutral atoms
F_c	Force on cathode tip

F_e	Partition function for electrons
g_0	Acceleration due to gravity at sea level
h	Planck's constant $6.626 \times 10^{-34} J \cdot s$
H_a	Anode heat
I	Impulse, Current
I_{sp}	Specific impulse
j	Current density
j_c	Cathode total current density
j_e	Electron current density
j_p	Positive ion density
J	Current
k	Boltzmann constant $1.38 \times 10^{-23} J/K$
K_e	Electron mobility
K_p	Positive ion mobility
K_n	Equilibrium ionization constant
ℓ	Length
m_0	Original mass
m_f	Final mass
$\dot{m}$	Mass flow rate
M	Mass
M^+	Mass of a positive ion
M_{AR}^+	Argon ion mass
M_{CU}^+	Copper ion mass
M_e	Mass of an electron $9.11 \times 10^{-31} kg$
Δm	Change in mass, mass increment
n	Number of particles
n_+	Number of positive ions
n_A	Number of neutral atoms
n_e	Number of electrons, Concentration of electrons
n_p	Concentration of positive ions
n_0	Total number of atoms available for ionization
Ω	Hall parameter
P	Pressure
P_A	Pressure in vessel A
P_B	Pressure in vessel B
P_c	Thermal power delivered to cathode
P_{column}	Power dissipated in the positive column
P_{ion}	Power dissipated in ionizing a gas flow
ϕ	Thermionic work function
ϕ'	Field modified thermionic work function
q	Charge of an electron
r	Radius
r^+	Average atomic radius
r_a	Anode radius
r_{AR}	Argon atomic radius

r_c^+ Cathode radius

r_{CU}^+ Copper atomic radius

R   Ideal gas constant $8.21 \times 10^{-5} \, m^3 \cdot atm / K \cdot mol$

R_p Positive column resistance

σ Stefan-Boltzmann constant $5.67 \times 10^{-8} \, W / m^2 \cdot K^4$

T   Thrust, Temperature

T_c Chamber temperature

T_e Exhaust temperature

μ_0 Magnetic permeability of free space $1.26 \times 10^{-6} \, H / m$

v   Velocity

v_0 Inlet velocity

$v_\perp$ Perpendicular velocity

v^* Dimensionless velocity

v_c Collision frequency, Chamber velocity

v_e Exhaust velocity

V   Volume

V_a Anode fall potential

V_c Cathode fall potential

Δv Change in velocity

ω Angular velocity

ω_b Plasma frequency

x^* Dimensionless position

z   Position

z_0 Inlet position

1 Introduction

The impetus for investigating such seemingly exotic methods of propulsion such as electrical plasma thrusters may not be immediately obvious, and so this introduction will help the reader gain some understanding of the physics involved in space flight, and introduce some of the basic parameters of thrusters in general. From this basic understanding, an argument for developing increasingly fuel efficient methods of generating thrust will be made, and some of the basic parameters that will be required for more aggressive missions will be set, and techniques that may be employed to that end will be explored.

1.1 Physics of Space Flight

This section follows the analysis of the physics of space flight presented in Robert G. Jahn's *Physics of Electric Propulsion* [1], and is based on the derivation of the mass fraction equation.

This analysis starts with the familiar force equation, where the imparted force is equal to the mass of an accelerated body multiplied by its acceleration

$$F = MA \quad (1\text{-}1)$$

This equation can be rewritten to represent the force imparted (thrust) to a vehicle by

$$T = \dot{m}v \quad (1\text{-}2)$$

where $\dot{m}$ is rate of mass loss (kg/s) through the thruster and v is the velocity of the expelled mass (m/s.) Therefore, the total impulse imparted to the vehicle is simply the time integral of thrust, or for constant thrust T

$$I = T\Delta t \quad (1\text{-}3)$$

with units of Ns. Assuming a constant exhaust velocity of v_e, the total change in velocity (referred to as the "delta-v") of the vehicle can be represented by as [2]

$$\Delta v = v_e \ln\left(\frac{m_o}{m_o - \Delta m}\right) \quad (1\text{-}4)$$

where m_o is the original launch mass of the vehicle, Δm is the increment of mass lost to thruster exhaust, and $m_o - \Delta m = m_f$ is the final mass of the vehicle. Rearranging this equation to the form

$$\frac{m_o}{m_f} = e^{-\frac{\Delta v}{v_e}} \quad (1\text{-}5)$$

yields an equation that relates the fraction of the original launch mass dedicated to fuel and the desired final velocity of the vehicle to the exhaust velocity of the propellant.

At the most general level a flight plan can be reduced to the three variables of the mass fraction equation: m_O/mf, Δv, and v_e. Common sense dictates that as much of the vehicle's original mass ought to be dedicated to useful payloads, whether that is cargo or passengers, and only a modest amount be dedicated to fuel. Similarly, it seems likely that short travel times corresponding to large Δv missions are preferable. Equation 1-5 indicates that the exhaust velocity of the propellant should be maintained at roughly the same order of magnitude as the desired final velocity, and therefore one of the major concerns facing engineers will be obtaining correspondingly high exhaust velocity propulsion systems.

1.2 Delta V and Fuels

Space flight mission requirements are often expressed as the total delta-v of the mission or as the total change in velocity of the vehicle as the result of thruster operation [3]. Accordingly, long distance missions or missions over extended periods of time often require relatively large delta-v. The table below shows the approximate delta-v required for several interplanetary missions [4].

Mission	$\Delta v, m/s$
Escape from Earth surface (impulsive)	11,200
Escape from 300-mile orbit (impulsive)	3,150
Escape from 300-mile orbit (gentle spiral)	7,590
Earth orbit to Mars orbit and return	14,000
Earth surface to Mars surface and return	34,000
Earth orbit to Venus orbit and return	16,000
Earth orbit to Mercury orbit and return	31,000
Earth orbit to Jupiter orbit and return	64,000
Earth orbit to Saturn orbit and return	110,000

Figure 1: Characteristic Velocity Increments

In order to increase the range of space exploration over a reasonable range of mass fractions it is apparent that these higher delta-v missions will require correspondingly high exhaust velocities.

The mass fraction equation clearly illustrates a general relationship between exhaust velocities the efficacy of the propellant used; however a more precise metric is often used to compare various propulsion systems and fuels. Specifically, the thrust imparted per unit mass of propellant, or the specific impulse, if often calculated as a property of a particular propellant and is defined as the ratio of thrust to propellant weight at sea level as [5]

2

$$I_{sp} = \frac{\dot{m} v_e}{\dot{m} g_0} = \frac{v_e}{g_0} \quad (1\text{-}6)$$

with units of seconds. Based on specific impulse, several chemical fuels are summarized below, and can be compared with the characteristic delta-v of missions [6].

Oxidizer/Fuel	Specific Impulse (s)
NO_2 / HTPB (solid)	248
N_2O_4 / Kerosene	256
N_2O_4 / Hydrazine	276
N_2O_4 / MMH	280
LOX / Kerosene	289
LOX / UDMH	297
FLOX-80 / Kerosene	320
LFL / Hydrazine	338
LOX / LH_2	381
LFL / LH_2	400

Figure 2: Specific Impulse of Chemical Fuels

Noting that specific impulse and exhaust velocity are related by a factor or g_0, even the highest specific impulse chemical fuels achieve exhaust velocities of 3,900 m/s, which correspond to only the smallest delta-v missions such as impulsive escape of Earth's gravity from a 300 mile orbit.

Further complications arise from the properties of chemical fuels beyond their limited specific impulse. Primarily, higher specific impulse implies higher reactivity and a correspondingly high rate of corrosion of thruster components. Similarly, high exhaust velocities also imply high exhaust temperatures which can reach well above the melting points of common materials, thus complicating the task of designing practical thrusters for use with these fuels. Finally, since the energy released in burning these fuels is obtained from the fuel's internal chemical energy, these high impulse fuels tend to also be relatively unstable and difficult to transport and store safely [7].

One possible solution to the difficulties of using high specific impulse propellants is to store relatively stable or inert compounds and then, at the point of use, impart some energy to the propellant. This could be implemented by using electrical energy to either heat the propellant, or to apply some electrostatic or electromagnetic force on the propellant. This alleviates the difficulties of storing highly reactive fuels, and should be relatively easy to implement considering the high electrical power levels available to space vehicles through radiothermal generators and solar panels.

This thesis will develop the theory behind electrical propulsion, present several different implementations of electrical thrusters, and finally present the design and analysis of a magnetoplasmadynamic arc thruster.

1.3 History of Electric Propulsion

The possibility of electrical space propulsion has been long recognized, starting with Robert Goddard in 1906 and Herman Oberth in 1929 though the lack of practical power sources limited any serious consideration of electrical propulsion methods until 1948 when the first feasibility studies were conducted, and even then no serious development was undertaken until the late 1950s [8]. Early developmental work focused on arcjet thrusters where electrical discharges were used to heat gasses and then expand them in conventional nozzles. This period also coincided with the development of ion engines and later resistojets and nuclear thrusters, both of which also heated gasses which were expanded in conventional nozzles.

Work on magnetogasdynamic thrusters started in the late 1960s, based on the concepts of magnetohydrodynamic thrusters, but this work stalled as the machinery required to generate programmed electric and magnetic fields in a MGD thruster channel was prohibitively large for only modest thrust levels. Later work began on magnetoplasmadynamic thrusters only after an accidental discovery whereby the flow rate and pressure in a thermal arcjet thruster was reduced to very low levels which unexpectedly resulted in very high specific thrusts. This discovery brought renewed interest to the study of the much simplified MPD thruster.

Current work on MPD thrusters is limited mostly to academic work with the notable exception of a high power MPD thruster at the NASA JPL facility. The only space application of an MPD thruster was on the Japanese satellite EPEX. The practical limitations of MPD thrusters such as electrode erosion have partially refocused research in electrical propulsion to the VASIMR type thruster which uses induced currents to avoid direct electrode contact and therefore does not suffer from electrode erosion. [9]

2 Background

The basic principles and modes of operation behind electric propulsion are probably not well understood outside of those actively studying or designed such systems, and have been considered within the generally inaccessible discipline of "rocket science", however from a few basic and fundamental principles a working understanding of moderately sophisticated thruster systems can be obtained. Presented in the following sections is a general summary, perhaps review, of those principles which will be used later to characterize and study the behavior of such thrusters.

2.1 Electrical Principles

At the most general level, electric thrusters use the interactions between charged particles to transfer momentum to a propellant stream, and thus it is important to have a good understanding of the possible forces that may be exerted between charged particle, electrical currents, and magnetic fields.

2.1.1 Coulomb Force

The Coulomb force refers to the force that charged particles exert on each other, either individually or by their combined effect as an electric field. Individually, the force that one charge feels as the result of the presence of another is give by Coulomb's Law

$$\overline{F}_{12} = \frac{1}{4\pi\varepsilon_0} \frac{q_1 q_2}{r^2} \hat{r}_{21} \quad (2\text{-}1)$$

where ε_0 is the electrical constant $= 8.988 \times 10^9 \, N \cdot m^2 \cdot C^2$

q_1, q_2 are the charges of the two particles under consideration

r is the distance from q_1 to q_2

$\hat{r}_{21}$ is the unit vector pointing from q_2 to q_1

For the force exerted on one charge as the result of many other charges, Coulomb's law can be summed for the force contribution of each charge as follows

$$\overline{F}_1 = \sum_j \frac{1}{4\pi\varepsilon_0} \frac{q_1 q_j}{r^2} \hat{r}_{j1} \quad (2\text{-}2)$$

Noting that q_1 is constant in this equation, it can be pulled to the front, and the rest of the summation can be considered the "electric field". Therefore, the force felt by a single charge is simply the product of the charge and the electric field

$$\overline{F} = q\overline{E} \quad (2\text{-}3)$$

2.1.2 Lorentz Force

The Lorentz force refers to the effects of the magnetic field resulting from the flow of current through a loop. As illustrated below, if a metal rod (thin line) is placed across two terminals (thick line) and a current flows, the magnetic field caused by the current will interact with the current flowing through the rod resulting in a force that propels the rod in the direction indicated by F.
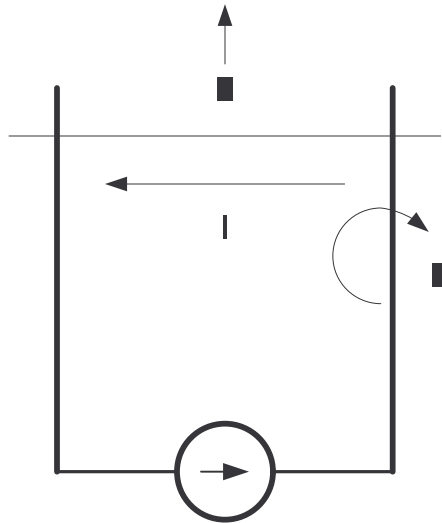
Figure 3: Lorentz Force

The resultant force is the cross product of the current and magnetic field vectors, and the force is therefore normal to the $\bar{J}$ and $\bar{B}$ plane.

$$\overline{F} = \overline{J} \times \overline{B} \quad (2\text{-}4)$$

2.1.3 Effective Electric Field

In the discussion of Coulomb forces, the electric field was defined to be the sum of all electrostatic forces per charge. This concept can be extended to include Lorentz force as well, resulting in an "effective electric field" which can be used to find the net force on a test charge. Simply summing the Coulomb and Lorentz contributions to force yields the relationship

$$\overline{E}' = \overline{E} + \overline{v} \times \overline{B} \quad (2\text{-}5)$$

The effective electric field is defined so that the force felt by a charge as a result of the electric field is defined the same as earlier

$$\overline{F} = q\overline{E}' \quad (2\text{-}6)$$

6

2.2 Distribution of Gaseous Particle Velocity

The molecules in a gas in thermal equilibrium are in a state of constant random motion, with a distribution of velocities that range from virtually stationary to relatively fast. This is expected, as elastic collisions will occur between molecule where momentum is transferred, and some molecules will increase in velocity and some will decrease [10]. In order to better characterize the behavior of gasses, it is important to understand the distribution of this random thermal velocity. Cobine derives the velocity distribution function in the same manner as Maxwell (which is referred to as a Maxwellian distribution in his honor.) The results of this derivation are presented below, though the details of the derivation are omitted.

Considering the large number of molecules in even a very small sample of gas, and that the velocity vector in equilibrium for any arbitrary molecule is equally likely to point in any direction, it can be assumed that the velocity distribution will have spherical symmetry [11]. Therefore, the distribution function in any particular direction is given as [12]

$$\frac{dN_c}{N} = \frac{4}{\sqrt{\pi}} \cdot \frac{c^2}{c_0^3} e^{-\frac{c^2}{c_0^2}} dc \quad (2\text{-}7)$$

where N is the total number of modules

N_c is the number of molecules with a particular velocity

c_0 is the most probable velocity

c is the ratio of velocity to the most probable velocity

The most probably velocity is calculated through the ideal gas law, and has been determined to be [13]

$$c_0 = \left(\frac{2kT}{M}\right)^{1/2} \quad (2\text{-}8)$$

and substituting the most probable value back into the Maxwellian distribution equation yields the following result for the velocity distribution

$$\frac{dN_c}{N} = \frac{4}{\sqrt{\pi}} \cdot \left(\frac{m}{2kT}\right)^{3/2} c^2 e^{-\frac{mc^2}{2kt}} dc \quad (2\text{-}9)$$

Some other useful relationships for this distribution are

- RMS Velocity: $C = 2.027 \times 10^{-8} \sqrt{\frac{T}{M}}$ [14]

- Average Velocity: $\bar{c} = 1.868 \times 10^{-8} \sqrt{\frac{T}{M}}$ [15]

- Pressure: $p = \dfrac{nMC^2}{3}$ [16]

Finally, the velocity of a particle with kinetic energy given in electron-volts is

$$v = \sqrt{\frac{20Ve}{3M}} \quad (2\text{-}10)$$

2.3 Ionization

Ionization refers to a process whereby an atom, molecule, or ion either has an electron removed or is split into two separately charged particles. This process is important to electric propulsion because particles that carry a charge can have forces exerted on them by electromagnetic fields and carry electrical currents, whereas neutral particles do not directly feel the effects of fields or currents. Before discussing the mechanisms involved in electrical propulsion, it is important to understand the processes that cause ionization and how charged particles behave, both on an atomic level and as a group.

At temperatures below several thousand Kelvin almost all atoms and molecules are not ionized unless acted upon by some process that causes the removal of a unit of charge. Individual ionizing events represent the transfer of energy in an increment equal to the energy necessary to break an atomic or molecular bond, resulting in charged particles of higher energy. The energies involved in ionization events are very small compared to the Joule so units of electron-volts (eV) are used, where the electron-volt represents the amount of energy an electron gains by being accelerated through a potential of 1 Volt, equal to $1.6 \times 10^{-19} J$.

2.3.1 Disassociate Events

Dissociation refers to the separation of one or more atoms from a molecule. Though not strictly related to ionization, molecular dissociation reactions can often occur along side ionization or as part of the ionization process, and therefore also need to be considered.
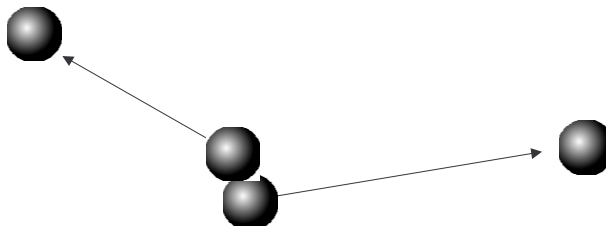
Figure 4: Dissociation

As an example, Nitrogen exists in the atmosphere not as atomic Nitrogen (N), but rather as diatomic Nitrogen (N_2). The dissociation of one diatomic N_2 molecule would yield two

free Nitrogen molecules, a process that requires $941 kJ/mol$ [17]. This bears significant relevance to the ionization of N_2, which by comparison requires $1402 kJ/mol$ [18]. Since the dissociation of N_2 requires less energy than ionization, N_2 will tend to dissociate before the individual Nitrogen molecules will ionize and thus fully ionizing N_2 will require more than twice the energy of ionizing the same mass of monatomic Nitrogen.

2.3.2 Ionization Energy

When an electron stores enough energy it may be elevated into an orbit around the nucleus which is sufficiently high such that the electron is no longer bound to the atom. Having then lost an electron, the atom becomes charges and is ionized. This can occur either in discrete steps, where the electron enters increasingly higher atomic orbitals until it is freed from the atom, or in a single transfer of energy. The total increment of energy required to free an electron is referred to as the ionization energy. Below is a simplified Grotrian diagram of the electron energy levels for Helium and Cesium [19].
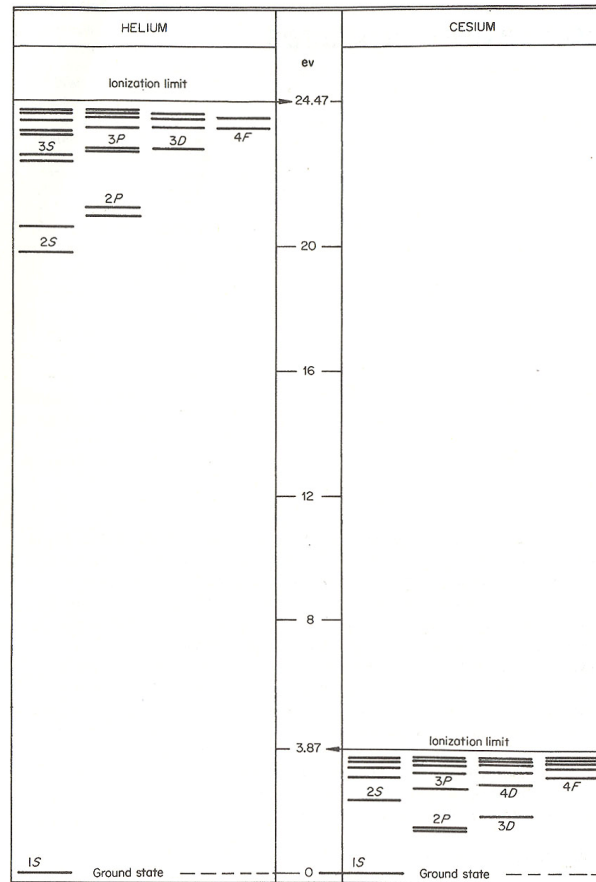
Figure 5: Grotrian Diagram

This type of diagram shows all of the available energy states which electrons may occupy for a particular atomic species. When all of the atom's electrons are in their lowest energy

orbitals the atom is in its ground state, represented as 0 eV. The energy of atoms with excited electrons is measured against this state by the total internal energy possessed by the atom above the ground level state.

2.3.3 Ionization Events

Due to the large number of energy transfer mechanisms that work on an atomic level, particles can be ionized by a number of different interactions. One possible interaction is the collision, where two particles come sufficiently close to each other that they are influenced by each others' atomic forces. This collision can either be elastic or inelastic, where collisions between particles of energies below a certain level will be deflected with no transfer of momentum (elastic collision) or the collision energy will exceed the threshold and one particle will transfer some of its energy to the other (inelastic collision.) [20]
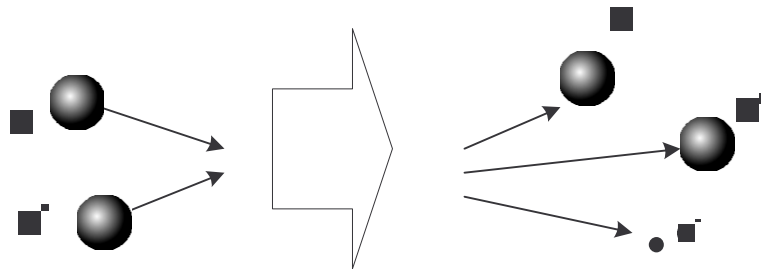
Figure 6: Atomic Collisions

In this case, only the inelastic collision will be able to cause ionization since it is the only collision where any energy is transferred.

Atoms and molecules can also become ionized by the presence of a sufficiently strong electric field. In this type of interaction, the electrons and protons of the atom feel Coulomb forces in opposite directions along the electric field lines [21]
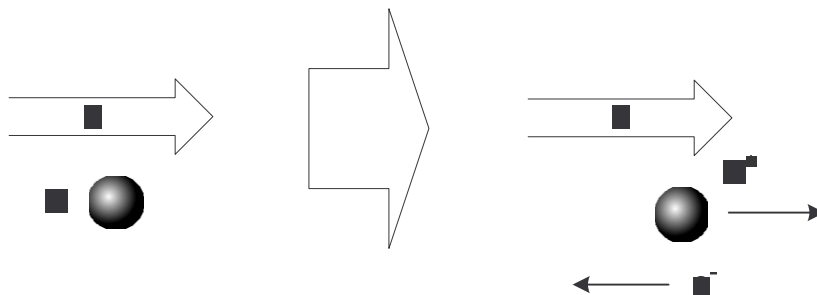
Figure 7: Field Ionization

If the field strength exceeds a certain limit then an electron can be extracted and ionization will occur. This interaction usually occurs in stages, where the most weakly bound electron is extracted first with an associated energy of first ionization, and then the

second, third, etc. electrons are extracted by increasingly strong fields with increasing energies of ionization.

Ionization can also be caused by electromagnetic radiation in the form of incident photos, referred to as photoionization. In this case, an electron can absorb the energy of a photon and assume an excited atomic orbital [22]
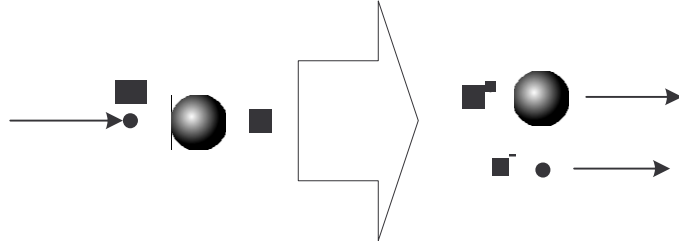
Figure 8: Photoionization

Again, this process can occur in discrete steps to higher orbitals by absorbing several low energy photos, or in one step by a sufficiently energetic photon.

Another ionizing mechanism is charge exchange. This occurs when an ionized particle collides with a neutral particle, and the charge of the ionized particle is transferred to the neutral particle [23].
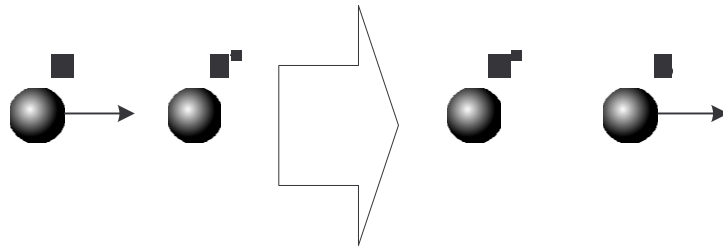
Figure 9: Charge Exchange Ionization

2.3.4 Recombination Events

Recombination events represent the reverse reactions of ionizing events, whereby molecules, atoms, ions, or electrons recompose into neutral particles. In some cases, the products of recombination are able to ionize other particles.

Radiative recombination occurs when an energetic free electron is captured into the orbit of a positive ion and results is the emission of a photon. The emission of a photon at a particular wavelength represents a loss of energy, which corresponds to the energy the electron looses as it falls into lower energy atomic orbits. This photon may have enough energy to cause photoionization elsewhere [24].
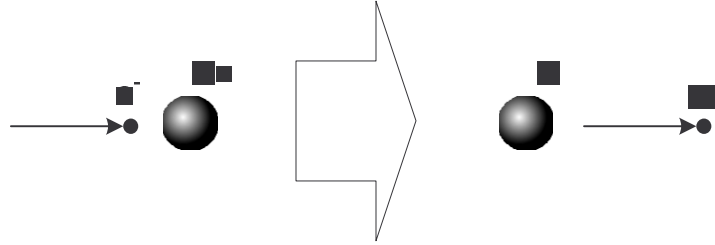
Figure 10: Radiative Recombination

Dielectric recombination is similar to radiative recombination in that an energetic free electron is captured into the orbit of a positive ion except that in dielectric recombination no photon is emitted. Rather, the energy corresponding to the free electron is retained by the atom. This hyper energetic atom may later collide and ionize another particle [25].
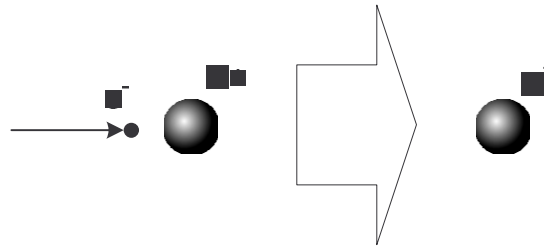
Figure 11: Dielectric Recombination

Dissociative recombination also involves the capture of an energetic free electron into a positive ion, however in this case the ion is not monatomic and the charge neutralization caused by the electron allows individual atomic species to separate [26].
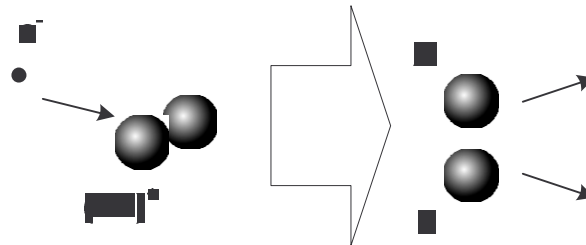
Figure 12: Dissociative Recombination

2.3.5 Cross-Section of Interception

The ionization and recombination processes in the two previous sections, as well as non-reactive collisions, describe reactions that occur when particles become sufficiently close to exchange energy. Such interactions are often represented as collisions of solid bodies; however this simplification obscures some of the subtlety of these interactions by assuming a fixed sphere of influence in which any particular interaction can occur. For

example, the inelastic collision of two neutral particles may roughly approximate the collision of solid bodies sized on the order of their outer electron shells, however an electron-positive ion collision may occur when the two bodies are significantly further apart due to their electrostatic attraction.

The distance over which each interaction occurs can be modeled by assigning a certain cross-sectional area to that interaction, where any particle that passes through that cross section, whether due to random thermal motion or outside acceleration, can be said to have collided.
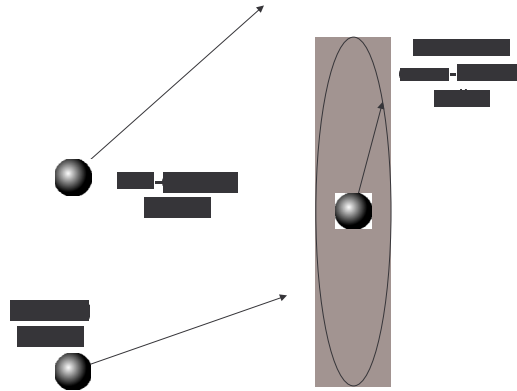
Figure 13: Cross-Section of Interception

By making certain simplifying assumptions about the motion of a particular concentration of particles it is possible to use this notion of cross-section of interception to estimate the probability of a collision occurring over a certain distance. First, it is assumed that all other particles in the volume under consideration are stationary, of the same species, and do not interact with each other. Second, it is assumed that a single particle enters the volume under consideration at a certain velocity and that it is not accelerated by any external forces. It is also assumed that the particles behave as an ideal gas. Finally, it is assumed that the trajectory of the moving particle is a straight line [27].

Given these assumptions it is possible to derive the probability of the moving particle intersecting another particle's cross-section of interception over a particular distance. Using the ideal properties of the gas, the density of particles can be expressed as a function of pressure and temperature using the following equation

$$\frac{P}{RT} = \frac{n}{V} \quad (2\text{-}11)$$

where P is the pressure in ATMs
V is volume in m^3
n is the number of particles
R is the ideal gas constant
T is temperature in Kelvin

A given type of interaction will have a certain-cross sectional area (a) of interaction associated with it. Therefore, the percentage of cross-sectional area which is free from

obstruction is $(1-a/A)^n$, where n is the total number of particles contained in the volume and A is the cross-sectional area of the volume under consideration. For simplification, A will be taken to be 1 m^2. By noting that the number of particles contained per unit volume is given by the particle density multiplied by the linear displacement, the overall probability of a collision is given by the equation

$$f(P,T,a) = 1 - (1-a)^{\left(\frac{P \cdot l}{R \cdot T} \cdot 6.02 \times 10^{23}\right)} \quad (2\text{-}12)$$

where a is the cross-section of interaction in m^2

$\quad\quad$ l is the displacement of the particle

As an example, Argon at S.T.P. has a density of 40.6 moles per m^3 (2.44×10^{25} Argon atoms per m^3). Assuming a cross-section of interception for neutral-neutral elastic collisions to be equal to a circular area with twice the radius of a single Argon atom (r = $1.42 \times 10^{-10} m$ [28], a = $6.33 \times 10^{-20} m^2$) a neutral Argon atom traveling a distance of 1m through Argon gas at STP is virtually guaranteed to collide. The cumulative distribution function for Argon at STP is shown below.
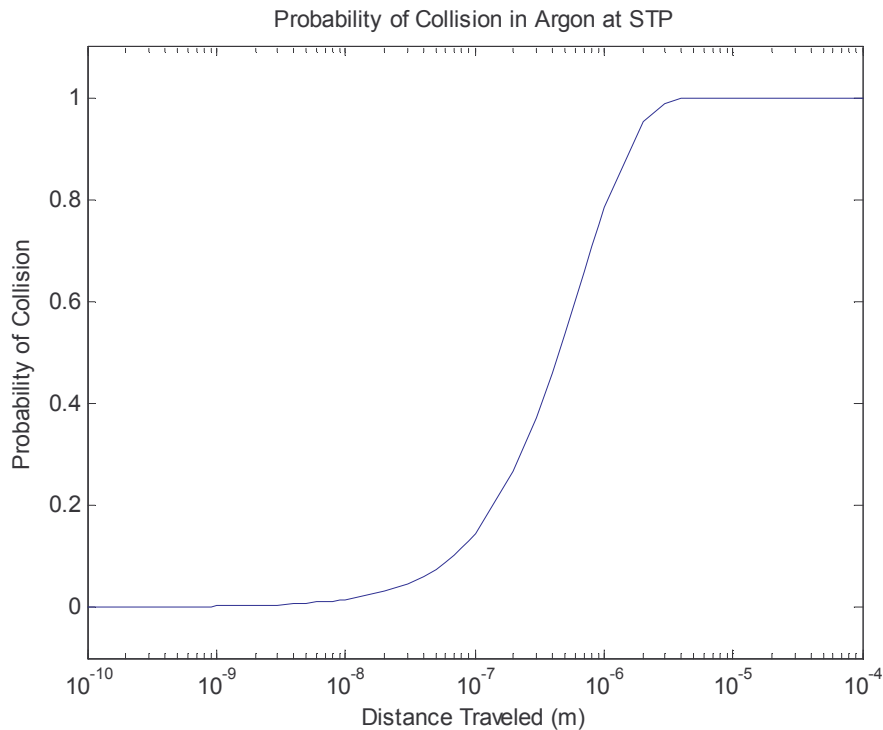
Figure 14: Probability of Collision in Argon at STP

From this estimate it is clear that collisions are unlikely if the distance traveled is less than roughly 10nm, and that a collision is virtually assured if the particle travels more than 3um.

2.3.6 Mean Free Path

The cross-section of interception analysis suggests at another useful parameter of gaseous motion. Looking at the cumulative probability function for a certain gaseous species suggests that there is some mean distance over which an "average" particle in motion will travel before experiencing a collision. Cobine derives this mean free path between collisions in *Gaseous Conductors*, and his analysis is presented as follows.

Cobine extends the concept of a cross-section of interception to a volume of interception, where a particle of some velocity v will sweep out a certain volume in 1 second of motion "equal to the product of the molecule's cross-sectional area and the velocity. A molecule in whole or in part within this volume would be struck by the moving particle." [29] Using the same assumptions presented for the cross-section of interception analysis, the area associated with the moving particle is $4\pi r^2$, and the volume will be $4\pi r^2 v$. Given a particle concentration of n the number of collisions will be $4\pi r^2 vn$ and the number of collisions per second will be the number of collisions divided by the particle velocity equal to a mean free path between collisions given by [30]

$$\ell = \frac{1}{4\pi r^2 n} \quad (2\text{-}13)$$

This equation must be modified for an electron due to its considerably smaller cross-section. In the case of the electron, the cross section is simply that of the intercepting particles, resulting in an m.f.p. given by [31]

$$\ell = \frac{1}{\pi r^2 n} \quad (2\text{-}14)$$

Cobine also notes that this equation is only an approximation since all of the particles in the system are in motion, and that this considerably complicates the analysis if a more precise calculation is required. Similarly, the velocities of the gas particles will not have one velocity; rather they will have a Maxwellian distribution of velocities.

2.3.7 Distribution of Free Paths

Since the collisions that define the mean free path are random events with a certain distribution, the exact distance traveled before a collision occurs will also be random with a certain distribution related to the mean free path [32]. Cobine derives this expressive in *Gaseous Conductors*, and is presented here without details of the derivation. The expression for the distribution of free paths is given as [33]

$$n = N\varepsilon^{-\frac{x}{L}} \text{ (2-15)}$$

where n is the number of free paths of a certain length
N is the total number of particles under consideration
x is the length of the free path under consideration
L is the mean free path for the gas under consideration

2.3.8 Equilibrium Ionization

When the forward ionization processes are exactly balanced by their reverse processes an ionized gas is said to be in equilibrium ionization. Such a reversible reaction, for example the inelastic ionizing collision of two Argon atoms, can be expressed as follows [34]

$$Ar + \tilde{Ar} \Leftrightarrow Ar + Ar^+ + e \text{ (2-16)}$$
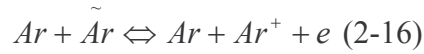
Since this process is assumed to have reached equilibrium, it can be assumed that the relative proportion of each species (neutral, positive ion, electron) is constant, and can be assigned an equilibrium constant (K_n) as follows [35]

$$K_n = \frac{n_+ n_e}{n_A} \text{ (2-17)}$$

where n_+ is the number of positive ions
n_e is the number of electrons
n_A is the number of neutral atoms
Furthermore, the equilibrium constant can also be expressed as a sum of the available energy states, i.e. by the ratio of total partition functions [36].

$$K_n = \frac{n_+ n_e}{n_A} = \frac{F_+ F_e}{F_A} \text{ (2-18)}$$

2.3.8.1 Partition Functions

From the previous section it has been shown that the equilibrium constant for a monatomic gas can be computed as the ratio of the partition functions for the various species found in the ionized gas. The partition function is then the product of a translational and internal portion [37]

$$F_A = f_A^T \cdot f_A^i \text{ (2-19)}$$

where the translational portion is defined as [38]

16

$$f_A^T = \frac{\left(2\pi M_A kT\right)^{\left(\frac{3}{2}\right)}}{h^3} \quad \text{(2-20)}$$

where M_A is the mass of the atom

k is Boltzmann's constant ($1.38 \times 10^{-12} \ J/K$)

T is temperature in Kelvin

h is Planck's constant ($6.626 \times 10^{-34} \ J \cdot s$) [39,40]

and the internal partition function is defined as [41]

$$f_A^i = \sum_j g_j e^{-(e_i/kT)} \quad \text{(2-21)}$$

The partition function for positive ions is defined in the same manner, except that the absolute ground state energy level must differ by the ionization potential [42,43].

$$F_+ = f_+^T f_+^i = \frac{\left(2\pi M_+ kT\right)^{\left(\frac{3}{2}\right)}}{h^3} \cdot \sum_j g_j e^{-\left(e_i^+/kT\right)^i} \quad \text{(2-22)}$$

Similarly, the partition function for an electron is defined only by a translational part multiplied by 2 for spin degeneracy [44].

$$F_e = 2 f_e^T = 2 \cdot \frac{\left(2\pi M_e kT\right)^{\left(\frac{3}{2}\right)}}{h^3} \quad \text{(2-23)}$$

Therefore, by substitution of the partition functions back into the equilibrium constant equation the equilibrium constant can be defined as [45]

$$K_n = 2 \cdot \frac{\left(2\pi M_e kT\right)^{\left(\frac{3}{2}\right)}}{h^3} \cdot \frac{\sum_j g_j e^{-\left(ei^+/kT\right)^i}}{\sum_j g_j e^{-(ei/kT)}} \cdot e^{-(ei/kT)} \quad \text{(2-24)}$$

2.3.8.2 Saha Equation

The Saha equation relates the degree of ionization of an ideal gas to its pressure and temperature, providing a useful tool in analyzing ionized gasses. The Saha equation is derived by substituting several other gas and plasma relations into the equilibrium constant equation. First, the degree of ionization is related to the concentration of ions in the plasma (based on charge neutrality where $n_e = n_+$) such that [46]

$$\alpha = \frac{n_+}{n_A + n_+} = \frac{n_+}{n_0} \quad (2\text{-}25)$$

where α is the degree of ionization

n_+ is the concentration of positive ions

n_A is the concentration of neutral ions

n_0 is the total concentration of atoms available for ionization [47]

Next, an equation of state for an ideal gas is defined as [48]

$$p = (n_e + n_+ + n_A)kT = (1+\alpha)n_o kT \quad (2\text{-}26)$$

Noting that

$$K_n = \frac{n_+ n_e}{n_A} = \frac{\alpha^2}{1-\alpha^2} \quad (2\text{-}27)$$

and substituting 2-25 into , 2-28 the Saha equation is determined to be [49]

$$\frac{\alpha^2}{1-\alpha^2} = \frac{2(2\pi M_e)^{3/2}(kT)^{5/2}}{ph^3}\left(\frac{f_+^i}{f_A^i}\right)e^{-(e_i/kT)} \quad (2\text{-}28)$$

The Saha equation can be simplified by noting that, since the neutral atoms and ions remain largely in their respective ground states, the ratio of the internal partition functions is effectively constant, and the equation can be rewritten as [50]

$$\alpha \approx Gp^{-1/2}T^{5/4}e^{-(e_i/2kT)} \quad (2\text{-}29)$$

where G collects all of the constant terms including the ratio of internal partition functions as shown below.

$$G = \sqrt{\frac{2(2\pi M_e)^{3/2}k^{5/2}}{h^3}\left(\frac{f_+^i}{f_A^i}\right)} \quad (2\text{-}30)$$

At lower temperatures where the degree of ionization is much lower than 1, this equation can be further simplified to [51]

$$\alpha \approx G'n_0^{-1/2}T^{3/4}e^{-(e_i/2kT)} \quad (2\text{-}31)$$

2.3.8.3 Saha Equation for Argon

Determining the degree of ionization for a gas, such as Argon, at a particular temperature and pressure for the simplified Saha equation in 2-32 first requires the constant G to be evaluated. Collecting all of the known constants gives G in a form only dependant on the ratio of the internal partition function of the positive ions and neutral atoms

$$G = \sqrt{\left(2.106 \times 10^{26}\right)\left(\frac{f_+^i}{f_A^i}\right)} \quad (2\text{-}32)$$

The internal part of the ground state atom partition function is evaluated as presented in 2-22, which requires knowledge of all of the internal electron energy levels and their degeneracies. Though weakly dependant on gas temperature, the partition function ratio has been calculated elsewhere, and will be taken as 5.2 for the purposes of this calculation. Additional information is presented in Ratio of Partition Functions for Argon [in the appendix. Therefore, the ionization for Argon at relatively low temperatures is

$$\alpha \approx \left(3.32 \times 10^{13}\right) p^{-1/2} T^{5/4} e^{-(e_i/2kT)} \quad (2\text{-}33)$$

where e_i is the ionization energy. Graphing the Saha equation for Argon across a wide range of temperatures requires the use of the full equation, yielding
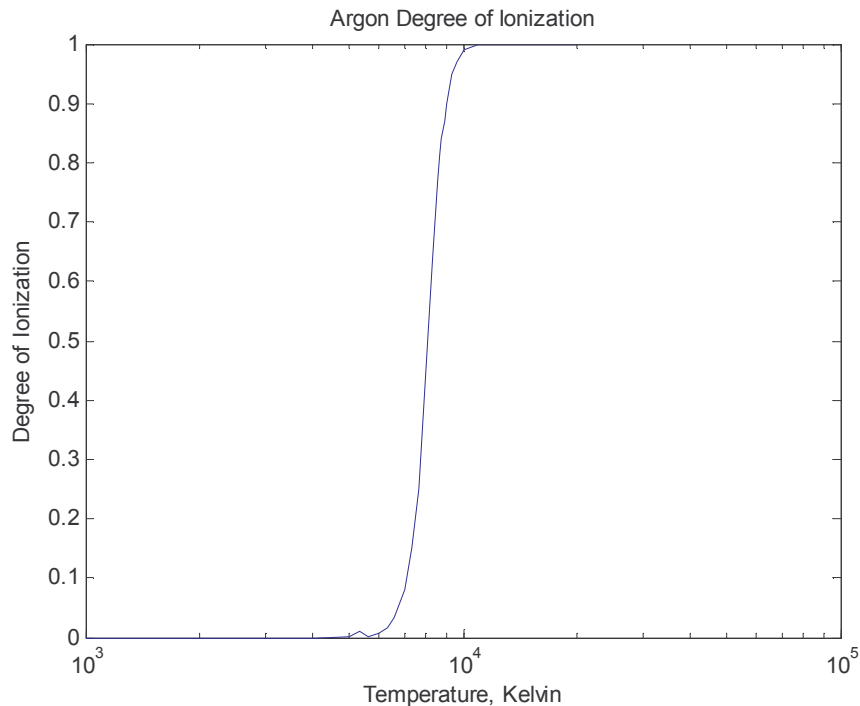
Figure 15: Degree of Argon Ionization

2.3.9 Thermionic Emissions

Thermionic emission is the processes of heated solids emitting electrons. A common application of this phenomenon is the cathode ray tube, where a filament is heated by passing a current through it to such a point where the surface of the filament begins emitting electrons toward an anode. Accordingly, this phenomenon is important in any situation where plasma comes in contact with a containing wall as the wall will heat up to a point where it too may emit electrons that contribute to the current sustaining the plasma.

Cobine presents an equation derived by Dushman [52] which relates the saturation current density of a thermionic emission as

$$j = AT^2 e^{-b_0/T} \quad (2\text{-}34)$$

where A is a constant $= \dfrac{2\pi M_e k^2}{h^3} = 6.02 \times 10^5 \, A \cdot m^{-2} \cdot K^{-2}$

b_0 is a constant $= \dfrac{\phi_0 e}{k}$ where ϕ_0 s the thermionic work function of the surface [53]

A table of A and b_0 is presented in the appendix.

2.3.10   Field Emissions

Increasing the voltage between a thermionic cathode and an anode will increase the current until it reaches its saturation current, given by the thermionic emission saturation equation. However, the current will continue to increase if the voltage across the electrodes is increased far beyond its saturation value. This is due to the ability of a sufficiently high electrostatic field to remove electrons from the surface of the metal, also known as the Schottky effect [54].

In the case of field emissions, the electric field at the cathode's surface assists the electrons in leaving the surface, and effectively lowers the surface's work function. The new work function for the surface becomes [55]

$$\phi' = \phi - \sqrt{eE} \quad (2\text{-}35)$$

This result can be substituted direly into the thermionic emission current density equation with the resulting equation for current density including field effects, known as the Schottky equation [56].

$$j = AT^2 e^{-\dfrac{\left(\phi - \sqrt{eE}\right)e}{kT}} \quad (2\text{-}36)$$

2.4 Electric Discharge

The electric arc represents a discharge of current, typically through an ionized gas, and is differentiated from other types of discharges (Townsend, Glow, etc.) by the fact that an electric arc is self-sustained. The conditions, process, and properties required for an electric arc will be discussed in this section.

2.4.1 Townsend Discharges

Townsend discharges are a category of "dark" non-self-sustained discharges typically occurring at very low currents, and depend on free electrons usually sourced by radiation or photoionization. With no voltage applied to a pair of electrons, free electrons will diffuse equally in all directions, yielding no net current. By applying a small voltage across the electrodes, the free electrons will favor moving in the direction of the anode and so some fraction of the free electrons will make it to the anode. Increasing the anode to cathode voltage will result in a larger portion of the free electrons emitted by the cathode reaching the anode, until all free electrons eventually reach the anode. At this point increasing the voltage further will not increase the current and the discharge will become saturated [57].

2.4.2 Field Intensified ionization

Though increasing the voltage above the Townsend discharge saturation point will not initially result in an increase in current, continuing to increase the voltage will eventually result in the current increasing. This effect is due to free electrons being accelerated through an increasingly strong electric field and eventually causing ionizing collisions, thus freeing more electrons that can move toward the anode. The exact form of this field-intensified ionization is covered in Cobine's *Gaseous Conductors*, but for this analysis it is sufficient that the discharge is not self-sustained because the total current is a function of the Townsend saturation current [58].

2.4.3 Glow Discharge

At some point, with increased gap voltage, the "dark" Townsend discharges will transition to a self-sustained discharge often characterized by positive ion bombardment at the cathode and electron avalanche toward to the anode. This discharge typically takes the form of either a glow discharge or an arc discharge. Though the arc discharge is more relevant to the implementation of an arc thruster, understanding the behavior of a glow discharge will illuminate later discussion on arc discharges.

At very low pressures, on the order of mmHg, glow discharges take on a pattern of alternating light and dark regions corresponding to various processes inside of the gas. In order from cathode surface to anode surface these regions are: Aston dark space, cathode glow, cathode dark space, negative glow, Faraday dark space, positive column, anode glow, and anode dark space [59]. The arrangement of these regions is illustrated below [60].
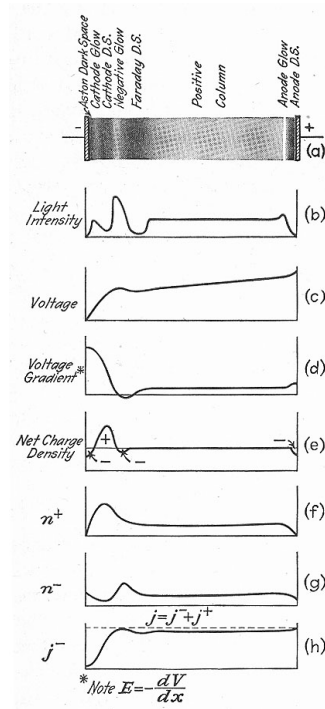
Figure 16: Low Pressure Glow Discharge Characteristics

Depending on the gas, pressure and current, the Aston and anode dark spaces may not be visible, and the anode glow may not occur [61]. Also, it is important to note that if the gas pressure is changed or the electrodes are moved, the positive column will expand and contract while the other regions remain approximately the same size. This indicates that the processes occurring near the anode and cathode are critical to the discharge while the positive column is secondary [62].

Directly adjacent to the cathode is a region of high electron concentration followed by the cathode dark space, which is characterized by large potential and high electric field strength. The presence of the electrons at the cathode is a result of the cathode being an electron emitter, and that having just been ejected from the cathode they have relatively low velocities. The cathode dark region is characterized by high positive ion concentrations which cause the large potential drop, and which originate either in the cathode dark space or the anode fall region. Toward the end of the cathode dark space the electron density increases to such a point that the electron and positive ion concentration are nearly equal, and may have total concentrations of more than 100 times that of the positive column [63]. In the Faraday dark space the electron density increases again up until the positive column where the electron and positive ion densities are again roughly equal. The positive column serves to maintain a conduction path, and has a low voltage gradient across it. The positive column terminates in the anode glow where positive ion density decreases until at the anode dark space the current is entirely carried by electrons.

2.4.4 Arc

The electric arc is a self-sustained discharged characterized by a relatively low voltage drop, which can carry very large currents, and which generally has an overall negative V/I slope [64]. The characteristics of an arc discharge are functions of the gas, electrode materials, and a strong function of gas pressure.

2.4.4.1 Low Pressure Arc

The low pressure arc is characterized by a relatively low gas temperature, on the order of a few hundred Kelvin, and a much high electron temperature – perhaps several tens of thousands of Kelvin. The transition from glow discharge to arc discharge is partially indicated by the positive column being the only visible region in the arc discharge. In the positive column, the current is carried almost entirely by electrons, though a presence of slow moving positive ions is present which serve to cancel out any space charge that would otherwise appear, and results in a very low voltage gradient across the positive column [65].

2.4.4.2 High Pressure Arc

The high pressure arc is distinguished from the low pressure arc primarily by the fact that the neutrals, ions, and electrons are in thermal equilibrium. Thermal equilibrium is typically reached at a pressure of approximately 0.03 atm, with arc column temperatures being on the order of 5000k-6000k [66] and both cathode and anode material being at their boiling points. Arc discharges are also differentiated from other discharges by the fact that only the positive column, cathode fall, and anode fall regions are present in an arc discharge, though the anode and cathode drop regions are very short and largely masked by the positive column.

The V/I characteristic of high pressure arc discharges was studied by Hertha Ayrton, who found two distinct regions of operation for carbon/air arc – the silent and hissing arcs. For relatively low current arcs she found that the V/I characteristic was represented by a hyperbolic curve for silent arcs up to the transition to hissing arcs at higher currents which had nearly linear V/I curves [67].
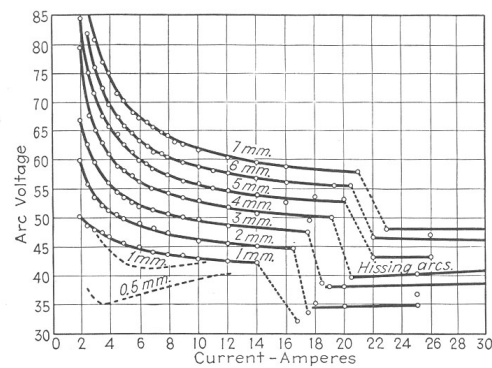
Figure 17: High Pressure Carbon Arc V/I Characteristic

23

In the silent region, Ayrton found that the curves adhered to the Ayrton equation, given as [68]

$$e_a = a + bi + \frac{c + dx}{i} \quad (2\text{-}37)$$

where a, b, c, d are constants for the particular electrode material/gas used

      x is the length of the arc

      i is the arc current in Amperes

After the transition to hissing arcs at higher currents the Ayrton equation no longer hold, and at much higher currents the V/I curve departs from a negative linear slope to a positive slope represented by [69]

$$e_a = c_1 i + \frac{c_2}{i} + c_3 i^2 \quad (2\text{-}38)$$

The distribution of the arc voltage across the gap is not linear, rather it is broken up into three distinct regions, as shown below [70].
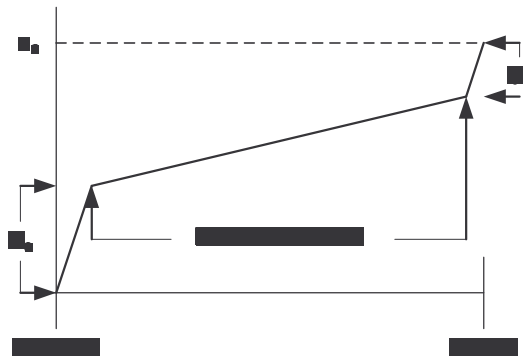
Figure 18: Arc Voltage Drop Distribution

The first region, directly adjacent to the cathode, is the cathode drop region which is followed by the positive column and then the anode drop region directly adjacent to the anode.

2.4.4.3 Cathode Phenomena

The processes occurring at the cathode of an arc discharge are critical to maintaining the current through the arc, and will be further examined in order to determine better how these processes affect the behavior of the arc. First, it is important to note that generally the cathode drop potential is on the order of the ionizing potential of the gas in which the arc burns [71]. Secondly, a cathode dark space has never been observed and so it is assumed to exist only over a very short distance, estimated to be on the order of an electron mean free path length [72]. It is also generally observed that the

cathode fall potential of the arc discharge is lower than the cathode fall in a glow discharge, suggesting that the electron emission process at the cathode must be more efficient that the emission of electrons by positive ion bombardment [73].

Particularly in high melting point cathodes, the electron emission process at the cathode is field intensified thermionic emissions. The temperature of the cathode is maintained by heat developed by positive ion bombardment, where the positive ions are likely produced in the cathode region by ionizing electron collisions. Since the cathode region is probably on the order of a mean free path length many electrons are likely to pass through this region without a collision, and since the ionization process is much less than 100% efficient, the electron current density must be much higher than the positive ion density [74]. Assuming that the cathode drop is a result of high positive ion concentrations, the positive ion current can be estimated using the space charge equation as follows [75]

$$j_p = \frac{1}{9\pi}\sqrt{\frac{2e}{M_+}}\frac{V_c^{3/2}}{d_c^2} \quad (2\text{-}39)$$

where j_p is the positive ion current density

V_c is the cathode drop potential

d_c is the cathode drop length, on the order of a m.f.p of the ion

Calculations by Mackeown take into account the electron current density in determining the field at the cathode by the following equation [76]

$$E_c = 7.57 \times 10^5 V_c^{1/2}\left[j_p(1845W)^{1/2} - j_e\right] \quad (2\text{-}40)$$

where W is the atomic weight of a positive ion of the gas

j_p is the positive ion current density

j_e is the electron current density

Experiments by Ramburg in determining the dominant electron emission mechanism at the cathode can be helpful in choosing the correct expression for current density. He found that cathodes of C, Ca, Mg, and W are thermionic and that cathodes of Cu, Hg, Ag, and Au are field type emissions. Other cathodes such as Pt, Sn, Pb, Ni, Zn, Al, Fe, and Cd probably involve some modified field type emission [77].

2.4.4.4 Positive Column

The high pressure arc is differentiated from the low pressure arc by the fact that the gas, ion, and electrons are in thermal equilibrium and at a very high temperature, allowing application of the Saha equation. Another important characteristic is the increased arc temperature at higher pressures, and the presence of electrode material in the positive column which effectively lowers the ionizing potential of the gas and raises its temperature. Similar to the glow discharge, the positive column of the arc does not

support processes integral to maintaining the arc, rather it is the result of flowing charges. Accordingly, the current density in the arc is given by [78]

$$j = \left(n_e e K_e + n_p e K_p\right) E_l \quad (2\text{-}41)$$

where K_e, K_p are the motilities of electrons and positive ions respectively

n_e, n_p are the concentrations of electrons and positive ions respectively

2.4.4.5 Anode Phenomena

The phenomena occurring at the anode of the arc discharge are similar to those in the glow discharge, where there is a drop in potential corresponding to the anode drop. The temperature at the anode is limited to the boiling point of the anode material with a few exceptions such as Zn, Al, and Mg where high melting point oxides may form in the presence of oxygen [79]. There is also a high electron space charge at the anode due to the arrival of electrons emitted from the cathode, and a high positive ion concentration at the cathode end of the anode drop region due to the formation of positive ions by electron collision [80].

Anode heating is caused by electrons at the anode, where the energy delivered per electron is the sum of the energy the electron received by being accelerated through the anode drop and the heat of electron condensation [81].

$$H_a = j\left(V_a + \phi_0\right) \quad (2\text{-}42)$$

Assuming that the only loss of heat by the anode is through radiation, and relating the heat gained by electrons arriving at the anode to heat radiated by the Stefan-Boltzmann law, the expression for the anode drop can be approximated as [82]

$$V_a = \frac{a\sigma T^4}{j} - \phi_0 \quad (2\text{-}43)$$

where V_a is the anode drop potential

a is the emissivity of the anode material (relative to a black body radiator)

ϕ_0 is the thermionic work function of the anode material

The actual anode drop potential will be higher than calculated since loss of heat through conduction of the anode, conduction near the anode, and increased radiating area will tend to raid the anode drop potential

2.5 Plasma Conductivity

Due to the presence of a large number of mobile charges on account of high degrees of ionization, plasmas are very good. Accordingly, a plasma's conductivity can be represented by a bulk material parameter that takes into account the movement of charges inside the plasma, where conductivity(σ) is a proportionality constant relating electric field strength to current density such that [83]

$$\bar{j} = \sigma\overline{E}' = \sigma\left(\overline{E} + \bar{v} \times \overline{B}\right) \quad (2\text{-}44)$$

which can also be defined as the summation of the movement of all of the charged particles in response to applied fields [84].

2.5.1 Charge Motion in Electric and Magnet Fields

Since current is the cumulative motion of charged particles it is of interest to investigate how charged particles move in electric and magnetic fields, and from this analysis an expression for the conductivity of plasma can be derived. First, consider a charged particle with initial velocity v_0 in a steady magnetic field. From earlier discussion of Lorentz forces, it is known that the force the particle feels will be normal to the $\bar{v}$ and $\overline{B}$ plane and is proportional to their product.
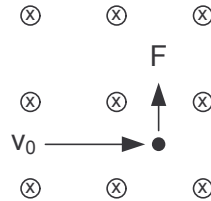
Figure 19: Charged Particle in a Magnetic Field

In this case, assuming v_0 is entirely perpendicular to the magnetic field, the charged particle will travel in a circle with radius given by [85]

$$r = \frac{Mv_{\perp}}{qB} \quad (2\text{-}45)$$

where $v_{\perp}$ is the component of initial velocity perpendicular to the magnetic field and with an angular velocity of [86]

$$\omega = \frac{qB}{M} \quad (2\text{-}46)$$

as illustrated below
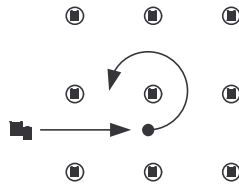
Figure 20: Motion of a Charged Particle in a Magnetic Field

Adding an electric field perpendicular to the magnetic field will modify the motion of the particle as shown below [87]
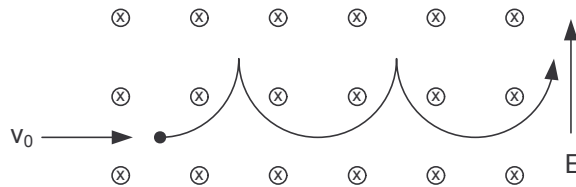
Figure 21: Motion of a Charged Particle in a Perpendicular Electric and Magnetic Field

which will maintain a velocity in the $\overline{E} \times \overline{B}$ direction regardless of the charge of the particle [88]. Any component of the initial velocity parallel to the magnetic field will not be affected, however a component of the electric field parallel to the magnetic field will cause an acceleration in that direction resulting in a parabolically displaced helix [89].

The motion of a charged particle in a perpendicular electric and magnetic field can be decomposed into two components, the first representing the circular motion caused by $\overline{v}_0 \times \overline{B}$, and a second representing a constant drift velocity in the $\overline{E} \times \overline{B}$ direction. This is significant as the radius and angular velocity of particles in a gas will have a distribution of radii and angular frequencies that may not be of particular interest, however the entire cloud of positively and negatively charged particles will drift in the same direction and with the same velocity. The drift velocity is given by [90]

$$v = \frac{E_\perp}{B} \quad (2\text{-}47)$$

In the $\overline{E} \times \overline{B}$ direction, and with a transformed radius of [91]

$$r' = \frac{ME}{qB^2} \quad (2\text{-}48)$$

2.5.2 Conductivity

Noting that charged particles of either a positive or negative charge in a perpendicular electric and magnetic field will move in the same direction and with the same velocity, it is apparent that there will be no net current, as illustrated below [92].
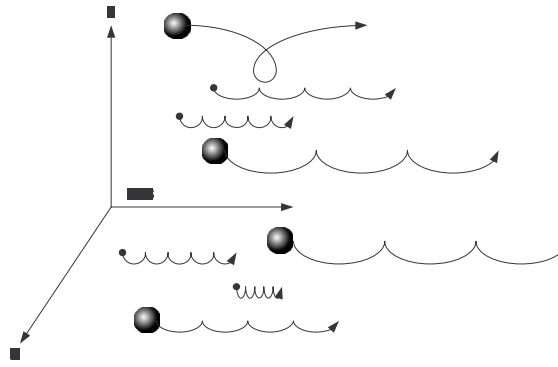
Figure 22: Particle Flow in a Perpendicular Electric and Magnetic Field

The addition of a component of the electrical field parallel to the magnetic field, however, will draw a current by accelerating the positive and negative charges in opposite directions. As Jahn notes, if collisions are ignored the charged particles in such a flow will increase in velocity linearly without limit [93]. If the electric field is applied across a positive and negative terminal, for any value of $\overline{E}_\parallel$ all charge will reach a terminal and the conductivity will not be defined. Therefore, collisions must be considered in order to obtain a relationship for the conductivity of the plasma

Jahn derives this relationship by introducing the concept of collision frequency, v_c, "in terms of the rate at which the particle swarm loses its migration momentum via all such collisions." [94] The expression relating the loss of momentum by collisions is [95]

$$\frac{d}{dt} nM\overline{v} = nq\overline{E} - v_c nM\overline{v} \quad (2\text{-}49)$$

This relationship can be rewritten as [96]

$$\dot{\overline{v}} = \frac{q}{M}\overline{E} - v_c \overline{v} \quad (2\text{-}50)$$

with v_c either being calculated directly using the cross-section of interception for momentum transfer or it can be measured as an experimental parameter. Solving this equation for the swarm velocity yields the expression [97]

$$\bar{v} = \frac{q}{Mv_c}\bar{E} + C\varepsilon^{-v_c t} \quad (2\text{-}51)$$

Recognizing that the second term is a decaying exponential transient, the steady state current density can be shown to be [98]

$$\bar{j} = nq\bar{v} = \frac{nq^2}{Mv_c}\bar{E} \quad (2\text{-}52)$$

Finally, the constant of this expression can be extracted as the conductivity of the plasma.

$$\sigma = \frac{nq^2}{Mv_c} \quad (2\text{-}53)$$

2.5.3 Hall Parameter

The Hall parameter is defined as the ratio of angular velocity of a charged particle in a crossed electric/magnetic field to the collision frequency [99]

$$\Omega = \frac{\omega_b}{v_c} \quad (2\text{-}54)$$

and indicates the direction of current flow. If the angular velocity of the particle is very high compared to the collision frequency then it will complete many cycles before experiencing a collision and loosing its streamwise momentum. In this case, the major component of current will be in the direction of gas flow [100,101,102].
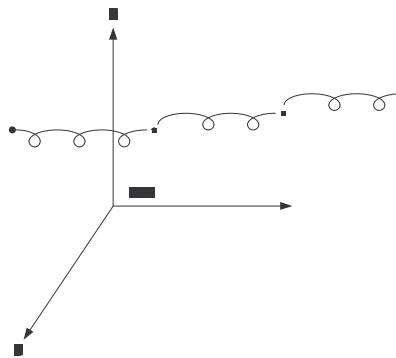
If the angular frequency and collision frequency are comparable, then the charge motion will have comparable components in the stream-wise and electric field directions.
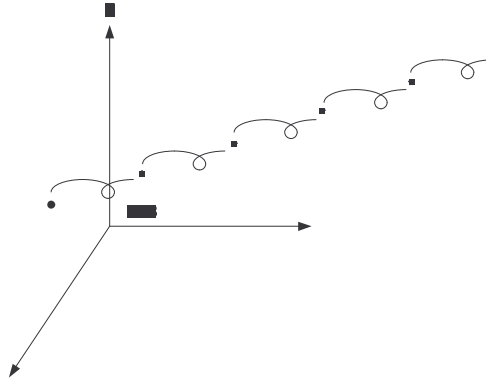
Figure 24: Hall Parameter Approximately Equal to 1

Finally, if the collision frequency is much greater than angular frequency, the charged particle will seldom complete a complete cycle and the motion will be mostly in the direction of the electric field.
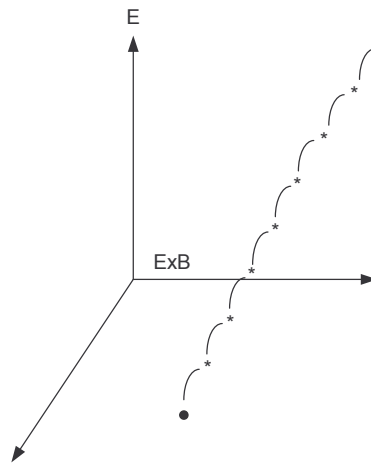
Figure 25: Hall Parameter Much Less Than 1

2.6 Compressible Flow

An important aspect of thruster design involves the delivery of some gas to the thruster nozzle, typically at high mass flow rates. Accordingly, the properties of high pressure and high mass flows rates are important both in gas delivery and nozzle design. For the purposes of this discussion, only a basic understanding of some of the limiting principles will be presented.

The most important result from compressible flow is that of the choked flow, whereby the rate of flow of the gas may be limited by the presence of a certain set of conditions. Consider a pair of containers, A and B, with different pressures where the pressure of container A is greater than B, but of sufficient volume that the rate of flow inside of the container is negligible, and that these containers are connected by some tube that has a constriction along it, as shown below in figure 26.
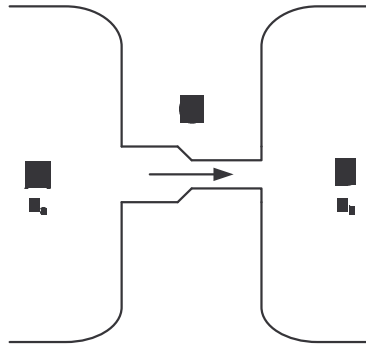
Figure 26: Compressible Flow, Un-Choked

In this example, if the absolute pressure in vessel A is less than roughly 1.8 times the absolute pressure of vessel B, then the mass flow rate will be a function of the pressure differential between the two vessels, and the flow will be at subsonic speeds throughout. If the pressure in vessel A is raised above roughly 1.8 time the pressure in vessel B, then the flow will reach the speed of sound at the smallest cross-section (called the throat), and mass flow rate will only be a function of the pressure in vessel A and the cross-sectional area of the throat. This situation may be desirable, since the mass flow rate is no longer a function of the receiving vessel's pressure, and so the mass flow rate is decoupled from down-stream conditions.

Next, consider a similar setup where two vessels of different pressures are again connected via a passage with a constriction, except this time the gas is allowed to expand after the constriction, as shown below in figure 27.
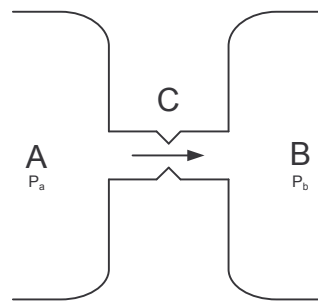
Figure 27: Compressible Flow – Choked

In this case, the flow will reach the speed of sound inside of the throat, but as the gas expands beyond the throat the flow will accelerate to super-sonic speeds. This phenomenon is employed in super-sonic nozzles, as shown below in figure 28.
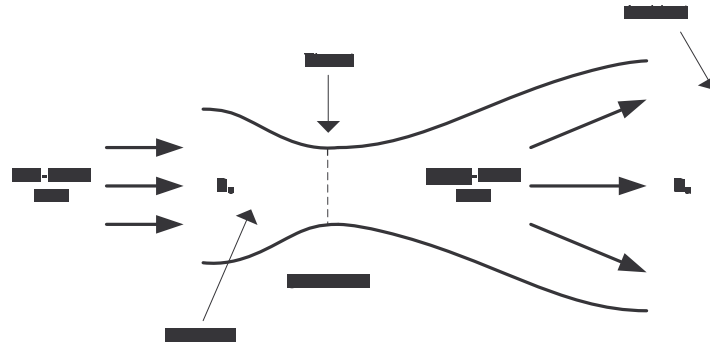
Figure 28: Super Sonic Nozzle

A typical super-sonic nozzle (also known as converging-diverging nozzle due to its geometry) is shown above. The chamber refers to the high pressure area where fuel and oxidizer is injection and combusted in conventional rockets, or any high pressure area in a converging-diverging nozzle. Ambient refers to the conditions outside of the nozzle, and the throat is again the location of the smallest cross-sectional area. Since the reaction force on the thruster is a function of the velocity of the exhaust stream, accelerating the exhaust to super-sonic speeds allows for much higher thrust levels for the same mass than sub-sonic nozzles.

2.7 Classes of Electrical Thrusters

Several different classes of electric thrusters have been devised, each exploiting a different aspect of the interaction between electric energy and kinetic energy. Electrothermal thrusters are the most like conventional chemical rockets, whereby a gas is heated in order to convert the thermal energy into directed kinetic energy. Electrostatic thrusters use the force exerted between two charged particles to generate thrust, while electromagnetic thrusters use the force that arises between the interaction of magnetic fields and electric currents. The electrothermal and electromagnetic thrusters will be characterized and analyzed below, with an emphasis placed on electromagnetic thrusters.

2.7.1 Electrothermal Thrusters

Electrothermal thrusters work by converting electrical energy into thermal energy in a gas, and then convert the thermal energy of the gas into directed kinetic energy. Heating of the gas can occur by passing it over a resistive heater element, heating it directly with an electric arc, or inducing currents through some non-contact method.
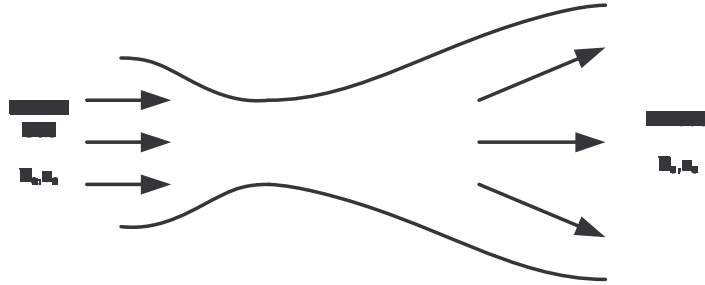
Figure 29: Electrothermal Thruster Schematic

In all cases, the maximum attainable exhaust velocity is governed by the amount of thermal energy transferred to the gas by the equation [103]

$$\frac{1}{2}v_e^{\ 2} = \frac{1}{2}v_c^{\ 2} + c_p(T_c - T_e) \approx c_p T_e \quad (2\text{-}55)$$

where v_e is the exhaust velocity of the gas

v_c is the chamber velocity of the gas

c_p is the specific heat of the gas at constant pressure

T_e is the exhaust temperature of the gas

T_c is the chamber temperature of the gas

By simply rearranging this equation, the relationship between exhaust velocity and exhaust temperature can be found to be [104]

$$v_e = \sqrt{2c_p T_e} \quad (2\text{-}56)$$

Of course, this simple relationship ignores all modes of energy loss such as radiation from the nozzle, viscous losses, etc.

Electrothermal thrusters are generally limited by the maximum working temperature of the wall material, which cannot be heated to such a high temperature as it begins to lose its structural properties. Furthermore, practical limitations are set by the size of the power supply, which limits the mass flow rate through the thruster and thereby limits the maximum thrust.

To illustrate the practical limits of an electrothermal thruster, an example is presented here from Jahn's *Physics of Electric Propulsion*. An arbitrary maximum gas temperature is set to 3000K (which roughly corresponds to the maximum working temperature of highly refractory materials, such as tungsten and carbon.) Hydrogen is chosen as the working gas of the thruster due to its high specific heat of $2 \times 10^4 \ J/kg \cdot K$ at a temperature of 3000K. The final constraint is the power supply, which is taken to be limited to 30kW of power. By estimating the exhaust velocity to be about $10^4 \ m/s$, the flow rate and thrust can be computed. The total energy per kilogram of fuel needed to

34

obtain exhaust velocities of $10^4\ m/s$ is $5 \times 10^7\ J$. Therefore, the maximum flow rate is limited by the power supply to $6 \times 10^{-4}\ kg/s$ with a corresponding thrust of 6 N [105].

Nearly all other design aspects of an electrothermal thruster relate to reducing losses associated with the large thermal gradients generated and non-idealities of the fuel gas. These issues will not be covered here as they pertain to electrothermal thrusters, but many of the loss mechanisms discussed in later sections also apply here.

2.7.2 Electromagnetic Thrusters

Electromagnetic thrusters operate based on applying a force density to an ionized gas via the interaction of the current through the gas and either an applied magnetic field or the magnetic field produced by the current flowing through the gas. Neglecting the details of how the magnetic field is generated, such a thruster operates based on the Lorentz force applied to a gaseous conductor as illustrated below [106].
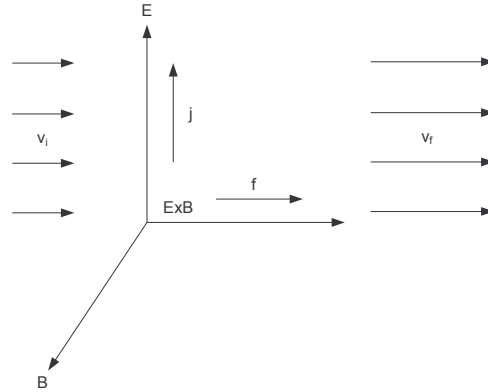
Figure 30: Simplified Electromagnetic Thruster Schematic

In this illustration, a gaseous conductor is passed through a perpendicular $\overline{E}$ and $\overline{B}$ field with initial and final velocities parallel to $\overline{E} \times \overline{B}$. As discussed in earlier sections concerning plasma conductivity, the current that will flow will be $\overline{j} = \sigma\left(\overline{E} + \overline{v} \times \overline{B}\right)$ which is parallel to $\overline{E}$. This will cause a force density equal to $\overline{f}_b = \overline{j} \times \overline{B}$ in the gas and accelerate it through the channel [107].

On an atomic level, electrons which are emitted into the stream will attain some drift velocity in the $\overline{E} \times \overline{B}$ direction and collide with gas molecules thereby transferring their momentum to the gas stream [108]. Though there are many different configurations of electrodes, gasses, power supplies, and so forth that can produce this sort of body force, the magnetogasdynamic thruster will be considered first as a generalized model and later the magnetoplasmadynamic (plasma or arc) thruster will be considered.

2.7.2.1 Magnetogasdynamic Model

The magnetogasdynamic model treats the ionized gas in a thruster as a fluid which can be reasonably well described by a set of material parameters such as viscosity, thermal conductivity, density, conductivity, etc, and a set of equations that describe the behavior of the fluid [109]. The three equations that need to be considered are conservation of mass, motion, and energy balance [110].

$$\frac{\partial \rho}{\partial t} + \nabla \cdot (\rho \bar{v}) = 0 \quad (2\text{-}57)$$

$$\rho\left(\frac{\partial v}{\partial t} + \bar{v} \cdot \nabla \bar{v}\right) = -\nabla p + \left(\bar{j} \times \bar{B}\right)_v \quad (2\text{-}58)$$

$$\rho\left(\frac{\partial}{\partial t} + v \cdot \nabla\right)\left(c_p T + \frac{v^2}{2}\right) = \frac{\partial p}{\partial t} + \bar{j} \cdot \bar{E}_r \quad (2\text{-}59)$$

where p is the pressure of the gas

ρ is the density of the gas

c_p is the specific heat of the gas

v is the velocity of the gas

Note that the viscous body force density, net thermal input by conduction, net viscous dissipation, and radiant energy loss have been omitted from these equation. These equations also assume that the magnetic field is independent of the electric field and current, and that the flow is isothermal. By combining these equations with equations of state and Maxwell's equations, a simpler set of equations can be derived [111].

$$\rho v = F = cons \tan t \quad (2\text{-}60)$$

$$\rho v \frac{dv}{dx} = -\frac{dp}{dx} + j\bar{B} \quad (2\text{-}61)$$

$$\rho v \frac{d}{dx}\left(c_p T + \frac{v^2}{2}\right) = j\bar{E} \quad (2\text{-}62)$$

$$j = \sigma\left(\bar{E} - v\bar{B}\right) \quad (2\text{-}63)$$

$$p = \rho R T \quad (2\text{-}64)$$

$$\sigma = \sigma(p, T) \quad (2\text{-}65)$$

where F is the mass flux. Assuming an isothermal flow (temperature is constant along the channel) the equation of energy and motion can be combined to yield [112]

$$Fv\frac{dv}{dx} = \xi\left(F\frac{dv}{dx} + \frac{dp}{dx}\right) \quad (2\text{-}66)$$

where $\xi = \dfrac{E}{B}$. This relationship can be simplified to [113]

$$\xi = \frac{v^3}{v^2 - RT} \quad (2\text{-}67)$$

Noting that $(RT)^{1/2}$ is the isothermal speed of sound in the gas, it is apparent that ξ has a zero in the denominator where the flow velocity equals the isothermal speed of sound in the flow [114]. This condition corresponds to the flow becoming choked and developing a shockwave, beyond which the flow cannot accelerate. In order to avoid this condition, supersonic inlet velocity is required.

2.7.2.2 External Field Accelerators

Assuming that the magnetic field generated by the current flowing through the gas is negligible compared to an applied external field, only two more equations are needed in order to solve for all of the variables, and with the constraint of constant power input over the channel length, the relatively simple solution is calculated to be [115]

$$v^* = \left(1 + 2\frac{PL}{Fv_0^2}x^*\right)^{1/2} \quad (2\text{-}68)$$

where v^* is the dimensionless gas velocity defined as v/v_0
v_0 is the initial gas velocity
P is the power input per unit length
L is the channel length
x^* is the dimensionless position defined as x/L

In the velocity profile equation the term PL/Fv_0^2 is referred to as the magnetic interaction parameter (β), and specifies the strength of the electromagnetic interaction. Graphing the dimensionless velocity against the magnetic interaction parameter times the dimensionless position for constant power input per unit length yields the velocity profile along the accelerator channel [116].
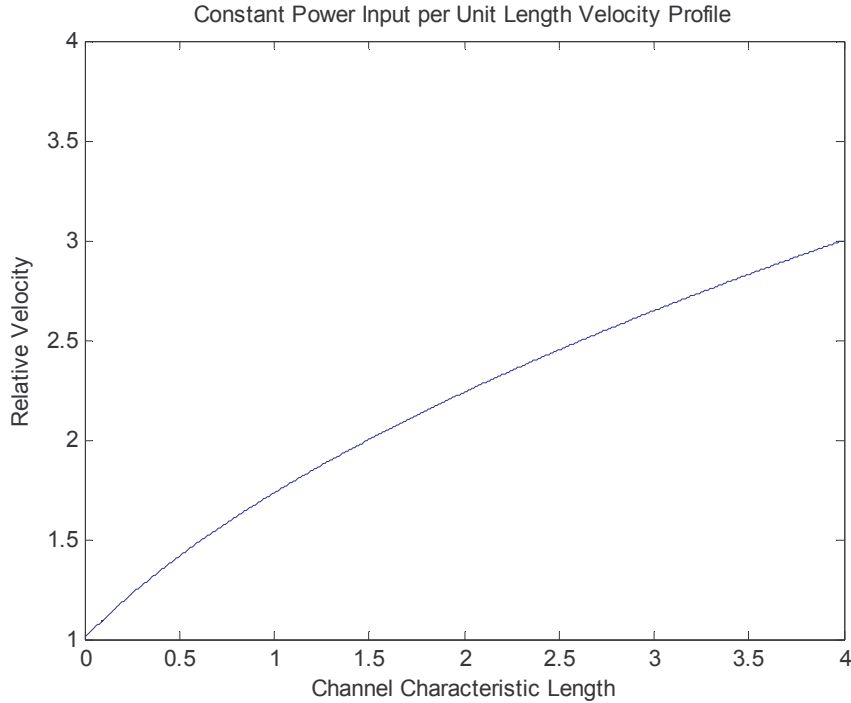
Figure 31: Velocity Profile for Constant Power Input per Unit Length

Jahn notes that the relative velocity (v^*) is a weak function of βx^*, and that the overall acceleration of the gas along the channel length is not particularly impressive [117]. He also suggests that removing the constant area constraint on the channel could improve performance, though this is likely to result in only a modest increase in performance [118]. It is also possible to achieve higher levels of performance by setting $E(x)$ and $B(x)$ to different values along the channel, but such analysis is beyond the scope of this document and building a device to implement variable E and B fields is prohibitively complicated for a practical thruster [119].

2.7.2.3 Self-Field Accelerators

This class of accelerators assumes that any externally applied magnetic field is negligible compared to the magnetic field generated by the current through the ionized gas. Self-field effects become significant when the current density reaches approximately 10^5 or 10^6 A/m^2. Accordingly, the high current densities found in self-field accelerators imply correspondingly high gas conductivity without the need for pre-ionizing equipment, and also relieves the need for an external magnet [120]. For self-field accelerators the dimensionless parameter known as the magnetic Reynolds number specifies the relative importance of the self-field [121].

$$R_B = \mu \sigma v L \quad (2\text{-}69)$$

When R_B is much greater than one, the self-induced magnetic field must be considered. If it is much less than one, then its effect can be ignored. This class of accelerator can be more easily studied if the discharge region is sufficiently narrow that the details of the internal conditions can be simplified in to discrete conditions before and after the discharge region [122]. For this condition, the conservation equations are [123]

$$F(v_l - v_0) + (p_l - p_0) = \frac{\mu J^2}{2} \quad (2\text{-}70)$$

$$\frac{\gamma}{\gamma - 1}(p_l v_l - p_0 v_0) + \frac{F}{2}\left(v_l^2 - v_0^2\right) = JE \quad (2\text{-}71)$$

If an isobaric jump condition is imposed on the discharge sheet then the change in gas velocity can be expressed as [124]

$$v_l - v_0 = \frac{\mu J^2}{2F} \quad (2\text{-}72)$$

and the electric field intensity can then be expressed as [125]

$$E = \left(\frac{\gamma}{\gamma - 1}\frac{p_0}{2F} + \frac{v_0}{2}\right)\mu J + \frac{\mu^2 J^3}{8F} \quad (2\text{-}73)$$

For most accelerators where μJ^2 dominates, the exit velocity can be simplified to

$$v_l = \frac{4E}{B_0} \quad (2\text{-}74)$$

where B_0 is the magnetic field at the inlet. This compares favorably to external field accelerators which are limited to maximum exhaust velocities equal to the drift velocity of particles in the magnetic and electric field given by E/B.

2.7.2.4 Magnetoplasmadynamic Thrusters

External and self-field type accelerators were considered impractical for space thrusters, due to the large amount of auxiliary equipment such as pre-ionizers and external magnets, until in 1964 the phenomena of the magnetoplasmadynamic arc was discovered by accident while investigating low mass flux arcjet thrusters. By reducing the mass flux in an arcjet thruster exhaust velocities observed at 20,000-30,000 m/s without the need for bulky external machinery or complex nozzle assemblies to implement programmed electric and magnetic fields [126].

While the benefits of such a thruster were immediately apparent, the details of how they operated were not. This was complicated by the fact that significant levels of

thrust were observed in this class of thruster even when operated without any propellant gas. Three separate descriptions of the magnetoplasmadynamic thruster have been suggested, each providing some insight into the possible processes occurring inside the MPD arc. In all likelihood, the actual process is probably some combination of the three different descriptions.

Similar to the external and self-field accelerators already discussed, the MPD thruster can be described in terms of magnetogasdynamic interactions. Owing to it's origin as a short-channel arcjet thruster, the MPD thruster electrode are often configured in a similar fashion to other arcject thrusters. Typical electrode geometry is shown below [127].
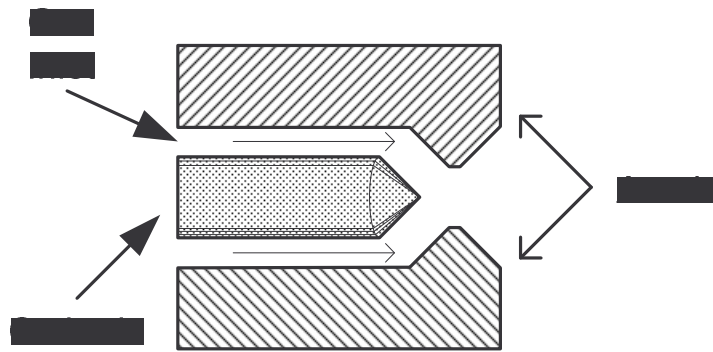
Figure 32: Typical MPD Thruster Electrode Geometry Cross-Section

In the magnetogasdynamic description, two components contributing to the total thrust can be considered. The first component is the result of the radial current from the cathode crossed with the azimuthal self-magnetic field which generates a streamwise force on the ionized gas. The second component is a result of an axial current from the cathode tip crossed with the azimuthal self-magnetic field which generates an axial force on the ionized gas. Jahn refers to these individual components as the "blowing" and "pumping" contributions, as shown in figure 33 [128].
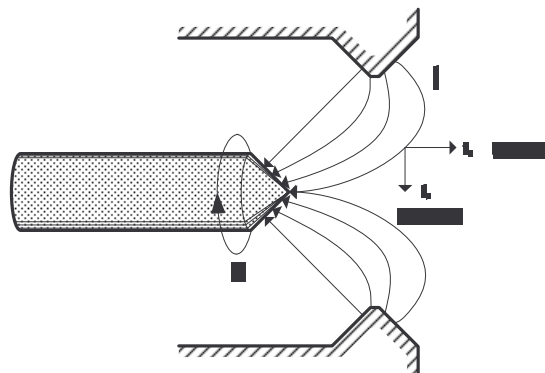
Figure 33: Pumping and Blowing Force Contributions

These body forces on the ionized gas can be decomposed into three separate easily analyzed modes. The first mode is defined for radial current density uniform over the surface of a rod of constant radius. [129]
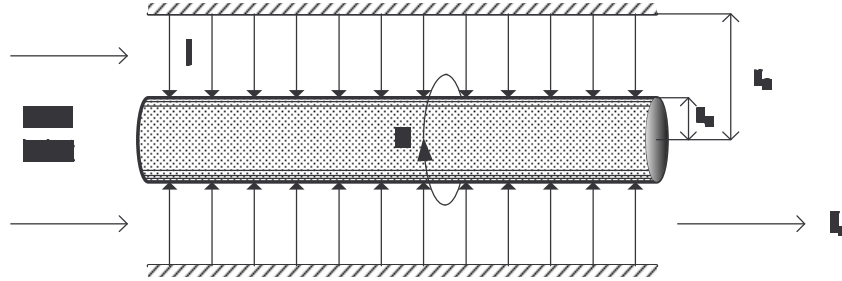
Figure 34: Blowing Force from Radial Current

Therefore, the self-magnetic field can be described as [130]

$$B_\theta(r,z) = \frac{\mu J}{2\pi r}\left(1 - \frac{z}{z_0}\right) \quad (2\text{-}75)$$

where J is the total current. With the B field defined, the force density is simply the product of the current density (a function of radial position only) and the B field [131].

$$f_z(r,z) = j_r B_\theta = \frac{\mu J^2}{4\pi^2 r^2 z_0^2}(z_0 - z) \quad (2\text{-}76)$$

The total streamwise force contribution from the radial current over the constant radius cathode is then the integral over the discharge gap volume [132].

$$F_z = \frac{\mu J^2}{4\pi}\ln\left(\frac{r_a}{r_c}\right) \quad (2\text{-}77)$$

where r_a is the radius to the anode wall

r_c is the radius of the cathode

The second force contribution arises from current entering the conical tip of the cathode, which can be accounted for by extending the limits of integration, and which results in a second term in the total force equation. This current is shown in figure 35 [133]

41
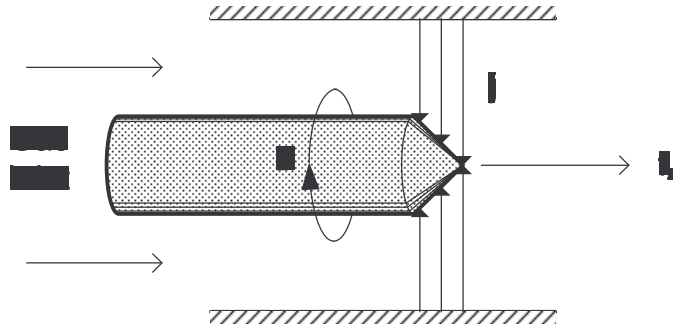
Figure 35: Blowing Force from Radial Current at Conical Tip

And the resulting total pumping force contribution is [134]

$$F_z = \frac{\mu J^2}{4\pi} \ln\left(\frac{r_a}{r_c} + \frac{1}{2}\right) \quad (2\text{-}78)$$

Equation 1: Total Blowing Force Contribution

The final force contribution arises from the pumping action as a result of current entering the conical tip normal to the surface as shown in figure 36. [135]
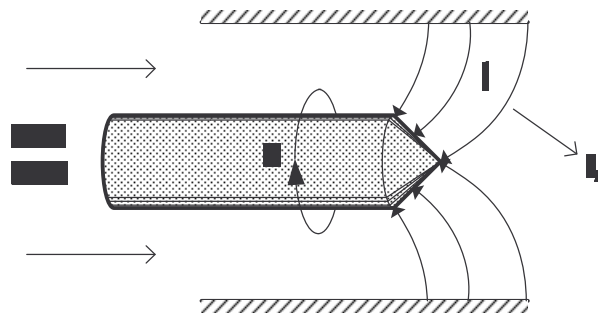
Figure 36: Pumping Force from Radial Current

The magnetic field is defined as before, except it is now dependant on the radius of the tip along its length [136].

$$B_\theta(r,z) = \frac{\mu J r}{2\pi r_c^2} \quad (2\text{-}79)$$

Again the force density is the product of the B field and the current density, however, it must be balanced by a pressure gradient in equilibrium [137].

$$f_z(r,z) = j_r B_\theta = \frac{\mu J^2 r}{2\pi^2 r_c^4} = -\frac{dp}{dr} \quad (2\text{-}80)$$

This pressure on the conical tip is therefore [138]

$$p(r) = p_0 + \frac{\mu J^2}{4\pi^2 r_c^2}\left[1 - \left(\frac{r}{r_c}\right)^2\right] \quad (2\text{-}81)$$

Integrating the pressure over the cathode tip results in an axial force [139]

$$F_c = \frac{\mu J^2}{8\pi} \quad (2\text{-}82)$$

Combining these three force components yields the total force as [140]

$$F = \frac{\mu J^2}{4\pi}\left(\ln\frac{r_a}{r_c} + \frac{3}{4}\right) \quad (2\text{-}83)$$

The term $\mu/4\pi$ is equal to 10^{-7} in M.K.S., with force being a function of the total current squared, and so at even modest ratios of anode and cathode radius thrust levels of interest can be expected above 1kA [141].

The MPD arc can also be described according to the motion of the ions, leading to the particle description which assumes that particle collisions are only important near the anode wall where they are generated, and that the rest of the flow is collisionless [142]. Though this is not likely a safe assumption for most practical thrusters, it does lead to several useful relationships that can help to explain phenomena which the magnetogasdynamic model does not address.

In particular, the concept that the entire current is carried by positive ions created near the anode leads to a relationship between current and mass flow. Under these assumptions, where positive ions are the current carriers and that the gas is nearly completely ionized, gas must be supplied to the arc at such a rate that positive ions can be created at no less than the rate that current flows [143]

$$J \leq \frac{\dot{m}e}{M_+} \quad (2\text{-}84)$$

This relationship yields useful insight into the operation of MPD thrusters when no gas is fed to the arc. It is likely that under these conditions vaporized electrode material becomes the current carrier, and so to limit electrode erosion the gas mass flow should be maintained above a minimum level corresponding to the arc current.

Another requirement of the particle description is that the positive ions have gyro radii sufficiently small to prevent them from colliding with the electrode walls, and therefore the radii must decrease with their radial position in the arc such that [144]

$$r_B^+(r) = \frac{M^+ v^+}{eB} = \frac{2\pi r M^+ v^+}{\mu e J} \quad (2\text{-}85)$$

Substitution of the positive ion velocity can be replaced by the stream velocity derived early, which yields the two following relationships [145]

$$v \leq \frac{\mu e J}{2\pi M^+} \leq \left(\frac{2Ve}{M^+}\right)^{1/2} \quad (2\text{-}86)$$

Jahn note that these inequalities predict, insofar as the assumptions of the particle description are valid, "…an arc voltage that varies as J^2, a thrust that varies as J^2, and an exhaust speed proportional to J and inversely proportional to M^+."

3 Design

This section discusses the design considerations and limitations of the magnetoplasmadynamic thruster, power supply, and instrumentation used in analyzing its performance. A practical model for MPD thruster operation will be constructed which will later be used for conducting simulations to compare against measured thruster performance.

3.1 Design Constraints

The magnetoplasmadynamic (MPD, or Plasma) thruster converts electrical energy into thrust by way of the Lorentz Force as a result of the interaction between electrical current through conductive gas (plasma) and the magnetic field resulting from the discharge current. Since the objective of this project is to analyze the thrust output of such a device, the most important design requirement must be that the device creates enough thrust to be easily measured with relatively inexpensive equipment. Accordingly, this design will attempt to achieve on the order of several Gs of acceleration.

Ideally, the initial design for such a thruster would maintain as many degrees of freedom in setting system parameters as possible. Unfortunately, access to materials and funding considerably constrained several aspects of the design even before setting pencil to paper. In particular, this class of thruster requires on the order of thousands of amperes of current and tens of kilowatts of power in order to generate significant thrust, which immediately eliminates the possibility of using a steady power supply, and limits the design to whatever pulsed supply can reasonably be obtained or assembled. Similarly, the type and rate at which gas is delivered to the nozzle during operation is limited to what can be obtained with relative ease at a minimum of expense. This is likely to constrain the working gas to those available in bulk for general commercial or industrial use.

Therefore, though it may be tempting to begin directly with a numerical analysis and design the thruster package around those constraints which limit thruster performance, it is instead preferable to analyze those materials and equipment which are available for this design and then proceed with a numerical analysis.

3.1.1 Power Supply

Since the force generated by an MPD thruster is a quadratic function of the total current supplied to the nozzle, the proper design of the power supply must be a primary concern. It is also clear that the number of practical choices for power supply topology is seriously constrained by the operating requirements of the thruster. In this case, the design is limited to pulsed power supplies, and of those available the capacitor bank is probably the most economical and practical.

From the gas, ionization, and thermal background already covered it is clear that the design and analysis is considerably simplified if it can be assumed that the ionized gasses are reasonably well represented by models that assume thermal equilibrium. In order to justify these assumptions, the power supply must be able to supply current to the

nozzle for long enough to establish thermal equilibrium in the gas and maintain a quasi-steady state of operation for long enough so that the steady state operation dominates the resulting performance. Cobine suggests that thermal equilibrium conditions can be reached in on the order of $10^{-4}s$, and therefore it is probably reasonable to try to sustain operation of the thruster for on the order of $10^{-3}s$.

Thus far it has been established that in order to operate the thruster under conditions which it can be profitably studied the current needs to be maintain on the order of thousands of amperes for a length of time on the order of milliseconds. Accordingly, a fair set of conditions to set on the power supply design suggest that the total energy stored be maximized, the total inductance of the system be minimized, and that the equivalent series resistance be minimized. Capacitor ESR and ESL can be minimized by using capacitors designed to reduce these parasitics, by connecting many units in parallel, or both. Parasitic resistances and inductances in the interconnects between capacitors as well as AC losses can be minimized by using thin, wide buss bars.

With these considerations in mind computer/inverter grade electrolytic capacitors with a working voltage of 350V (400V surge) rated at 3.6uF -10%/+50% were chosen. 128 of these capacitors were obtained and assembled into 8 plates arranged in a 4x4 pattern of capacitors connected with 1"x1/8" aluminum flat stock along the columns and 1.5"x1/8" aluminum flat stock across rows. Plates were stacked and connected to each other with two bars of 1.5"x1/8" aluminum flat stock in two stacks of 4 plates. Each capacitor was connected with a 20 kΩ bleeder resistor, and each column was also connected to a 400V metal-oxide varistor. The total energy storage at the rated working voltage was 28.4 kJ.

The V/I characteristic curve of the arc discharge is a non-linear function, and therefore sensitive to the external circuit to which is it connected. Accordingly, in order to obtain reasonable predictions of performance the power supply must be well characterized with parasitics and other relevant phenomena. Figure 37 is the circuit diagram for the power supply which enumerates the various ideal and parasitic components.
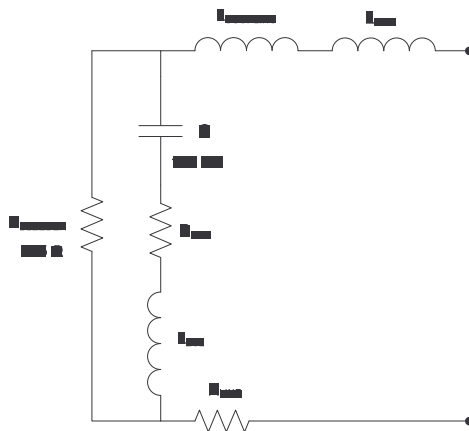

Figure 37: Power Supply with Parasitics

The circuit diagram represents the capacitor bank used to power the thruster, and the power supply connection leads, along with the coupling transformer and bleeder resistors. In this diagram C, R_{ESR}, and L_{ESL} represent the capacitor bank and its equivalent series resistance and inductance. In parallel with the capacitor bank is the bleeder resistor, marked $R_{BLEEDER}$. $L_{COUPLING}$ and L_{LINE} represent the self-inductance of the high voltage air-core coupling transformer and the inductance of the power supply leads, respectively. Finally, R_{LINE} represents the resistance of the power supply leads as well as the buss bars in the power supply. The estimation and measurement of these values are presented as follows.

3.1.1.1 Estimated Inductance and Resistance

Due to the large number of capacitors connected in parallel, it is likely that the parasitics in power supply leads will dominate those found in the capacitors and their associated buss bars. Therefore a good rough estimate may be made by simply considering a loop of cable the length of the power supply leads in calculating the resistance and inductance of the power supply. For the purpose of these calculations, the power supply leads will be considered as two parallel loops of 2 AWG copper cables with a diameter of 0.7m.

The inductance of the leads can be estimated by using the equation [146]

$$L = \mu_0 a \left[\ln \frac{8a}{r} - 1.75 \right] \quad (3\text{-}1)$$

Equation 2: Estimation of the Inductance of a Loop of Wire

where a is the radius of the loop of wire
r is the radius of the conductor
Therefore the self-inductance of one loop of 2 AWG wire with a = 0.7m and r = 0.0033m is 6.6uH, and two parallel loops is 3.3uH. Similarly, the resistance can be estimated from the resistance of 2 AWG wire being 0.513 Ω per kilometer [147] which results in an approximate DC resistance of 1.1 mΩ.

3.1.1.2 Measured Inductance and Resistance

Considering the probable magnitude of many of the parasitic elements, a sufficient model of the power supply is an LRC circuit where parasitic elements are lumped together. The power supply was modeled as an LCR circuit with the capacitor's bleeder resistor explicitly included. All other parasitics were lumped into the L and R components. The transfer function of the power supply circuit was obtained by connecting a signal generator across the nozzle terminals of the power supply and sweeping the frequency. The diagram below shows the circuit used to generate the transfer function. R_{OUT} is the external resistor which was added to prevent the large capacitance from loading down the signal generator. R_S is the series resistance of the power supply leads and capacitor equivalent series resistance. L is the inductance of the power supply leads and internal capacitor inductance, and R_B is the bleeder resistor

connected to the capacitor bank to slowly dissipate any extra charge on the capacitors when the device is not in use.
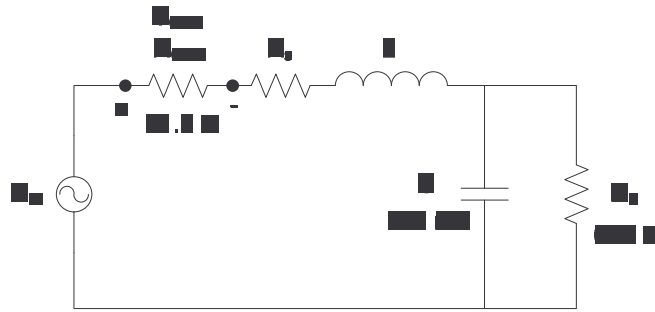
Figure 38: Power Supply Inductance Test Circuit

Considering the relative magnitude of the R_{OUT} resistor and the resistance of the high current cabling, R_S is relatively small and can be safely ignored compared to R_{OUT}. The capacitance is a known value, 115 mF, and the resistance and inductance can be determined with relative ease experimentally. After careful measurement the transfer function was determined to be
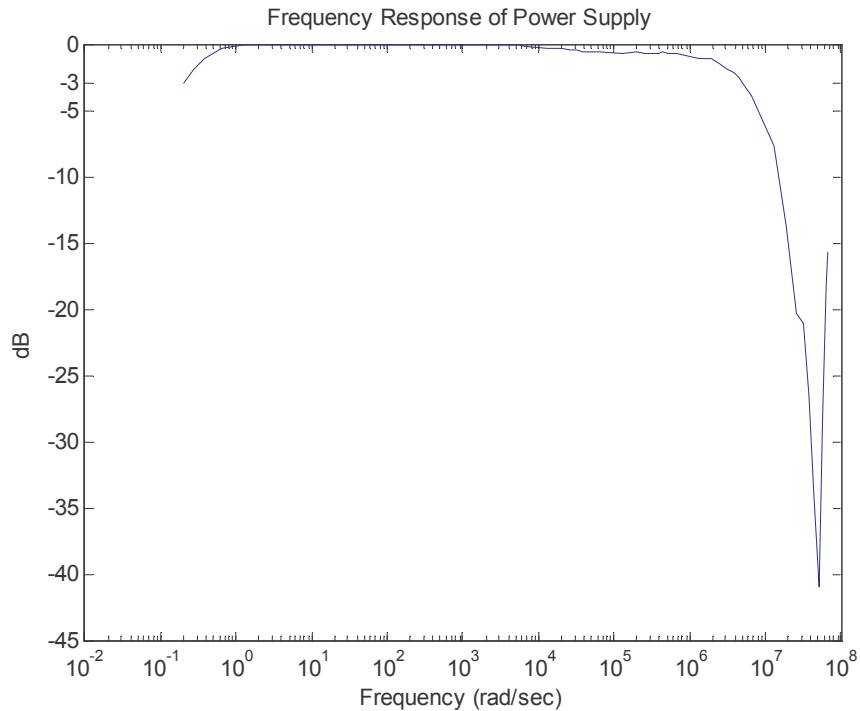
Figure 39: Transfer Function for Determining Power Supply Inductance

The transfer function has a zero at the origin and two poles, one from the capacitor bank and one from the inductance in the power supply. The low frequency pole occurs at -0.2 rad/sec, corresponding to a capacitance of 97 mF, which is reasonably close to the actual

value of 115 mF. The high frequency pole occurs at -4.7 Mrad/sec, corresponding to an inductance of 11 uH. This is somewhat higher than calculated earlier, which is expected since the earlier calculation neglected the self-inductance of the coupling transformer and the frequency dependence of the power supply inductance.

The final parameter that needs to be found is the resistance of the wiring in parallel with the capacitor's ESR. This value is likely on the order of a couple of mΩs. Accordingly, the time constants for the LR and RC circuits will probably be on the same order of magnitude, complicating the task of measuring the power supply series resistance. Instead, the voltage across the power supply and across the arc was observed, and the voltage difference across the cabling was used to estimate the resistance. The result, within experimental error, agreed with the calculated.

3.1.1.3 Lumped Model

Assembling the measured values (which agree reasonable well with the calculated estimations) into a simple model for the capacitor bank yields the following circuit
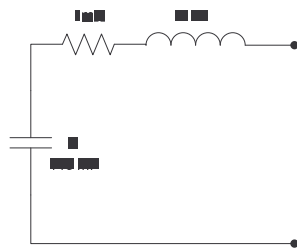
Figure 40: Power Supply Model

where C is the capacitance of the capacitor bank, R_{ESR} is the sum of all parasitic resistances in the circuit, and L_{ESL} is sum of all of the parasitic inductances in the circuit.

3.1.2 Gas Injection

The working gas for this system was limited to the widely available industrial gasses, such as N2, CO2, Ar, and He. Of these, the most readily available monatomic gas is Argon due to its use in welding applications as a shielding gas. Its monatomic nature prevents energy loss during ionization due to dissociation energies associated with diatomic gasses, is reasonably light for a noble gas, and has low thermal conductivity which corresponds to lower thermal losses and electrode erosion in the thruster nozzle. It can be easily obtained in high pressure gas cylinders and delivered at lower pressure via a regulator, though even high flow regulators are inadequate for this purpose. This shortcoming can be easily overcome with a large volume surge tank, which is pressurized to the working pressure of the system and acts as a reservoir which can supply very high mass flow rates.
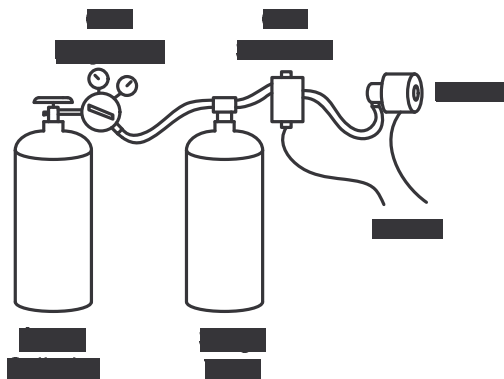
Figure 41: Gas Injection System

The maximum gas delivery pressure from the regulator (Harris 3500-125 High Flow Argon Regulator) and the maximum inlet pressure to the gas solenoid (AAA Products SS-40 Gas Solenoid) is 160 PSIG (174.7 PSIA.) Referring to the gas solenoid datasheet, the maximum mass flow rate to ambient at 160 PSIG can be calculated by

Body Style: #4, ½" Port:

$$\frac{174.7}{94.7}(215.0) = 327 \quad (3\text{-}2)$$

resulting in 327 SCFM at S.T.P. or 0.6 grams/s for Argon which is equivalent to 0.0149 mol/s. Since the delivery pressure is more than 1.7 times greater than ambient, and all orifices downstream of the solenoid are at least as large as the solenoid outlet, choked flow conditions will exist in the gas solenoid and the flow rate is independent of the back-pressure from the nozzle. See the appendix for the relevant gas solenoid specifications.

3.2 Subsystems

There is significant flexibility in the design of the remaining subsystems which includes the measurement instrumentation, ignition system, and thruster nozzle. The design of these subsystems will be presented below.

3.2.1 Instrumentation

The instrumentation of the thruster includes all equipment meant to measure the performance of the thruster in order to validate the theoretical predictions. Important variables that relate to the operation of the thruster include the arc current, power supply voltage, and thrust. All sensors were designed to interface to a National Instruments USB-6211 DAQ.

3.2.1.1 Arc Current

The arc current was measured via a low-noise shunt resistor constructed with concentric copper cylinders.
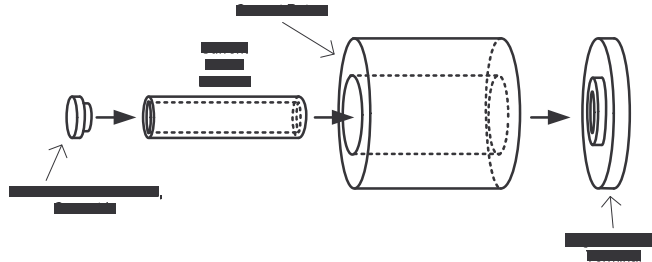
Figure 42: Current Sense Resistor, Exploded View

Since the current enters the current sense resistor in one direction and return in the opposite, the net flux in the volume between the two cylinders is zero. Also, by keeping the volume between cylinders small there will be little coupling to other fields and thus the current transducer is less susceptible to self induced and external noise.

The low voltage measured across the current sense element was amplified and isolated as well, which was accomplished using a variable gain amplifier and an isolation amplifier. The total bandwidth of the entire circuit was roughly 120 kHz, set by the isolation amplifier. The circuit used is shown below in figure 43.
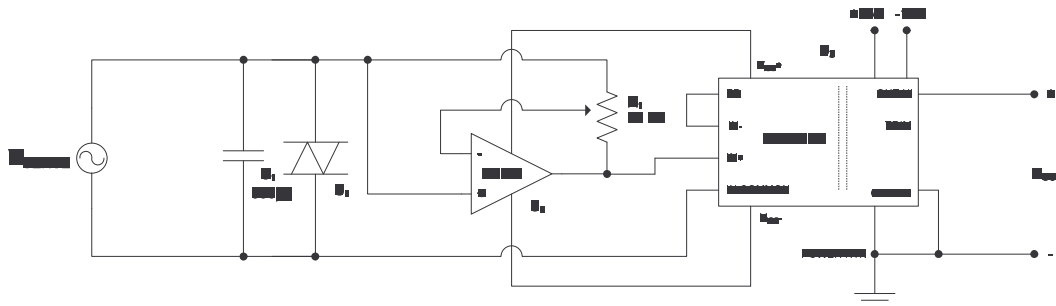
Figure 43: Arc Current Sense Interface

V_{SENSE} is taken directly from the terminals of the current sense resistor, with the combination of C_1 and U_1 (a 9V 45A metal-oxide varistor) forming an over-voltage protection network. U_1 clamps the voltage at a maximum of 9V, and the capacitor limits the rise rate of the voltage while U_1 turns on. R_1 and U_2 form a variable gain amplifier which is used to calibrate the current sensor, and U_3 is an isolation amplifier set to a gain of unity, which protects the measurement equipment from the high common mode voltage at the input.

3.2.1.2 Power Supply Voltage

The power supply voltage was measured directly from the positive and negative rails of the capacitor bank through a calibrated resistive divider and an isolation amplifier. The resistive voltage divider was calibrated to achieve a gain of 5V/700V. The interface circuit is shown below in figure 45.
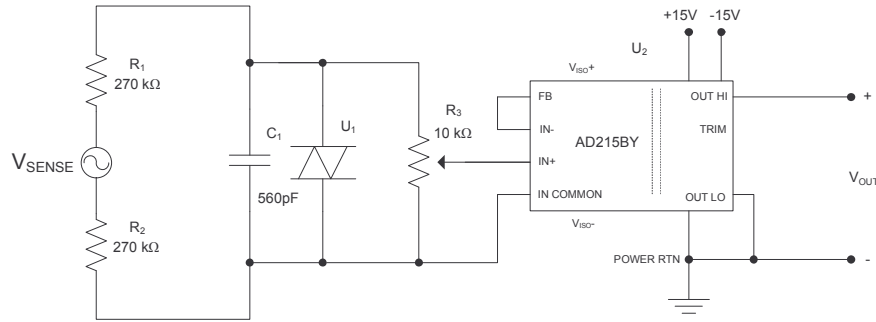
Figure 44: Power Supply Voltage Sense Interface

V_{SENSE} is connected across the capacitor bank terminals, with R_1 and R_2 preventing dangerous arcing in case of a short circuit. R_1 and R_2 also form a voltage divider with R_3, which is used to calibrate the sensor. C_1 and U_1 (a 9V 45A metal-oxide varistor) form an over voltage protection circuit. U_2 is an isolation amplifier that protects the measurement from high common mode voltages present on the capacitor bank.

3.2.1.3 Thrust

The force of the thruster was measured by way of an accelerometer (Freescale Semiconductors MMA1220D +/-8G accelerometer) attached to the nozzle by rubber shock-mounts, where acceleration and force are related by a factor of the nozzle's mass. In order to eliminate the effects of friction as completely as possible, the nozzle was mounted to a low friction track system consisting of 4 Thompson SPB-12 linear bearing pillow blocks traveling on a pair of Thompson LinearRace case 60 hardened ¾" steel rods measuring 22" long.

Figure 45: Thrust Measurement Test Stand

3.2.2 Ignition System

The ignition circuit is a particularly important component to this design. Since the capacitor bank is charged to voltages below the breakdown voltage of the nozzle gap, an external circuit is needed to impose a high voltage across the nozzle electrodes in order to initiate a dielectric breakdown without adversely affecting the high current discharge or

exceeding the operational limits of the power supply. The simultaneous high voltage and high current requirements make finding a suitable topology particular challenging. The power supply and nozzle are shown schematically below with operational constraints as labeled.
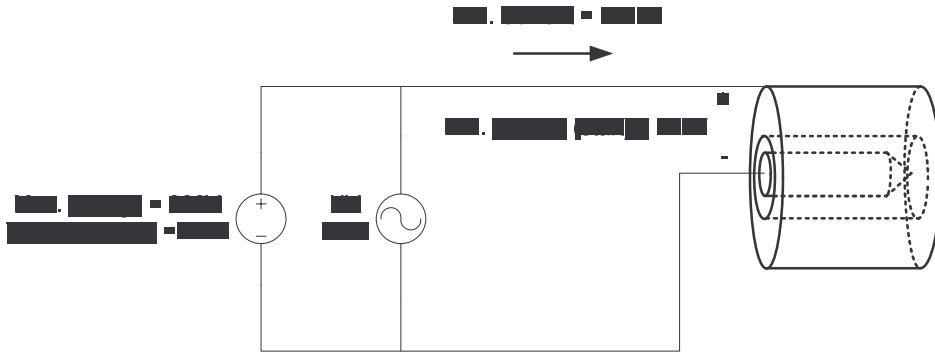
Figure 46: Power Supply and Nozzle Constraints

On inspection, the first practical problem in meeting these requirements are the conflicting requirement of maximum voltage across the power supply and minimum starting voltage. It is clear that the power supply must be decoupled from the high starting voltage, and perhaps the most logical place to start would be with a diode between the power supply and the high voltage starter, however the high blocking voltage and high forward current make such a diode impractical. Another possible solution would be to place a suitably large inductor between the power supply and the high voltage starter, however the large currents present during the discharge preclude any practically sized ferromagnetic elements such as transformers or inductors.

A suitable topology can be found in the high voltage starter circuits of electric welders which have similar constraints. A typical high voltage welding starter uses an air coupled transformer between the high current low voltage supply and a high voltage resonant circuit as illustrated below in figure 48.
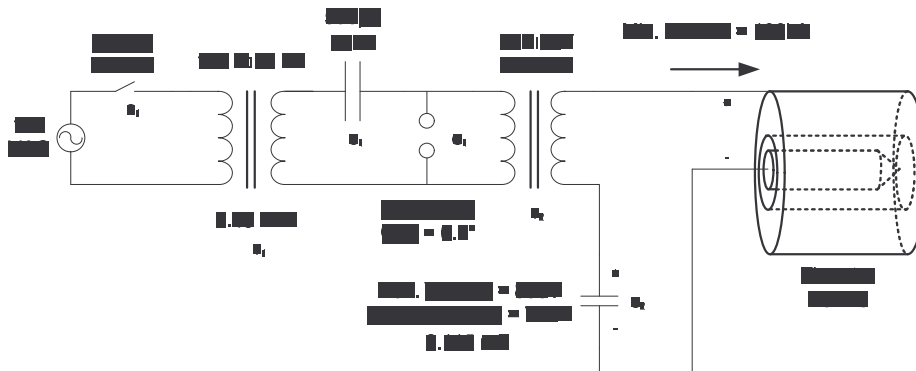
Figure 47: High Voltage Starter Circuit

S_1 is a solid state relay which controls the high voltage ignition circuit that initiates the discharge of C_2, the capacitor bank, into to the thruster nozzle. T_1 is a neon sign transformer rated at 0.45 kVA and 15 kV output. T_1 charges C_1 up to approximately 15 kV, at which point spark gap G_1 breaks down and causes C_1 and the primary of T_2 to oscillate as an LC tank. This high frequency, high voltage oscillation is coupled across the nozzle electrodes via T_2, and causes the gap between the two nozzle electrodes to break down. This provides a conductive path through which capacitor bank C_2 discharges. This topology relieves stresses on the power supply by coupling a high voltage AC component between the power supply and thruster nozzle such that the AC component rides on top of the power supply's DC offset. The air core transformer, though relatively weakly coupling the two windings, will remain unsaturated regardless of the current passing through it.

3.2.3 Nozzle

The main concern for the nozzle was that the cathode survives the extremely high current densities as a result of the entire return current passing through it. Therefore the cathode material was chosen to be Tungsten, which poses both relatively high electrical conductivity and the highest melting point of any metal. Unfortunately, Tungsten is also very difficult to machine and therefore correspondingly difficult to purchase. Its limited availability restricted the cathode to a maximum diameter of 0.25".

Due to its significantly higher volume, the anode does not need to withstand conditions as extreme as those found near the cathode. Also, its larger dimensions tend to require a more easily machined material as well as one that's more readily available and less expensive. Copper was used for the anode due to its availability, high thermal conductivity, and ease of machining.

4 System Model

This section will develop the theory presented earlier into a practical model that will describe the electrical, thermal, and dynamical behavior of the thrusters system previously described. A model for an arbitrary electrical propulsion system is not practical, so the constraints and generalized design will be used. Some parameters are not easily determined a priori, and so some empirical observations will be made before the complete model is constructed.

Previous discussion has justified considering the MPD arc as being in steady state thermal equilibrium, and has adequately modeled the external power supply circuit for the thruster. Therefore, in order to form a complete electrical model of the thruster, the terminal behavior of the MPD arc needs to be specified. Once the electrical behavior of the arc has been specified, deriving the thrust output is only a matter of accounting for the various loss mechanisms and writing an energy balance equation.

4.1 Thruster Operating Conditions

In order to begin establishing an electrical-mechanical model for the MPD arc thruster the basic parameters under which it will operate need to be establish. This section briefly discusses the gross operating conditions which can be expected within the nozzle of the thruster.

4.1.1 Arc Core Conditions

As the arc exists in a high pressure environment (on the order of ATMs) and the arc current is at least several thousands of amperes, it is reasonable to assume that the working gas is at such a temperature that it can be considered nearly completely singly ionized. Taking the ionization fraction as 0.99, the Saha equation can be used to estimate the arc core temperature as not less than 10,000K.

The chamber pressure is roughly equal to the maximum delivery pressure of the Argon regulator, or approximately 160 PSIG (174.7 PSIA = 11.88 ATM.)

4.1.2 Electrode Surface Temperature

Under the assumption of steady state operation and thermal equilibrium, it is known that the cathode and anode will both be at the boiling point of their respective materials. The cathode, made of Tungsten, will reach a temperature of 5,900K, and the copper anode will reach a temperature of 2,800K, though the ionized gas is at a much higher temperature.

4.2 Gas-Dynamic Description

The gas-dynamic description of the MPD thruster behavior considers the interaction between the particles flowing through the arc channel.

4.2.1 Thrust

The thrust developed by an MPD thruster has been derived earlier, and for the geometry shown below
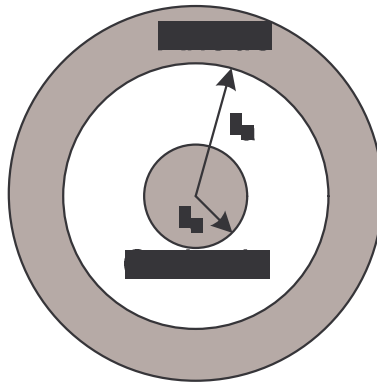
Figure 48: MPD Thruster Nozzle Layout

the thrust generated is a function of the ratio of the anode radius to the cathode radius and the total current [148]

$$F = \frac{\mu J^2}{4\pi} \left(\ln\left(\frac{r_a}{r_c}\right) + \frac{3}{4} \right) \quad (4\text{-}1)$$

Equation 3: Thrust Developed by an MPD Thruster

The thruster under investigation has ratio of radii given as $0.875"/0.25" = 3.5$. Therefore, in order to generate 1 N of thrust requires

$$J \approx \sqrt{\frac{F 4\pi}{\mu \left(\ln\frac{r_a}{r_c} + \frac{3}{4} \right)}} = 2.2 \times 10^3 \, A \quad (4\text{-}2)$$

with thrust rising quadratically at higher currents. At arc currents of 10 kA the thrust generated is 20 N, 50 kA yields 500 N, 75 kA yields 1.13 kN, and 100 kA yields 2 kN.

4.2.2 Anode Material Loss

      The gas-dynamic description of the MPD arc states that the arc current is carried in its entirety by positive ions. Ideally, all of these ions would be provided by the ionized propellant gas; however it may be the case that the propellant gas does not supply enough positive ions. In this case, the additional positive ions required to carry the current may be obtained by either re-circulating propellant gas or by vaporized electrode material. Since the arc current and the propellant flow rate are both known, the rate of electrode erosion can be estimated as constituting the difference between the propellant ion contribution and the total arc current. Under the assumption that the propellant ion contribution is insufficient to carry the entire arc current, the electrode material loss rate can be estimated (for a copper anode) to be

$$\dot{m}_a = \left(J \cdot 6.24 \times 10^{18} - \frac{\dot{m}_A}{M_A^+} \right) M_a^+ \quad (4\text{-}3)$$

with the total mass flow rate through the nozzle given by

$$\dot{m} = \dot{m}_A + \dot{m}_a \quad (4\text{-}4)$$

4.2.3 Propellant Stream

      Evaluating the properties of the propellant stream consists of first looking at the injected propellant gas flow and then the additional copper vapor which is required to carry the remainder of the arc current. Each Argon atom has a mass of $6.64 \times 10^{-26} \, kg$, with a mass flow rate given as 0.0149 mol/s, or $5.96 \times 10^{-4} \, kg/s$. This propellant mass flow rate is able to support approximately 1.4kA of arc current. Any current beyond this value will require vaporized anode material. Therefore, for currents over 1.4kA, the mass flow rate is given as

$$\dot{m} = 5.69 \times 10^{-4} \, kg/s + 3 \times 10^{-7} (I - 1.4 \times 10^3) \, kg/s \quad (4\text{-}5)$$

With the varying propellant stream composition, the average molecular radii and mass will also change. The average molecular radii as a function of arc current (for currents over 1.4kA) is given as

$$r^+ = \frac{r_{AR}^+ (1.4kA) + r_{CU}^+ (I - 1.4kA)}{I} \quad (4\text{-}6)$$

The average molecular mass as a function of arc current (for currents over 1.4kA) is given as

$$M^+ = \frac{M_{AR}^+ (1.4kA) + M_{CU}^+ (I - 1.4kA)}{I} \quad (4\text{-}7)$$

4.2.4 Exhaust Velocity

With the nozzle mass flow rate and thrust know, it is trivial to compute the average particle exhaust velocity. This parameter is important in validating the high specific thrust of the thruster. The average exhaust velocity is given as

$$v_e = \frac{F}{\dot{m}} \quad (4\text{-}8)$$

4.3 Electrical Description

Considering the thruster nozzle terminal voltage as a function of the arc current for a particular nozzle geometry, the behavior of the circuit can be characterized as

$$V_c = L\frac{di}{dt} + ri + e_a(i) \quad (4\text{-}9)$$

where V_c is the capacitor bank voltage

L is the combination of all parasitic inductances in the power supply
r is the combination of all parasitic resistances in the power supply
$e_n(i)$ is the terminal voltage for a nozzle of a particular geometry expressed as a
function of arc current

The most significant challenge is therefore to express the nozzle terminal V/I characteristic. Though the exact representation is not immediately obvious, based on similar applications and some intuition, some qualitative statements about the arc behavior can be made to help guide the development of a more rigorous description.

4.3.1 Cathode Positive Ion Current Density

The high voltage gradient at the cathode indicates that there is a significant space charge which can be estimated using the space charge equation. Cobine presents a similar example where the cathode drop is taken to be the ionization potential of the gas and the cathode drop region is taken to be 1 m.f.p. of an electron in that gas. Cobine gives the likely mean free path of an electron in such a gas to be roughly $6 \times 10^{-7} m$ [149], with the calculation proceeds directly from the space charge equation [150]

$$j_p = 5.35 \times 10^{-12} \sqrt{\frac{e}{m_p}} \frac{V_c^{3/2}}{d_c 2} = 1.44 \times 10^6 \ A/m^2 \quad (4\text{-}10)$$

This result corresponds with a relatively small ion current towards the cathode of $144\ A/cm^2$, and is consistent with the behavior of the welding arc, where the anode receives much more heat than the cathode.

4.3.2 Cathode Electron Current Density

Earlier discussion has established that the cathode in an arc discharge is a thermionic emitter, and that field emissions may also play a role in the electron emission processes. Referring back to the Schottky equation for a Tungsten cathode at its boiling point (5,800K) the current density with a field equal to the ionization potential of Argon over one electron M.F.P.

$$\overline{E} = \frac{e_{column}}{\ell} = \frac{15.75V}{6 \times 10^{-7} m} = 2.63 \times 10^7\ V/m \quad (4\text{-}11)$$

yields a current density of

$$j_c \approx j_n = AT^2 e^{-\frac{\phi_0 e}{kT}} = 6.02 \times 10^5 \times 5{,}900^2\, e^{-\frac{4.4 \times 1.602 \times 10^{-19}}{1.38 \times 10^{-23} \times 5{,}900}} = 3.64 \times 10^9\ A/m^2 \quad (4\text{-}12)$$

or $3.64 \times 10^5\ A/cm^2$. Note that the field strength at the cathode is not strong enough to appreciably contribute to the cathode current density.

4.3.3 Built-in Arc Voltage

An arc between arbitrary electrodes in a particular gas has some minimum voltage which is necessary to maintain the arc, and which over a significant operating region of the arc, dominates the V/I characteristic. As discussed earlier, there exist two very narrow regions at the boundaries of the anode and cathode where there is a voltage drop which is a function of the gas that the arc burns in. This minimum voltage can be expressed as the summation of the anode and cathode voltage drops, which will each be on the order of the minimum ionization potential for the gas in which the arc burns, with the typical voltage being between two to three times the minimum ionization potential. In this case, the gas is Argon, which has a minimum ionization potential of 15.75 eV [151] which should correspond to a minimum arc voltage approximately between 31V and 48V.

4.3.4 Positive Column Voltage

The voltage across the positive column of the arc accounts for the remainder of the arc voltage not accounted for by the anode and cathode fall regions. It is typically characterized by very high conductivity and consequently exhibits a low voltage gradient across it, which requires that the positive ion concentration and electron concentration be very nearly equal. Any detailed particle analysis in the positive column under arc conditions will be cumbersome at best due to the complex interactions that occur in the

highly energetic core, and therefore an energy balance equation may be more practical in determining its electrical properties.

Without analyzing the gas dynamics of the positive column, it is apparent that the energy imparted to the processes occurring in the positive arc column is a result of the electrical charges flowing across it. Therefore, neglecting energy input from the anode and cathode drop regions, the power input to the positive arc column will be the product of the current flowing through it and the voltage across it. Since the overall model assumes steady state operation throughout, calculating the positive arc column voltage can be accomplished by relating the power lost to the electrical power input.

$$P_{column} = e_{c\,olumn}(i) \cdot i = \dot{m}\varepsilon_i + \frac{1}{2}\dot{m}v^2 \quad (4\text{-}13)$$

Here, the loss processes considered are the ionization of the propellant gas flow and the change in kinetic energy of the gas flow. The exact form of the energy balance will be considered later, after the thermal and gas-dynamic models are more completely described.

4.3.5 Total Arc Voltage

The terminal voltage at the thruster nozzle is equal to the arc voltage, which is a function of arc length, propellant gas, electrode material, and arc current. Substantial work has been done to characterize the electric arc, especially the Tungsten arc in Argon for welding applications, and will be adapted to the MPD thruster arc. From earlier work, the form of the V/I characteristic curve for a high current arc is known to be [152]

$$e_a = c_1 i + \frac{c_2}{i} + c_3 i^2 \quad (4\text{-}14)$$

which differs substantially from the low current forms given by Ayrton and Nottingham in that the high current arc V/I curve has a positive slope, whereas the Ayrton and Nottingham equations predict an arc voltage which is essentially independent of the arc current at high currents. Analyzing the positive column conductivity and energy balance equation will yield an equation of this form in order to complete the electrical description.

Observations of welding applications agree well with the earlier estimation of the arc voltage of short arcs at low currents to be about 30V, and work by Ayrton suggests that this voltage can be adjusted by approximately 0.9V per mm of arc length for electrodes in Argon. [153] For arcs approximately 8mm in length, as in this thruster application, this suggests a low current arc voltage of 37V.

Lack of any significant data on very high current (tens of kiloamps) Tungsten-Argon arcs requires some rough estimation on the actual values of the arc voltage in order to find the constants for the high current arc V/I curve. At low arc currents the arc voltage tends to be somewhat higher than at modest arc currents, which can be attributed to smaller and cooler arc columns with correspondingly lower conductivities. This is

supported by work done studying the welding arc, which has established the conductivity of Argon plasma as a function of plasma temperature. [154]
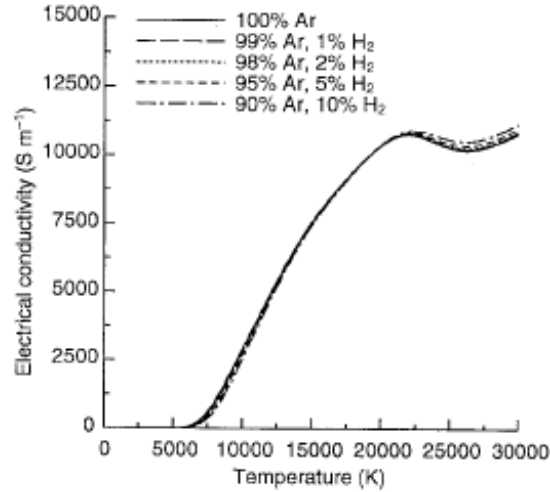
Figure 49: Argon Plasma Conductivity as a Function of Temperature

In the region where the V/I curve begins to show positive slope, perhaps out into several thousands of amps of arc current, the i^2 term begins to dominate due to energy lost to the kinetic energy of the propellant stream.

      In order to calculate the voltage drop across the positive column due to the plasma's resistance, the dimensions of the arc sheet in the nozzle must be established. For a known cathode current density, the total surface area of the cathode covered by the discharge can be calculated as

$$A_{arc} = \frac{J}{j} m^2 \quad (4\text{-}15)$$

.

If the cathode spot is taken to be the surface of a right-cone (i.e. the tip of the cathode) then the thickness of the arc sheet is equal to the height of the cone required to give the cathode spot area, or

$$\ell = \sqrt{\frac{J}{j\pi\sqrt{2}}} \quad (4\text{-}16)$$

and the resistance of the arc core is given as the resistance of the volume between an outer cylinder and the tip of a right-cone. The total resistance of the arc sheet can then be expressed as

$$R_p = \frac{1}{2\pi\sigma r_a \left[\ln(r_a - \ell) + \ln(r_a)\right]} \quad (4\text{-}17)$$

The resistance due to this term is very small, perhaps milliohms or smaller, and so the total voltage across the positive column due to resistive effects is quite small, consistent with voltage gradients observed in the positive columns of arcs.

The other source of energy loss, and consequent voltage drop across the positive column, is kinetic energy given to the plasma. This voltage drop can be estimated by an energy balance. The kinetic energy given to the propellant gas is a function of the exhaust velocity, which can be expressed as

$$v_e = \frac{F}{\dot{m}} \quad (4\text{-}18)$$

and substituting for the force developed in the propellant stream the following relationship is established

$$P = \frac{1}{2}\dot{m}v_e^2 = \frac{1}{2}\cdot\frac{F^2}{\dot{m}} \quad (4\text{-}19)$$

As shown earlier, the force can be expressed as a function of current and substituting yields

$$e_a = \frac{1}{32}\cdot\frac{\mu^2 J^3}{\pi^2 \dot{m}}\cdot\left[\ln\left(\frac{r_a}{r_c}\right)+\frac{3}{4}\right]^2 \quad (4\text{-}20)$$

Noting that the mass flow rate is also a function of current, that relationship can be substituted into the voltage drop equation as follows

$$e_a = \frac{1}{32}\cdot\frac{\mu^2 J^3}{\pi^2}\cdot\left[\ln\left(\frac{r_a}{r_c}\right)+\frac{3}{4}\right]^2 \frac{1}{5.6\times10^{-4}+3.07\times10^{-7}(J-1,400)} \quad (4\text{-}21)$$

for arc currents greater than 1.4 kA. This expression is approximately a function of J^2, and fits the form for a high current arc discharge. One final modification is required to account for all terms in the energy balance equation. The voltage drop due to energy lost ionizing the propellant gas is equal to the power used ionizing the gas (equal to the product of the ionization energy and the mass flow rate) divided by the arc current as shown below

$$e_i = \frac{\dot{m}_a \varepsilon_i}{J} \quad (4\text{-}22)$$

The complete positive column voltage drop can therefore be expressed as

$$e_a = \frac{1}{32} \cdot \frac{\mu^2 J^3}{\pi^2} \cdot \left[\ln\left(\frac{r_a}{r_c}\right) + \frac{3}{4}\right]^2 \frac{1}{5.6\times10^{-4} + 3.07\times10^{-7}(J-1{,}400)} +$$

$$\frac{J}{2\pi\sigma r_a\left[\ln(r_a - \ell) + \ln(r_a)\right]} + \frac{\dot{m}_a \varepsilon_i}{J} \tag{4-23}$$

and the total arc drop is equal to the positive column voltage plus the built-in voltage drop. This final equation is encouraging, since it follows the form given for high current arcs and accounts for the positive slope of the arc at high currents. However, in this form, the $1/J$ term becomes small very quickly, and is inaccurate at low currents which would not otherwise be able to sustain a fully ionized flow, and so it can be omitted without introducing much error.

4.3.6 Electrical Model

Combining the power supply and arc model results in a complete electrical model for the arc behavior in the MPD thruster. Using $r_a = 11.4mm$, $r_c = 3.2mm$, $T = 15{,}000K$, $\sigma = 7{,}500\, S/m$, $j_c = 3.64\times10^9\, A/m^2$, $R_p = 7.33\times10^{-4}\Omega$, and $\ell = 2.49\times10^{-4}m$, the complete model is as shown below in figure 51.
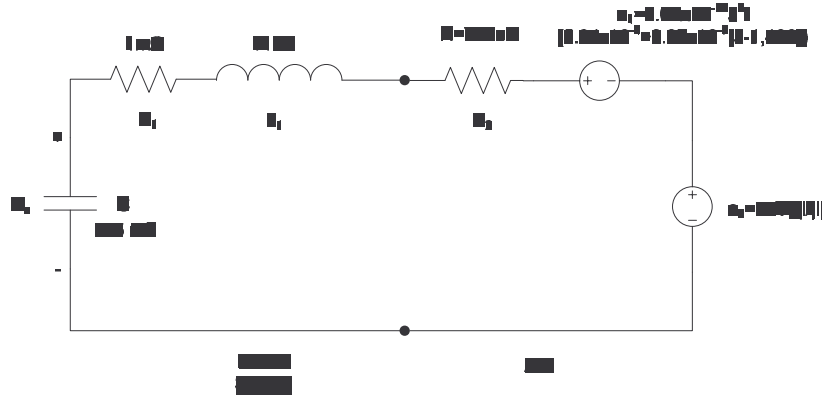
Figure 50: Complete Electrical Model

V_C, measured across C_1, is the capacitor bank voltage, with R_1 representing the equivalent series resistance of the entire circuit, and L_1 representing the equivalent series inductance of the circuit. R_2 represents the resistance of the arc formed in the thruster nozzle, e_1 represents the voltage developed across the arc as a result of electrical energy converted to kinetic energy in the propellant stream, and e_2 represents the built in voltage of the arc.

4.4 Thermal Description

This section will discuss the various heat transfer mechanisms, and the relative heating of various components in the thruster nozzle. Coincidently, the use of Argon as the propellant gas greatly simplifies the thermal analysis in the thruster nozzle since it is monatomic and therefore does not transfer a heat of dissociation away from the arc core towards the electrodes, nor does it carry heat away from the electrodes well compared to other mechanisms at work in the nozzle. Therefore, the effects of convection within the arc core can be considered negligible compared to joule heating and electron/ion bombardment without introducing much error. The results of this section will also be applicable to the energy balance equation discussed in the positive arc column section.

4.4.1 Cathode Heating

Cathode heating occurs by positive ion bombardment from ions created in the positive column and anode drop region, which are then accelerated through the cathode drop region and impact the surface of the cathode. The heat delivered to the cathode is critical to maintaining the temperature of the cathode, which in turn causes it to emit electrons thermionically and sustain the arc column. The heat delivered to the cathode can be estimated as the product of the positive ion current through the cathode drop region and the cathode drop potential. From the electrical description, the thermal power density delivered to the cathode is

$$P_c = j_c V_c = 1.44 \times 10^6 \ A\big/m^2 \cdot 15.75V = 2.27 \times 10^7 \ W\big/m^2 \quad (4\text{-}24)$$

or $2.27 \times 10^3 \ W\big/cm^2$. This heat flux is not distributed over the entire surface area of the cathode, rather just that portion that is enclosed by the arc core, and corresponds to a total area which can be computed through the total current and the cathode current density. Accordingly, only a small portion of the cathode is likely to be included in the arc core, corresponding to a "cathode spot," perhaps only a few mm^2. Due to the refractory nature of the Tungsten cathode, little material is expected to be lost during thruster operation. Furthermore, the strong magnetic field near the cathode tip is expected to provide some measure of protection against excessive ion impacts, and should further limit cathode material loss.

4.4.2 Anode Heating

Anode heating is primarily caused by electron bombardment from electrons thermionically emitted from the cathode. The energy gained by the electrons as they fall through the anode drop region is transferred to the anode material. Therefore, the thermal power delivered to the anode is equal to the product of the electron current to the anode and the anode drop potential. With electrons carrying the majority of the current, likely on the order of thousands of amps, and the anode drop potential on the order of the ionization potential of Argon, the thermal power delivered to the anode will be extremely high. Unlike in the cathode, the temperature of the anode does not contribute to any

processes critical to maintaining the arc, but it will cause a significant amount of copper to vaporize and join the propellant flow, adding to the mass flow rate and developed thrust. Therefore, estimating the anode heating and material vaporization rate is important in calculating the total thrust generated. The thermal power delivered to the anode can therefore be expressed as

$$P_a = J \cdot V_a \approx J \cdot 15.75V \leq Pa \leq J \cdot 31.5V \quad (4\text{-}25)$$

The surface area to which this power is delivered is less well defined than for the cathode since the electrons are not constrained to any particular return path, and may travel down the plasma jet for some distance before returning even outside of the luminous plume. A thermal analysis can be used to estimate the mass of anode material lost to vaporization, however the gas-dynamic model presents a shortcut to calculating the rate of mass loss, which will be presented later.

4.4.3 Propellant Flow

The rate of energy input to the propellant flow is dependant on the rate of propellant flow, and thus the rate of propellant flow needs to be established before further thermal analysis. Compressible flow theory dictates that the narrowest cross section along a compressible flow and the ratio of inlet and outlet absolute pressures will set the mass flow rate of the propellant. In this case, the gas solenoid in the gas injection system will have the smallest cross section of flow, and will therefore set the maximum mass flow rate. This was calculated earlier for Argon to be 0.6 grams/s, equal to 0.0149 mol/s. In order to fully ionize the flow, the energy of ionization must be transferred to the propellant mass. The first ionization energy of Argon (only the first ionization energy is considered since the flow is assumed to be singularly ionized) is given as 1520.6 kJ/mol. [155] Accordingly, the power input for maintaining full ionization of the propellant flow is given by

$$P_{ion} = \dot{m}\varepsilon_i = 0.0149\,mol/s \times 1520.6\,kJ/mol = 22.657kW \quad (4\text{-}26)$$

Therefore, at the specified propellant flow rate a portion of the energy input to the thruster is likely to be lost on ionization, since the ionization itself does not impart any thrust in the MPD thruster. Significant thermal losses like this do suggest that a properly designed nozzle may be able to recover some of the thermal losses as thrust. This mode of operation is more accurately described as an arcjet thruster.

Furthermore, at arc currents of several thousands of amps the required voltage drop across the positive column in order to supply the $22.657kW$ is only a couple of volts, and at currents above several tens of thousands of amps, is probably negligible compared to the total anode and cathode drops.

4.5 System Model

With the various mechanisms at work in the arc current identified and characterized, a complete model of the electro-mechanical behavior of the MPD thruster can be constructed and evaluated. The electrical and thrust models can be combined to yield an electromechanical model for the thruster as shown in figure 52.
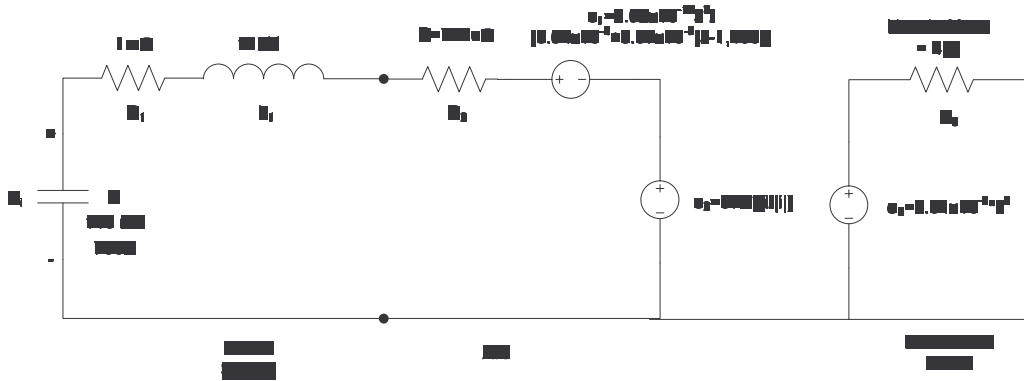
Figure 51: Electromechanical Model

V_C, measured across C_1, is the capacitor bank voltage, with R_1 representing the equivalent series resistance of the entire circuit, and L_1 representing the equivalent series inductance of the circuit. R_2 represents the resistance of the arc formed in the thruster nozzle, e_1 represents the voltage developed across the arc as a result of electrical energy converted to kinetic energy in the propellant stream, and e_2 represents the built in voltage of the arc. e_f represents the value of the instantaneous force developed by the thruster, and R_3 represents the mass of the nozzle assembly. In this electrical analogy to the mechanical phenomena, the current flowing through R_3 is the acceleration of the cart.

5 Simulation

With the electro-mechanical model of the MPD thruster fully specified, simulating its performance is trivial using a SPICE circuit simulator. The following simulations were conducted with an initial capacitor bank voltage of 700V and topology as developed in earlier sections. The SPICE model for the thruster can be found in the appendix.

5.1 Simulation Results

The simulated current discharge through the thruster arc is shown in figure 53
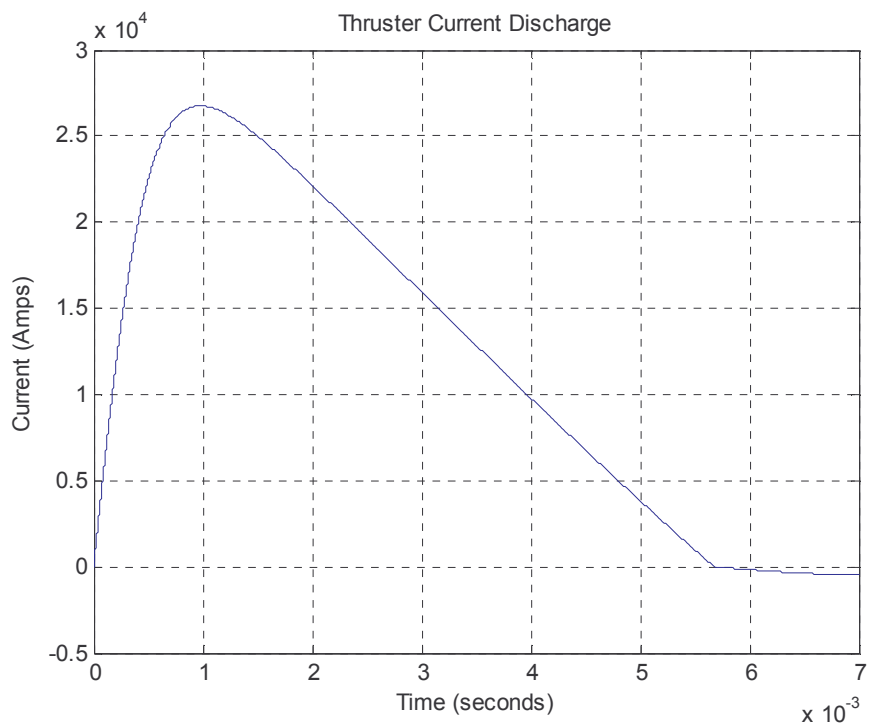

Figure 52: Thruster Current Discharge, Simulated

The force developed by the current discharge is shown in figure 54
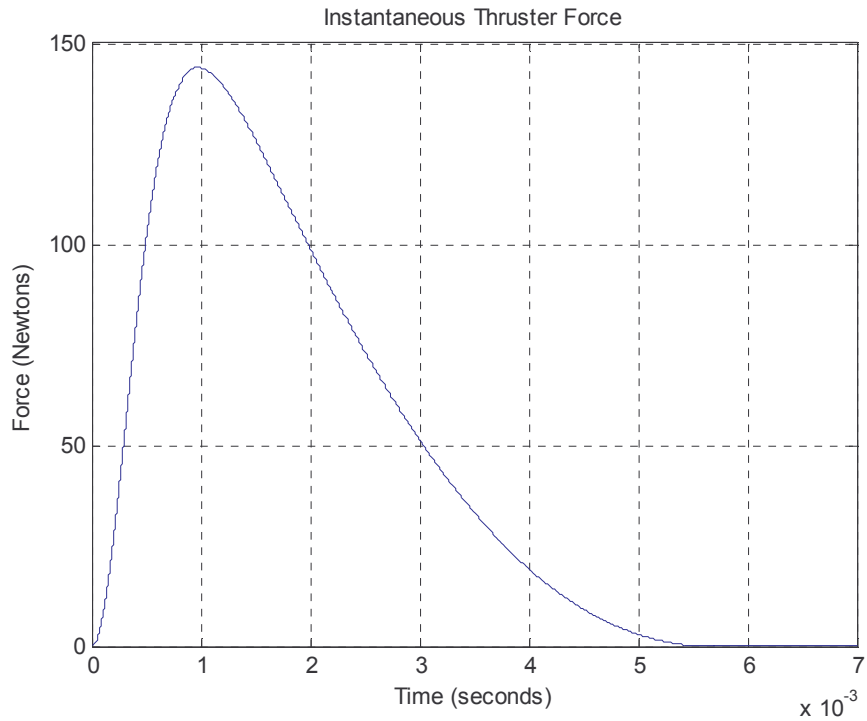
Figure 53: Instantaneous Thruster Force, Simulated

Integrating the force over time yields the total developed impulse shown in figure 55
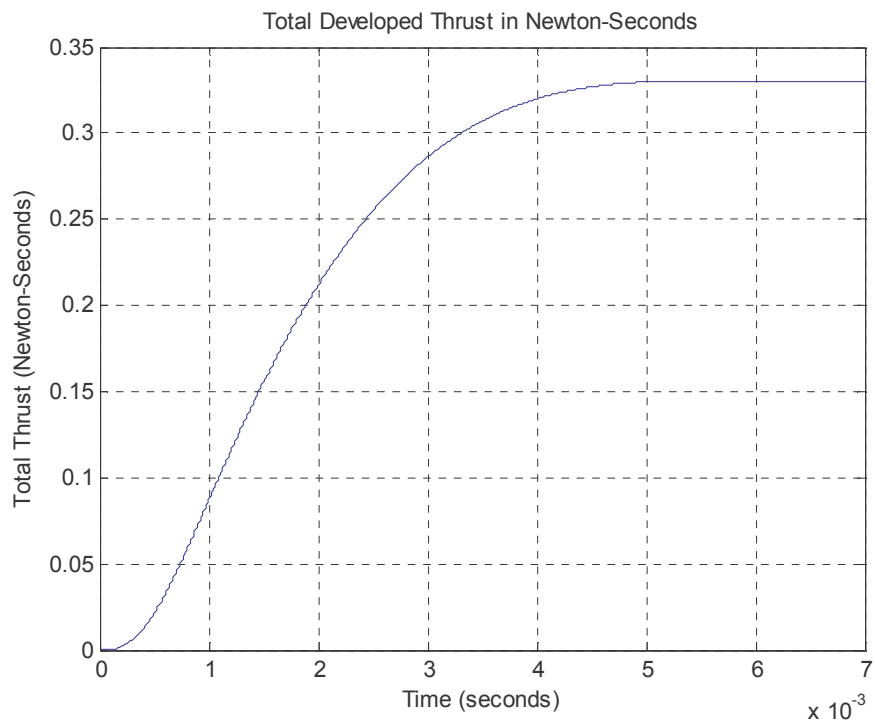
Figure 54: Total Developed Thrust in Newton-Seconds, Simulated

5.2 Simulation Analysis

The results of these simulations provide some valuable insight into the design and estimated performance of this thruster.

5.2.1 Arc Current

The short duration of the discharge is expected due to attempts to minimize resistance and inductance throughout the system, and corresponds to very high peak power consumption. This suggests high performance of the thruster as well. Below, the instantaneous power dissipation of the thruster arc is shown, with a peak dissipation of just less than 14 MW.
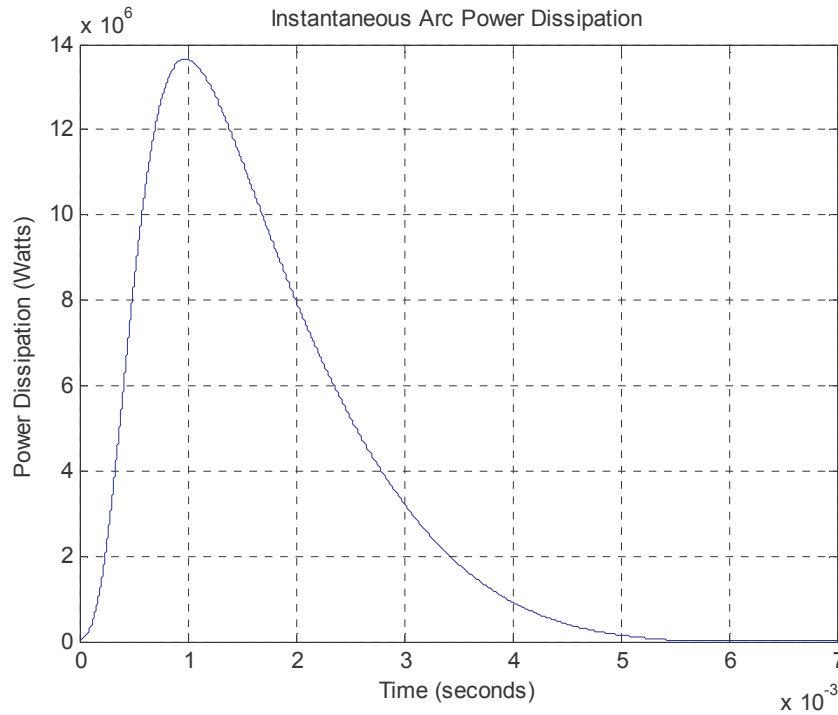
Figure 55: Instantaneous Arc Power Dissipation, Simulated

5.2.2 Instantaneous Force

Using the estimated mass flow rates, the specific impulse of this device can be estimated from this simulation. Using equation 4-18, the mass flow rate at the instant of peak force can be calculated as

$$\dot{m} = 5.69 \times 10^{-4}\, kg/s + 3 \times 10^{-7}(J - 1.4 \times 10^{3})\, kg/s = 8.28 g/s \quad (5\text{-}1)$$

From the mass flow rate equation 4-18 can be used to calculate the peak exhaust velocity, which evaluates to

$$v_e = \frac{F}{\dot{m}} = \frac{145}{0.00828} = 1.81 \times 10^4 \ m/s \quad (5\text{-}2)$$

This yields a specific impulse of 1,813 s, which would correspond to levels of performance found in magnetogasdynamic thrusters, but falls far short of the expected specific impulses of above 10,000 s for magnetoplasmadynamic thrusters.

5.2.3 Total Thrust

The total thrust imparted to the thruster in this simulation is approximately 0.33 Ns. This is again in agreement with the results for magnetogasdynamic thrusters, but falls short for the thrust that would be expected for the same mass if accelerated by a magnetoplasmadynamic thruster.

5.2.4 Optimal Inductance

The strong dependence of the force developed in the thruster on arc current suggests that the inductance in the power supply circuit may have a strong effect the thruster's performance. Here, several simulations are run with varying values for the parasitic inductance, and the total developed thrust for each case is compared in order to determine the dependence of the inductance on performance.
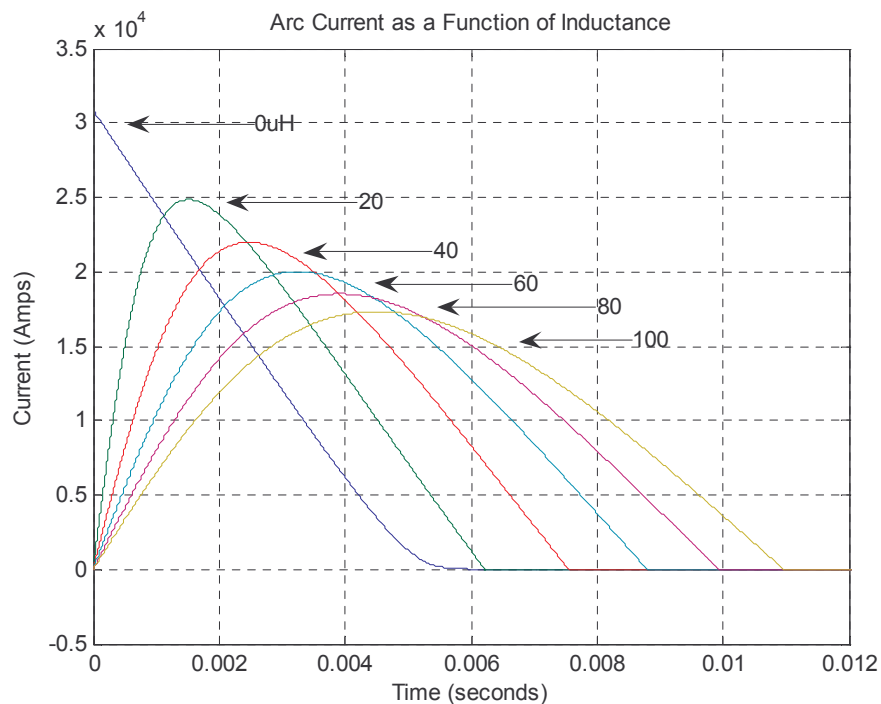
Figure 56: Arc Current as a Function of Inductance

Comparing the total thrust developed for each value of inductance yields the following result
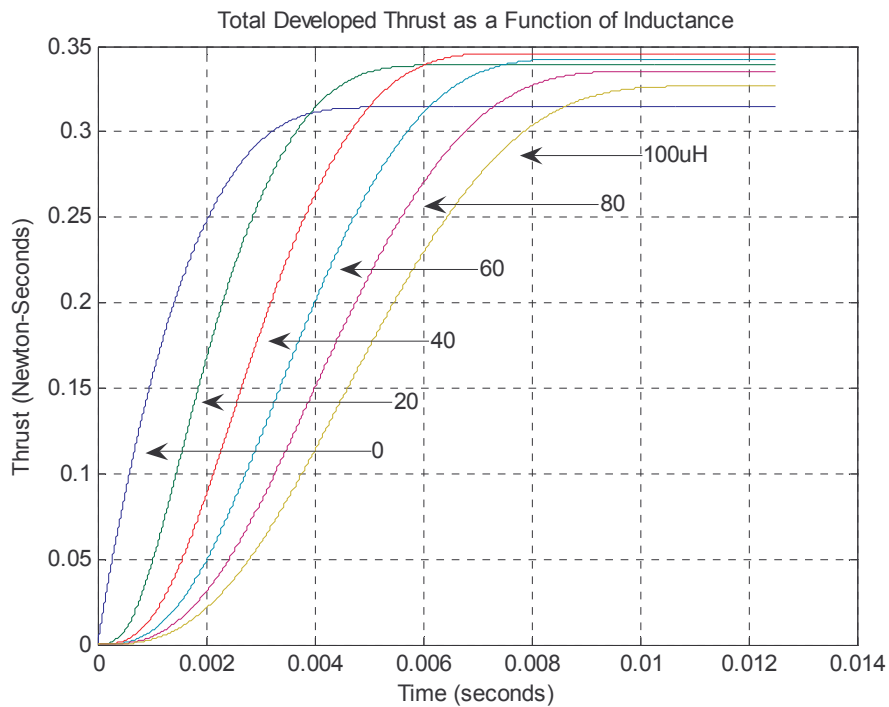
Figure 57: Total Developed Thrust as a Function of Inductance

The peak developed thrust appears to occur at roughly 40uH. Note that these simulations do not allow negative arc current, due to the limitations on the electrolytic capacitors in the capacitor bank. The first indications of LC oscillations occur at roughly 9uH, indicating the actual value of 11uH is probably very close to the upper limit on the inductance before oscillations become a concern.

6   Performance and Results

Simulations have suggested that the design presented in this thesis is already near optimal in terms of managing parasitic elements in the power supply, however real world validation of the model is necessary to ensure that these predictions are accurate. Accordingly, this section presents the results of measurements made during the operation of the thruster design previously proposed

6.1 Test Setup

The test setup was designed to measure the force developed in the thruster nozzle during operation. In order to make this measurement, the nozzle was mounted to a cart on low friction tracks and long flexible cables were used to connect the power supply so as to provide a platform that was as nearly free from friction or spring effects as possible. The attachment of an accelerometer to the cart allowed the unimpeded acceleration of the cart to be measured, from which the instantaneous force could be computed. The test rig is shown below.
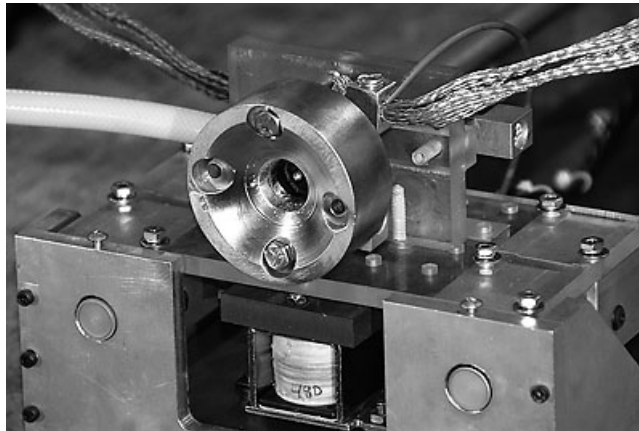
Figure 58: Thrust Test Rig

6.2 Cold Flow

The propellant flow through the thruster nozzle, even when not electro-magnetically accelerated, causes a reaction force that imparts some thrust to the nozzle. The cold flow thrust is superimposed over the thrust due to electromagnetic acceleration when the thruster is operated using magnetogasdynamic interaction, and needs to be removed in order to accurately analyze the thruster operation. The cold flow thrust contribution was measured using the same test rig designed for full MPD operation by recording the acceleration of the test cart over the propellant pre-flow, discharge, and post-flow periods as shown in figure 60.
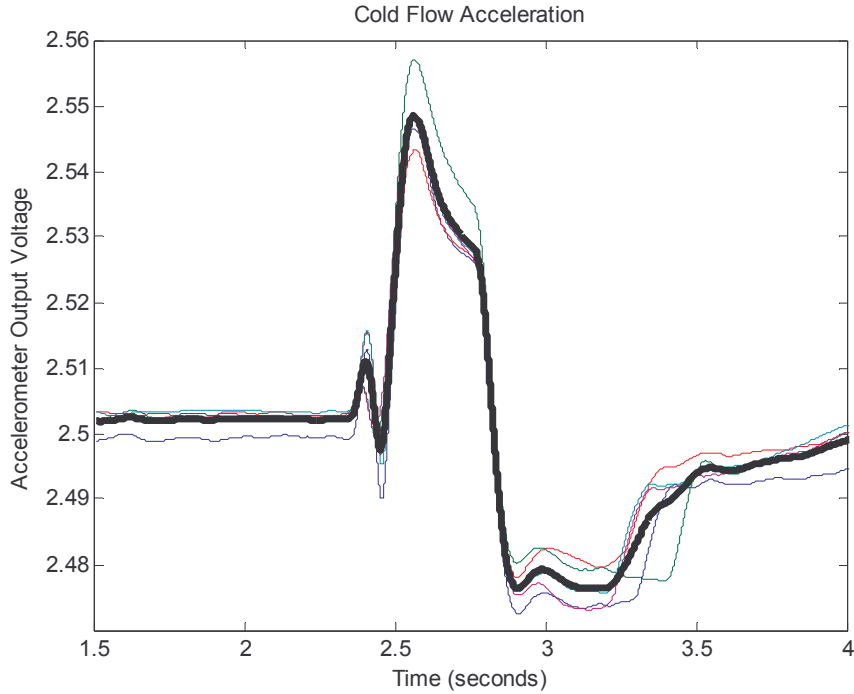
Figure 59: Cold Flow Acceleration

The data for each of the five runs are shown as thin lines, while the average of the 5 runs is shown in thick black. The change in the accelerometer output voltage from rest to maximum acceleration is taken to be 0.037V, and with the accelerometer's sensitivity given as 0.25 V/G, this corresponds to a cold flow acceleration of 0.148 G. The mass of the test cart and nozzle was measured to be 14.17 kg, which yields a cold flow thrust of 2.1 N.

These results were obtained by filtering the raw data obtained from measurements in order to reduce noise and oscillations due to mechanical resonances in the accelerometer mounting hardware. A third-order Butterworth filter with a cut-off frequency of 5.25 Hz was applied to the raw data in order to generate this graph.

6.3 Thruster Operation Results

Three parameters of the thruster were recorded during operation for comparison to the simulated results – capacitor bank voltage, thruster current, and thruster acceleration. First, the capacitor bank voltage is considered and shown below in figure 61.
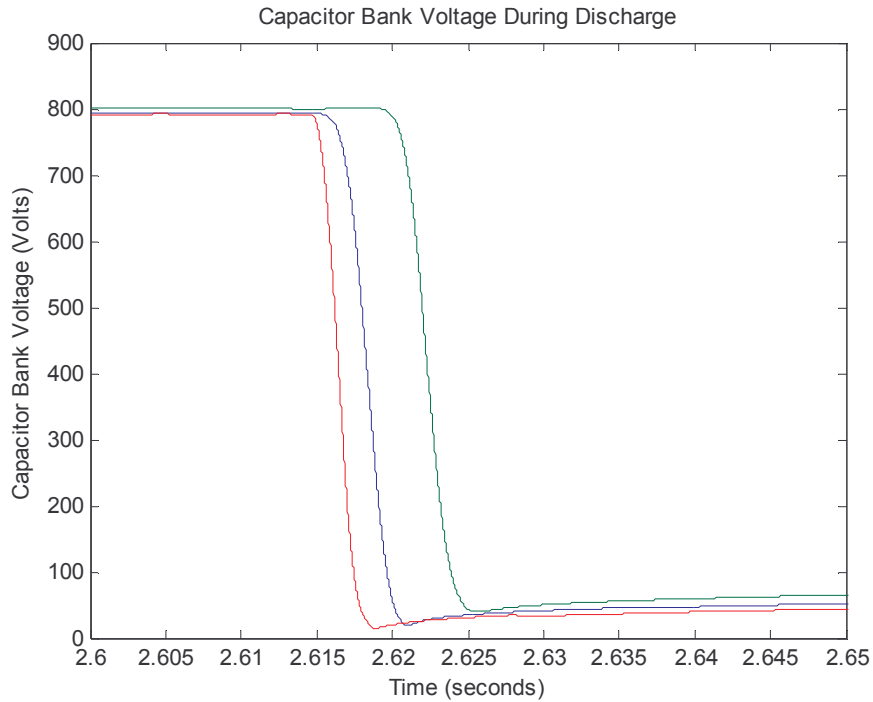
Figure 60: Capacitor Bank Voltage During Discharge

As expected, the capacitor bank completely discharges in a few milliseconds, consistent with earlier simulations. It is also significant that there is no indication of oscillations in the capacitor voltage which reaches some minimum value above zero volts.
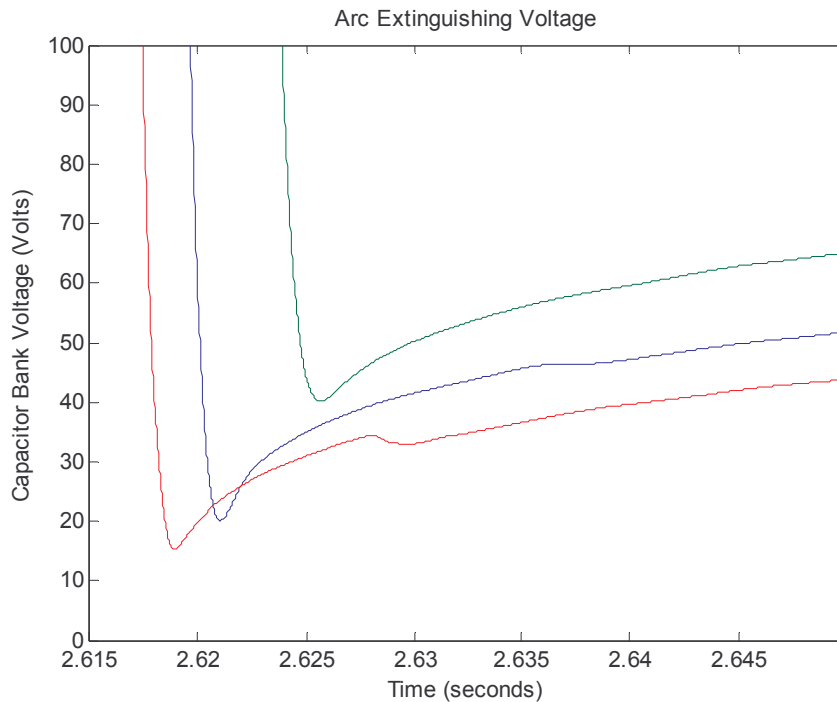
Figure 61: Arc Extinguishing Voltage

From this figure the voltage at which the arc extinguishes can be estimated as between 15 and 45 Volts, also in agreement with the model used. The arc current was also recorded, and corresponds to short discharge times indicated by the capacitor bank voltage discharge times observed above. The discharge currents are shown below in figure 63.
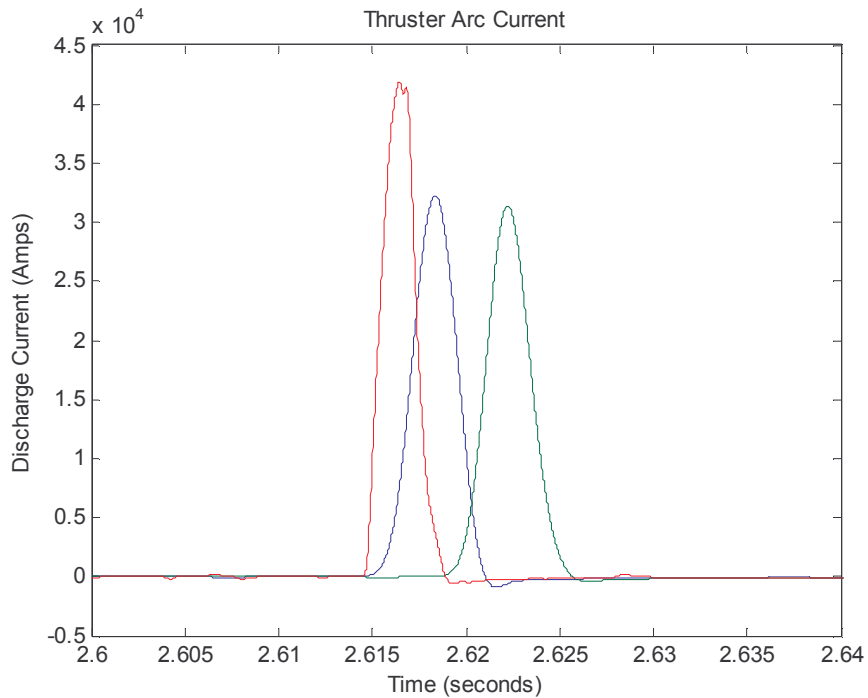
Figure 62: Arc Discharge Current

From this graph, the discharge times appear to be between 4 and 6 ms, with peak currents of 42 kA, 32.4 kA, and 31.2 kA respectively. These results are higher than the predicted discharge currents, and accordingly are somewhat shorter in duration as well. The thrust produced by these discharges were measured by an accelerometer, whose output corresponds to the reaction force on the test cart. Below, the accelerometer's output is shown for each of the three test runs, with the arc current superimposed in order to show the time relationship between the arc current and accelerometer's output.
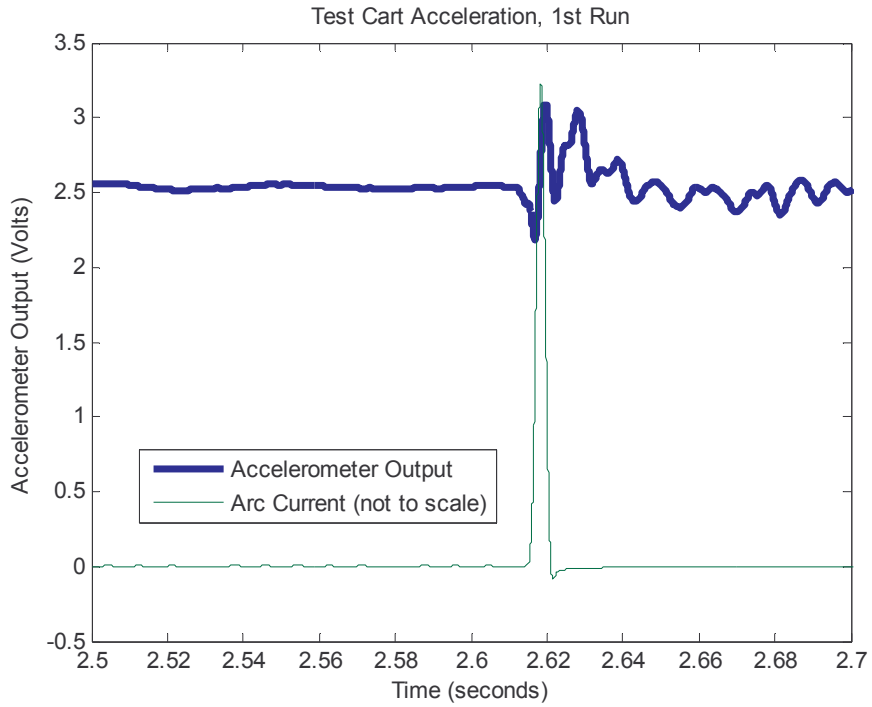
Figure 63: Test Cart Acceleration, 1st Run

For the first test run, the peak current of 32.4 kA corresponds to a peak accelerometer output of 3.14V, a change of 0.635V, or 2.54G. This corresponds to a peak thrust of 36N.
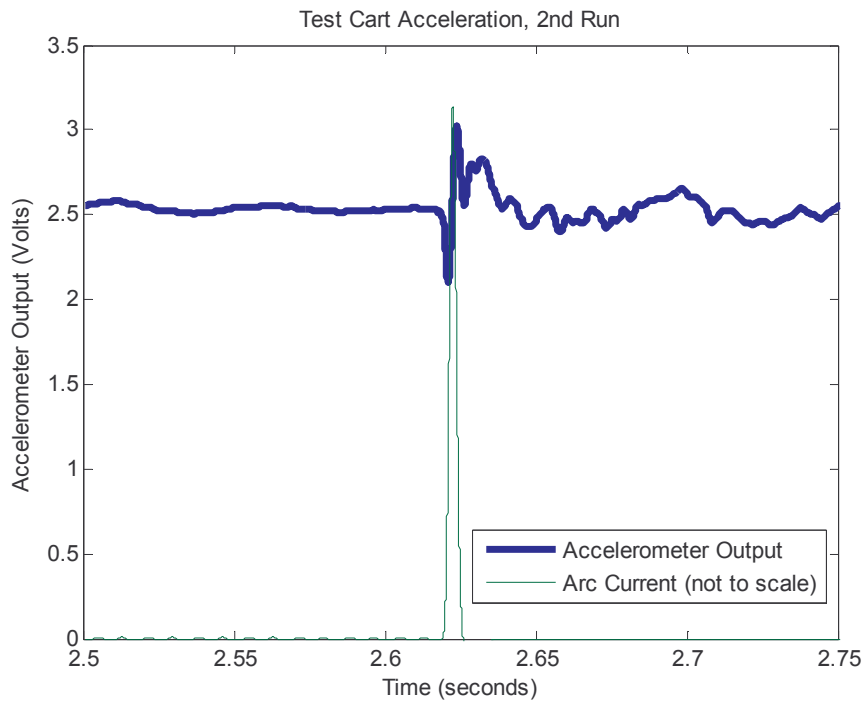
Figure 64: Test Cart Acceleration, 2nd Run

For the second test run, the peak current of 31.2 kA corresponds to a peak accelerometer output of 3.04V, a change of 0.536V, or 2.14G. This corresponds to a peak thrust of 30.4N.
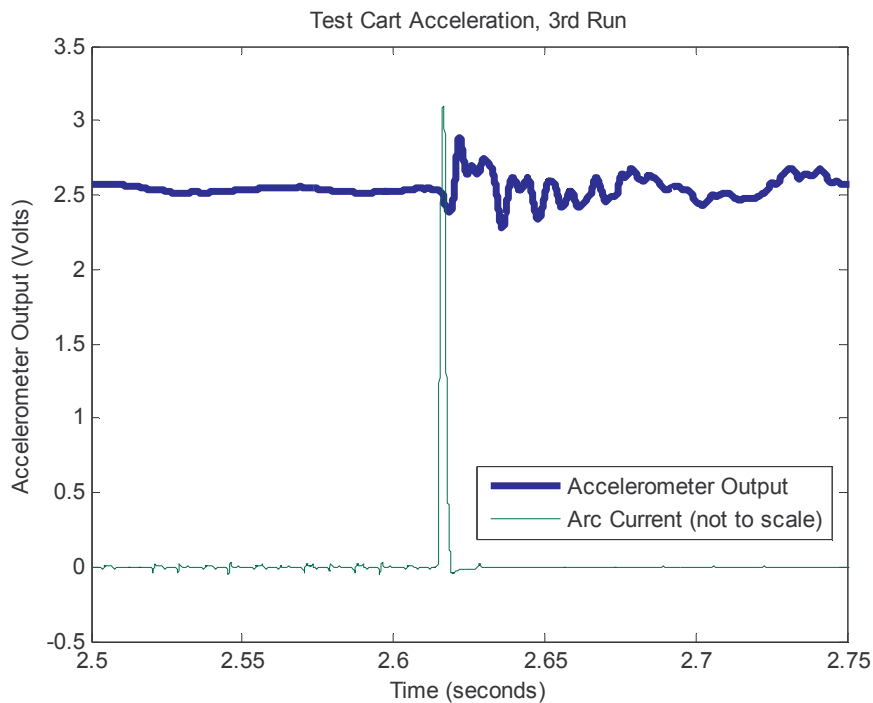
Figure 65: Test Cart Acceleration, 3rd Run

For the third test run, the peak current of 42 kA corresponds to a peak accelerometer output of 2.91V, a change of 0.406V, or 1.62G. This corresponds to a peak thrust of 23N. Based on these results, the cold flow acceleration does not represent a significant portion of the thrust developed.

6.4 Electrode Erosion

An important aspect of the thruster operation is its useful lifespan, mainly limited by electrode erosion caused by the large arc currents. Prior to firing, a new cathode was machined and the anode surface was polished, as shown below.
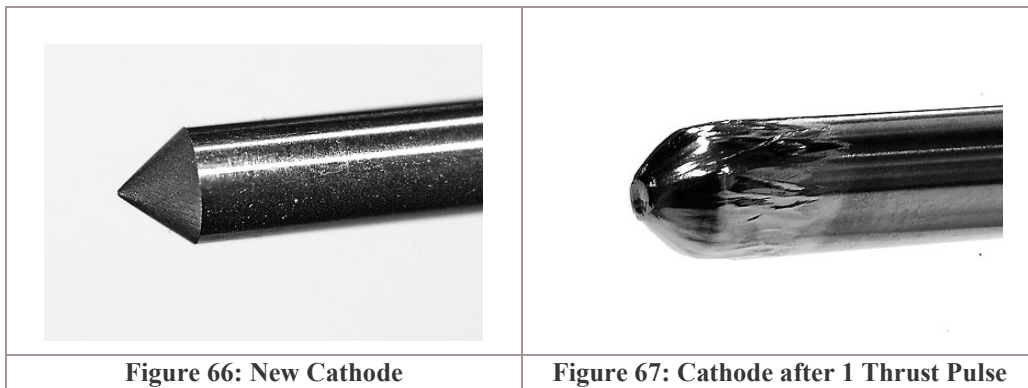
| **Figure 66: New Cathode** | **Figure 67: Cathode after 1 Thrust Pulse** |

77

Clearly, significant heat was accumulated at the cathode and material was lost from the cathode during the period of one pulse. From these photographs, it is apparent that most of the surface of the cathode, as far back as a centimeter, was molten to a significant depth in the material. The pattern of channels in the cathode tip indicates a flow of material in a stream-wise direction, and the truncated and dimpled tip indicate a strong cathode spot generating much of the electron flux, as shown in figure 69.

Figure 68: Cathode Spot at Tip

Considering the amount of relatively high melting point cathode material that was lost, it seems likely that the anode lost significant amounts of material as well, and that was observed to be the case as well as shown in the figure 70 and 71 below.
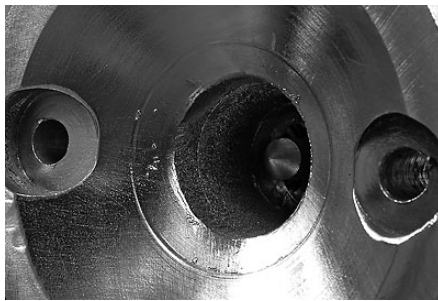
Figure 69: Polished Anode Surface   **Figure 70: Anode Material Loss**

From these photos it appears that a significant amount of material is lost from the inside edge of the anode, and spread out along the surface of the anode. Some of the material lost from the inner anode is also ejected along a stream-wise direction, as can be seen in figure 72.
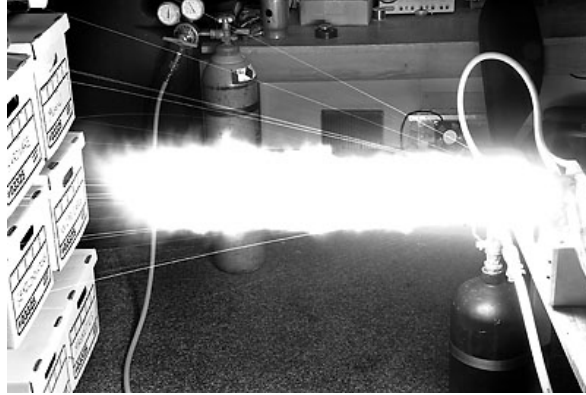
Figure 71: Exhaust Plume

The thin streaks originating at the nozzle are fragments of electrode material ejected along with the propellant gas, indicating further loss of anode material.

7 Conclusions

The primary goal of this thesis was to construct a theoretical model for an MPD arc thruster and verify it against experiment. From the results of simulation and experimentation, the relative success can be summarized in the table below.

	Peak Arc Current	Peak Force (measured)	Peak Force (predicted)
Simulated	27 kA	-	140 N
Run 1	31.2 kA	30.4 N	195 N
Run 2	32.4 kA	36 N	210 N
Run 3	42 kA	23 N	353 N

Figure 72: Results Summary

Clearly, the performance of the nozzle differs greatly from the simulated model, an effect which above all else is probably due to the fact that the thruster was operated at atmospheric pressure, as opposed to the original observations of the MPD phenomenon at pressures on the order of a few mmHg.

7.1 Deviations from Model

The following sections will attempt to address the discrepancies between the predictions and results and explore the assumptions that lead to those predictions.

7.1.1 Deviation from Particle Description

As mentioned previously, the conditions prevailing inside of the arc differ greatly from the conditions assumed under the particle description of the MPD arc. Primarily, the particle description assumes nearly collisionless motion of the positive ions as they move toward the cathode. Previous calculations have suggested an approximate mean free path on the order of $10^{-6} m$ under atmospheric conditions, resulting in many collisions occurring across even very short distances. If the pressure is lowered to 5 mmHg (for example) the mean free path increases to on the order of centimeters, and performance is likely to approach earlier predictions..

Another effect that the particle description suggests is the magnetic shielding of the cathode from positive ion collisions by the strong magnetic field. The magnetic field at the surface of the cathode (radius of 0.125") due to a current of 35 kA is roughly 2.2 T. Assuming a sonic speed at 10,000K in the arc of approximately 6 km/s [156] the gyro radii of a positive ion of Argon is approximately 1 cm (2-47). This gyro radius is too large to allow the ions to be turned stream-wise without colliding with the cathode. The ions can therefore be expected to deposit significant amounts of energy and, as observed in figure 69, experience significant melting and loss of material.

The effects of these deviations from the particle description will have the net effect of reducing the total energy imparted per unit mass flow through the nozzle. This

would tend to lower the arc voltage due to electrical energy being transferred to kinetic energy, and as a result larger currents would be expected with lower total thrust. This is what was observed in the results section, and is therefore a likely explanation for the lack of thrust compared to the simulations.

The particle description also suggests that the entire current is carried by positive ions derived either entirely from the propellant stream, or in the case of insufficient propellant flow, propellant and electrode material. The model used in this thesis assumed that all current beyond what the propellant flow could sustain was supplied by ions removed from the anode; however this assumption seems to be erroneous as this would require anode material to be removed at a rate of 23 grams per second. By observation, this material removal rate appears too high for the quantities of material observed to have been removed. It is therefore likely that some portion of the arc current is sustained by recirculating gas in the arc.

7.1.2 Operation as an Arcjet Thruster

If the thruster cannot operate as a MPD thruster under atmospheric conditions, then an alternate model for the generated thrust needs to be identified that can more accurately model the thruster's behavior. In this case, the arc heating of the propellant will result in some portion of the thermal energy being recovered by expanding the propellant flow. This corresponds to the arcjet mode of operation, where thrust is generated as in a conventional chemical or nuclear rocket. If the thruster is assumed to be operating as an arcjet, then it should perform as predicted by the background section on arcjets. Accordingly, the maximum exhaust velocity for this thruster, assuming an exhaust temperature of 10,000 K with a specific heat of $1,250 \, J/kg \cdot K$ as shown in figure 74 is calculated to be $5,000 \, m/s$ (2-58) [157].
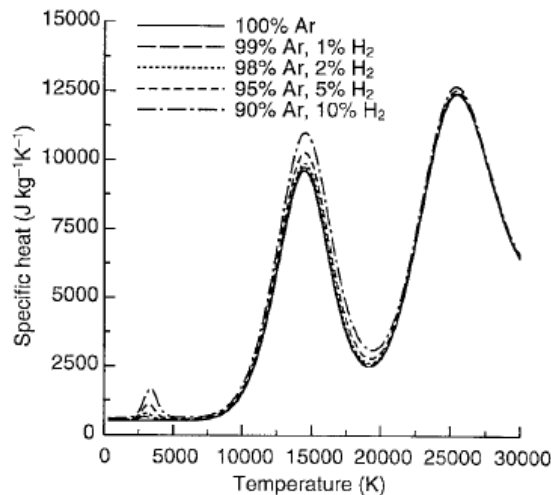

Figure 73: Temperature Dependant Specific Heat for Argon

81

Assuming a flow rate closer to that of the propellant flow (i.e. no contribution of copper vapors) the thrust can be computed to be approximately 10 N. If some contribution to propellant flow by copper is admitted, then the arcjet model predicts thrust on the order of those observed during thruster operation. Therefore it is likely that the thruster operates as an arcjet under atmospheric conditions.

7.2 Suggestion for Improvements and Further Research

The discrepancy between the theoretical model and the observed performance suggests significant improvements can be made to the design and testing of this class of thruster. These opportunities for improvement and further research are listed below.

7.2.1 Operate as a Magnetoplasmadynamic Thruster

The fact that the thruster did not operate as a magnetoplasmadynamic thruster means that the model developed in this thesis, while insufficient to describe operation at atmospheric pressures, was not evaluated at all under MPD operation. Therefore, operating the thruster in a vacuum chamber at pressures conductive to MPD operation would allow an opportunity to verify the theoretical model.

7.2.2 Mass Flow Matching

The possibility of large amounts of anode material being consumed in the arc suggest that the propellant mass flow and arc current need to be more closely matched. This may be accomplished either by increasing the mass flow drastically, or reducing the arc current. The former seems preferable, though is limited by practical gas delivery systems.

7.2.3 Steady State Operation

The pulsed mode of operation provides some complications in the measurement and analysis of the operation of the thruster which can be partially eliminated by using a pulse forming network to tailor the current pulse delivered to the arc. Ideally, a square wave pulse with a relatively constant peak current would be applied to the arc, resulting in the thruster operating in a steady thermal and electrical state. If a reasonable solution to the problem of matching the pulse forming network's characteristic impedance to the arc's characteristic impedance, then this would be a preferable solution.

Appendix A: Ratio of Partition Functions for Argon

[158]

Temperature (K)	$f_+^{\,i}\big/f_A^{\,i}$
5000	5.325
6000	5.419
7000	5.490
8000	5.591
9000	5.591
10.000	5.628
11,000	5.658
12,000	------
13,000	5.707
14,000	5.726
15,000	5.744
16,000	5.759
17,000	5.773
18,000	5.736
19,000	5.799

Appendix B: A and b_0 Constants for Various Materials

[159]

A in amp./(sq. cm.)(deg.^{2}); ϕ_0 in volts; [ ] = uncertain; __ = best outgassed value; b_0 in degrees Kelvin

Material	A	ϕ_0 Thermionic	ϕ_0 Photoelectric	b_0	Boiling point, °C.	Effect of gas on ϕ_0 Increase	Effect of gas on ϕ_0 Decrease
Ag	60.2	4.08	4.73–3.85	......	1950	H_2	O_2, N_2, CN
Al	....	....	4.56(600°) 3.57[2.5–3.6]	......	1800		
Al_2O_3	1.4	3.77	....	43,700			
Au	60.2	4.42	4.73 (740°) (1050°) 4.82 (20°)	......	2600	H^+	Air
BaO	2.5	3.44–1.66	....	19,700			
Bi	....	....	4.4–4.0	......	1450	......	Air
C	5.93	3.93	4.82[4.7]	46,500	4200	NH_3, H_2, CO_2, Air	
Ca	60.2	3.02–2.24	[2.7]	26,000	1170		
CaO	25.7	2.24	....	26,000			
Cd					767		
CdO	1.65×10^{-6}	2.43					
Co			4.25–4.12		3000		
Co_2O_3	2.17×10^{-2}	4.06					
Cu	65(1316°)	4.38	4.5–4.1	......	2300		
CuO	1.55×10^{-8}	1.76					
Cs	162	1.81	1.9	21,000	670		
Fe	....	....	4.72–4.2	......	3000	O_2, H_2	
Fe_2O_3	1.16×10^{-2}	3.82					
Hf	14.5	3.53	....	41,000			
Hg	....	.	4.53	......	357	Wax vapor H_2O vapor	H_2O (trace)
K	....	....	2.25–1.76	......	760	H_2, O_2, H_2O, S, NO	
Li	....	....	2.9–2.1	......	>1220		
Mg	....	....	[<3.4]	......	1110		
MgO	1.1×10^{-5}	....	3.19	33,100			
Mo	60.2	4.41–3.48	4.33–3.22	51,300	3700	H_2O	
Na	....	....	2.46–1.90	......	880	O_2, S, H_2O	
Ni	26.8	2.77	5.01–4.12	32,100	2900	H_2O	Air, O_2
NiO	9.1×10^{-2}	4.87					
Pb	....	....	[4.1–3.5]	......	1620		
Pd	....	4.99	4.96	......	2200	H_2, O_2	O_2
Pt	1.7×10^4	6.27	6.3 × 4.40	72,500	4300	H_2, NH_3	O_2
Rb	....	....	2.2–1.8	......	700		
Rh	....	4.58	4.57 (20°)	......	......	....	H_2, O_2
SiO_2	5.0	4.58					
Sn: β	....	....	4.5				
γ	....	....	4.38				
Liquid	....	....	4.21	......	2260		
SrO	6.9	1.99	....	23,100			
Ta	60.2	4.18–4.07	4.05 (20°) 3.92 (700°)	47,200	......	H_2O	
Th	60.2	3.35	[3.6–3.3]	38,900			
ThO_2	0.016	2.94	....	34,700			
W	60.2	4.52–4.40	4.80–4.52	52,400	5900	H_2O	O_2
Zn	....		3.68–3.32	......	907		
Zr	330	4.13	....	51,000	>2900		
ZrO_2	0.35	3.4	....	39,400			

Appendix C: Gas Solenoid Specifications
[160]

STANDARD 1/4" THROUGH 2"
"CLASSIC" SOLENOID: SO, SR, SS, SY

AIR FLOW RATINGS AND VALVE SHIFT TIME:

Test for the determination of flow-rate characteristics conforms to ISO 6358, *Pneumatic fluid power - Components using compressible fluids - Determinations of flow-rate characteristics*. These tests were conducted on AAA valves at the Fluid Power Institute Testing Laboratories of the Milwaukee School of Engineering.

RATED FLOW. Flow factor tests were made with the valve outlet vented to atmosphere and flow in the sonic region. The average flow factor was calculated from tests over a range of inlet pressures. The factor was then used to calculate expected flow at 100 PSIG. Cv values were calculated by graphing the flow (scfm) versus the square root of change in pressure across the valve. A line was fitted to this graph and the resulting slope is the Cv value. Cv uses the theoretical flow (scfm) through the valve when the differential pressure between the inlet and outlet is equal to 1 psi. **We have never lost an application based on either flow or durability.**

Rated Flow

Body Style	2	3	4	6*	8*	12*
Port Size	1/4"	3/8"	1/2"	3/4"	1"	1-1/2"
SCFM Flow	73.9	97.1	215.0	446.9	477.7	1627
Cv Factor	1.6	2.4	5.0	10.4	11.1	37.8

*Tested before the published ISO standards. Cv's were calculated using previous data.

SCFM flow in the above table was calculated for 70 PSIG then converted to 100 PSIG (114.7 PSIA) inlet pressure. At other inlet pressures, SCFM flow will be in proportion to PSIA inlet pressure.

Example: Size 3P at 80 PSIG (94.7 PSIA) inlet pressure.
Ratio of 94.7 to 114.7 is 94.7 ÷ 114.7 = 0.826
Flow at 80 PSIG = 0.826 x 97.1 = 80.2 SCFM.

RESPONSE TIME. With the valve initially shifted to communicate 150 psi inlet pressure to a blocked cylinder port the total elapsed shifting time was measured between the instant of energization of the opposite solenoid and build up of 90% of full steady state flow in the other cylinder port, which was vented to atmosphere. The result is a measure of the "Blocked to Open Shift Time".

In another test, with the valve initially shifted to a port which was vented to atmosphere, the total elapsed time was measured between the instant of energization of the opposite solenoid and build-up of 90% of full steady state pressure in the other cylinder port which was blocked. The result is a measure of "Open to Blocked Shift Time":

Response Times in Milliseconds

Body Style	2	3	4	6	8	12
Blocked*	91.0	95.0	74.2	147	147	147
Open†	80.0	67.5	67.5	152	170	105

*Blocked to Open response time.
†Open to Blocked response time.

These test were made over a range of 50 to 150 psi.

The shifting time is quite satisfactory for almost all applications, but for faster response a larger orifice can be supplied on special order.

Appendix D: Thruster SPICE Model

```
THRUSTER
Cbank     1    0          0.115 IC=700
R         1    2          0.001
L         2    3          11uH IC=0
Rarc      3    4          733u

E1dummy   100  0          VALUE =
    {(I(E1)*I(E1)*I(E1)*2.02*10^-13)/(5.64*10^-4)}
E2dummy   200  0          VALUE =
    {(I(E1)*I(E1)*I(E1)*2.02*10^-13)/(5.64*10^-
    4+(3.07*10^-7)*(abs(I(E1))-1400))}
E1        4    5          VALUE = { if
    ((I(E1)<1400),V(100),V(200))}
Earc 5    0          TABLE {I(Earc)}= -1m -27 1m 27

Ef        10   0          VALUE = {2.01*10^-
    7*I(Earc)*I(Earc)}
Rmass     10   0          4

Gforce    0    20         VALUE = {V(10)}
Cforce    20   0          1 IC=0
Rdummy    20   0          1G

.PROBE
.TRAN 0 7m 0 1u UIC
.END
```

Appendix E: Inductance Sweep SPICE Model

```
THRUSTER
Cbank  1       0              0.115 IC=700
R              1       2             0.001
L              2       3              LMOD 1 IC=0
.MODEL     LMOD         IND(L=1u)
.STEP  IND    LMOD(L)      0u,100u,20u

Rarc   3       4              733u

E1dummy     100    0              VALUE={(I(E1)*I(E1)*I(E1)*2.02*10^-
13)/(5.64*10^-4)}
E2dummy     200    0              VALUE={(I(E1)*I(E1)*I(E1)*2.02*10^-
13)/(5.64*10^-4+(3.07*10^-7)*(abs(I(E1))-1400))}
E1             4       5              VALUE={if ((I(E1)<1400),V(100),V(200))}

Earc   5       0              TABLE {I(Earc)}= -1m -27 1m 27

Ef             10     0              VALUE = {2.01*10^-7*I(Earc)*I(Earc)}
Rmass 10      0              4

Gforce 0      20             VALUE = {V(10)}
Cforce 20     0              1 IC=0
Rdummy      20     0              1G

.PROBE
.TRAN 0 25m 0 1u UIC
.END
```

References

[1] R. G. Jahn, *Physics of Electric Propulsion*, Mineola: Dover Publications, Inc., 2006, pp. 3

[2] R. G. Jahn, *Physics of Electric Propulsion*, Mineola: Dover Publications, Inc., 2006, pp. 3

[3] Wikipedia, "Delta-V", January 2007, http://en.wikipedia.org/wiki/Delta_v.

[4] R. G. Jahn, *Physics of Electric Propulsion*, Mineola: Dover Publications, Inc., 2006, pp. 4

[5] R. G. Jahn, *Physics of Electric Propulsion*, Mineola: Dover Publications, Inc., 2006, pp. 4

[6] R. A. Braeunig, "Rocket Propellants", December 2007, http://www.braeunig.us/space/propel.htm.

[7] R. G. Jahn, *Physics of Electric Propulsion*, Mineola: Dover Publications, Inc., 2006, pp. 5

[8] R. G. Jahn, *Physics of Electric Propulsion*, Mineola: Dover Publications, Inc., 2006, pp. 9

[9] J. D. Cobine, *Gaseous Conductors*, New York: McGraw-Hill Book Company, Inc., pp. 9

[10] J. D. Cobine, *Gaseous Conductors*, New York: McGraw-Hill Book Company, Inc., pp. 8

[11] J. D. Cobine, *Gaseous Conductors*, New York: McGraw-Hill Book Company, Inc., pp. 8

[12] J. D. Cobine, *Gaseous Conductors*, New York: McGraw-Hill Book Company, Inc., pp. 13

[13] J. D. Cobine, *Gaseous Conductors*, New York: McGraw-Hill Book Company, Inc., pp. 18

[14] J. D. Cobine, *Gaseous Conductors*, New York: McGraw-Hill Book Company, Inc., pp. 18

[15] J. D. Cobine, *Gaseous Conductors*, New York: McGraw-Hill Book Company, Inc., pp. 18

[16] J. D. Cobine, *Gaseous Conductors*, New York: McGraw-Hill Book Company, Inc., pp. 17

[17] Department of Chemistry, Colby College, "The Dissociation Energy of Halogen Gasses", December 2006, http://www.colby.edu/chemistry/PChem/lab/DissEI2Br2.pdf.

[18] Wikipedia, "Nitrogen", December 2006, http://en.wikipedia.org/wiki/Nitrogen.

[19] Department of Physics, Georgia Tech University, "Atomic Energy Level Diagrams", http://hyperphysics.phy-astr.gsu.edu/hbase/atomic/grotrian.html.

[20] R. G. Jahn, *Physics of Electric Propulsion*, Mineola: Dover Publications, Inc., 2006, pp. 47

[21] R. G. Jahn, *Physics of Electric Propulsion*, Mineola: Dover Publications, Inc., 2006, pp. 31

[22] R. G. Jahn, *Physics of Electric Propulsion*, Mineola: Dover Publications, Inc., 2006, pp. 31

[23] R. G. Jahn, *Physics of Electric Propulsion*, Mineola: Dover Publications, Inc., 2006, pp. 31

[24] R. G. Jahn, *Physics of Electric Propulsion*, Mineola: Dover Publications, Inc., 2006, pp. 33

[25] R. G. Jahn, *Physics of Electric Propulsion*, Mineola: Dover Publications, Inc., 2006, pp. 33

[26] R. G. Jahn, *Physics of Electric Propulsion*, Mineola: Dover Publications, Inc., 2006, pp. 33

[27] J. D. Cobine, *Gaseous Conductors*, New York: McGraw-Hill Book Company, Inc., pp. 20

[28] Wikipedia, "Argon", December 2006, http://en.wikipedia.org/wiki/Argon

[29] J. D. Cobine, *Gaseous Conductors*, New York: McGraw-Hill Book Company, Inc., pp. 20

[30] J. D. Cobine, *Gaseous Conductors*, New York: McGraw-Hill Book Company, Inc., pp. 21

[31] J. D. Cobine, *Gaseous Conductors*, New York: McGraw-Hill Book Company, Inc., pp. 21

[32] J. D. Cobine, *Gaseous Conductors*, New York: McGraw-Hill Book Company, Inc., pp. 23

[33] J. D. Cobine, *Gaseous Conductors*, New York: McGraw-Hill Book Company, Inc., pp. 24

[34] R. G. Jahn, *Physics of Electric Propulsion*, Mineola: Dover Publications, Inc., 2006, pp. 35

[35] R. G. Jahn, *Physics of Electric Propulsion*, Mineola: Dover Publications, Inc., 2006, pp. 35

[36] R. G. Jahn, *Physics of Electric Propulsion*, Mineola: Dover Publications, Inc., 2006, pp. 35

[37] R. G. Jahn, *Physics of Electric Propulsion*, Mineola: Dover Publications, Inc., 2006, pp. 35

[38] R. G. Jahn, *Physics of Electric Propulsion*, Mineola: Dover Publications, Inc., 2006, pp. 35

[39] Wikipedia, "Planck's Constant", December 2006, http://en.wikipedia.org/wiki/Planck's_constant.

[40] R. G. Jahn, *Physics of Electric Propulsion*, Mineola: Dover Publications, Inc., 2006, pp. 35

[41] R. G. Jahn, *Physics of Electric Propulsion*, Mineola: Dover Publications, Inc., 2006, pp. 36

[42] R. G. Jahn, *Physics of Electric Propulsion*, Mineola: Dover Publications, Inc., 2006, pp. 36

[43] R. G. Jahn, *Physics of Electric Propulsion*, Mineola: Dover Publications, Inc., 2006, pp. 36

[44] R. G. Jahn, *Physics of Electric Propulsion*, Mineola: Dover Publications, Inc., 2006, pp. 36

[45] R. G. Jahn, *Physics of Electric Propulsion*, Mineola: Dover Publications, Inc., 2006, pp. 36

[46] R. G. Jahn, *Physics of Electric Propulsion*, Mineola: Dover Publications, Inc., 2006, pp. 36

[47] R. G. Jahn, *Physics of Electric Propulsion*, Mineola: Dover Publications, Inc., 2006, pp. 36

[48] R. G. Jahn, *Physics of Electric Propulsion*, Mineola: Dover Publications, Inc., 2006, pp. 37

[49] R. G. Jahn, *Physics of Electric Propulsion*, Mineola: Dover Publications, Inc., 2006, pp. 37

[50] R. G. Jahn, *Physics of Electric Propulsion*, Mineola: Dover Publications, Inc., 2006, pp. 37

[51] R. G. Jahn, *Physics of Electric Propulsion*, Mineola: Dover Publications, Inc., 2006, pp. 38

[52] J. D. Cobine, *Gaseous Conductors*, New York: McGraw-Hill Book Company, Inc., pp. 107

[53] J. D. Cobine, *Gaseous Conductors*, New York: McGraw-Hill Book Company, Inc., pp. 107

[54] J. D. Cobine, *Gaseous Conductors*, New York: McGraw-Hill Book Company, Inc., pp. 116

[55] J. D. Cobine, *Gaseous Conductors*, New York: McGraw-Hill Book Company, Inc., pp. 117

[56] J. D. Cobine, *Gaseous Conductors*, New York: McGraw-Hill Book Company, Inc., pp. 118

[57] J. D. Cobine, *Gaseous Conductors*, New York: McGraw-Hill Book Company, Inc., pp. 143

[58] J. D. Cobine, *Gaseous Conductors*, New York: McGraw-Hill Book Company, Inc., pp. 144

[59] J. D. Cobine, *Gaseous Conductors*, New York: McGraw-Hill Book Company, Inc., pp. 213

[60] J. D. Cobine, *Gaseous Conductors*, New York: McGraw-Hill Book Company, Inc., pp. 213

[61] J. D. Cobine, *Gaseous Conductors*, New York: McGraw-Hill Book Company, Inc., pp. 213

[62] J. D. Cobine, *Gaseous Conductors*, New York: McGraw-Hill Book Company, Inc., pp. 213

[63] J. D. Cobine, *Gaseous Conductors*, New York: McGraw-Hill Book Company, Inc., pp. 215

[64] J. D. Cobine, *Gaseous Conductors*, New York: McGraw-Hill Book Company, Inc., pp. 290

[65] J. D. Cobine, *Gaseous Conductors*, New York: McGraw-Hill Book Company, Inc., pp. 317

[66] J. D. Cobine, *Gaseous Conductors*, New York: McGraw-Hill Book Company, Inc., pp. 291

[67] J. D. Cobine, *Gaseous Conductors*, New York: McGraw-Hill Book Company, Inc., pp. 293

[68] J. D. Cobine, *Gaseous Conductors*, New York: McGraw-Hill Book Company, Inc.,

pp. 294

[69] J. D. Cobine, *Gaseous Conductors*, New York: McGraw-Hill Book Company, Inc., pp. 299

[70] J. D. Cobine, *Gaseous Conductors*, New York: McGraw-Hill Book Company, Inc., pp. 299

[71] J. D. Cobine, *Gaseous Conductors*, New York: McGraw-Hill Book Company, Inc., pp. 302

[72] J. D. Cobine, *Gaseous Conductors*, New York: McGraw-Hill Book Company, Inc., pp. 302

[73] J. D. Cobine, *Gaseous Conductors*, New York: McGraw-Hill Book Company, Inc., pp. 302

[74] J. D. Cobine, *Gaseous Conductors*, New York: McGraw-Hill Book Company, Inc., pp. 302

[75] J. D. Cobine, *Gaseous Conductors*, New York: McGraw-Hill Book Company, Inc., pp. 303

[76] J. D. Cobine, *Gaseous Conductors*, New York: McGraw-Hill Book Company, Inc., pp. 304

[77] J. D. Cobine, *Gaseous Conductors*, New York: McGraw-Hill Book Company, Inc., pp. 306

[78] J. D. Cobine, *Gaseous Conductors*, New York: McGraw-Hill Book Company, Inc., pp. 335

[79] J. D. Cobine, *Gaseous Conductors*, New York: McGraw-Hill Book Company, Inc., pp. 343

[80] J. D. Cobine, *Gaseous Conductors*, New York: McGraw-Hill Book Company, Inc., pp. 343

[81] J. D. Cobine, *Gaseous Conductors*, New York: McGraw-Hill Book Company, Inc., pp. 343

[82] J. D. Cobine, *Gaseous Conductors*, New York: McGraw-Hill Book Company, Inc., pp. 344

[83] R. G. Jahn, *Physics of Electric Propulsion*, Mineola: Dover Publications, Inc., 2006, pp. 69

[84] R. G. Jahn, *Physics of Electric Propulsion*, Mineola: Dover Publications, Inc., 2006, pp. 69

[85] R. G. Jahn, *Physics of Electric Propulsion*, Mineola: Dover Publications, Inc., 2006, pp. 70

[86] R. G. Jahn, *Physics of Electric Propulsion*, Mineola: Dover Publications, Inc., 2006, pp. 70

[87] R. G. Jahn, *Physics of Electric Propulsion*, Mineola: Dover Publications, Inc., 2006, pp. 72

[88] R. G. Jahn, *Physics of Electric Propulsion*, Mineola: Dover Publications, Inc., 2006, pp. 72

[89] R. G. Jahn, *Physics of Electric Propulsion*, Mineola: Dover Publications, Inc., 2006, pp. 73

[90] R. G. Jahn, *Physics of Electric Propulsion*, Mineola: Dover Publications, Inc., 2006, pp. 71

[91] R. G. Jahn, *Physics of Electric Propulsion*, Mineola: Dover Publications, Inc., 2006, pp. 72

[92] R. G. Jahn, *Physics of Electric Propulsion*, Mineola: Dover Publications, Inc., 2006, pp. 74

[93] R. G. Jahn, *Physics of Electric Propulsion*, Mineola: Dover Publications, Inc., 2006, pp. 74

[94] R. G. Jahn, *Physics of Electric Propulsion*, Mineola: Dover Publications, Inc., 2006, pp. 75

[95] R. G. Jahn, *Physics of Electric Propulsion*, Mineola: Dover Publications, Inc., 2006, pp. 75

[96] R. G. Jahn, *Physics of Electric Propulsion*, Mineola: Dover Publications, Inc., 2006, pp. 75

[97] R. G. Jahn, *Physics of Electric Propulsion*, Mineola: Dover Publications, Inc., 2006, pp. 76

[98] R. G. Jahn, *Physics of Electric Propulsion*, Mineola: Dover Publications, Inc., 2006, pp. 76

[99] R. G. Jahn, *Physics of Electric Propulsion*, Mineola: Dover Publications, Inc., 2006, pp. 76

[100] R. G. Jahn, *Physics of Electric Propulsion*, Mineola: Dover Publications, Inc., 2006, pp. 77

[101] R. G. Jahn, *Physics of Electric Propulsion*, Mineola: Dover Publications, Inc., 2006, pp. 77

[102] R. G. Jahn, *Physics of Electric Propulsion*, Mineola: Dover Publications, Inc., 2006, pp. 77

[103] R. G. Jahn, *Physics of Electric Propulsion*, Mineola: Dover Publications, Inc., 2006, pp. 92

[104] R. G. Jahn, *Physics of Electric Propulsion*, Mineola: Dover Publications, Inc., 2006, pp. 91

[105] R. G. Jahn, *Physics of Electric Propulsion*, Mineola: Dover Publications, Inc., 2006, pp. 92

[106] R. G. Jahn, *Physics of Electric Propulsion*, Mineola: Dover Publications, Inc., 2006, pp. 197

[107] R. G. Jahn, *Physics of Electric Propulsion*, Mineola: Dover Publications, Inc., 2006, pp. 197

[108] R. G. Jahn, *Physics of Electric Propulsion*, Mineola: Dover Publications, Inc., 2006, pp. 197

[109] R. G. Jahn, *Physics of Electric Propulsion*, Mineola: Dover Publications, Inc., 2006, pp. 200

[110] R. G. Jahn, *Physics of Electric Propulsion*, Mineola: Dover Publications, Inc., 2006, pp. 200

[111] R. G. Jahn, *Physics of Electric Propulsion*, Mineola: Dover Publications, Inc., 2006, pp. 201

[112] R. G. Jahn, *Physics of Electric Propulsion*, Mineola: Dover Publications, Inc., 2006, pp. 203

[113] R. G. Jahn, *Physics of Electric Propulsion*, Mineola: Dover Publications, Inc.,

2006, pp. 203

[114] R. G. Jahn, *Physics of Electric Propulsion*, Mineola: Dover Publications, Inc., 2006, pp. 203

[115] R. G. Jahn, *Physics of Electric Propulsion*, Mineola: Dover Publications, Inc., 2006, pp. 204

[116] R. G. Jahn, *Physics of Electric Propulsion*, Mineola: Dover Publications, Inc., 2006, pp. 205

[117] R. G. Jahn, *Physics of Electric Propulsion*, Mineola: Dover Publications, Inc., 2006, pp. 205

[118] R. G. Jahn, *Physics of Electric Propulsion*, Mineola: Dover Publications, Inc., 2006, pp. 205

[119] R. G. Jahn, *Physics of Electric Propulsion*, Mineola: Dover Publications, Inc., 2006, pp. 205

[120] R. G. Jahn, *Physics of Electric Propulsion*, Mineola: Dover Publications, Inc., 2006, pp. 232

[121] R. G. Jahn, *Physics of Electric Propulsion*, Mineola: Dover Publications, Inc., 2006, pp. 228

[122] R. G. Jahn, *Physics of Electric Propulsion*, Mineola: Dover Publications, Inc., 2006, pp. 230

[123] R. G. Jahn, *Physics of Electric Propulsion*, Mineola: Dover Publications, Inc., 2006, pp. 231

[124] R. G. Jahn, *Physics of Electric Propulsion*, Mineola: Dover Publications, Inc., 2006, pp. 231

[125] R. G. Jahn, *Physics of Electric Propulsion*, Mineola: Dover Publications, Inc., 2006, pp. 231

[126] R. G. Jahn, *Physics of Electric Propulsion*, Mineola: Dover Publications, Inc., 2006, pp. 235

[127] R. G. Jahn, *Physics of Electric Propulsion*, Mineola: Dover Publications, Inc., 2006, pp. 238

[128] R. G. Jahn, *Physics of Electric Propulsion*, Mineola: Dover Publications, Inc., 2006, pp. 241

[129] R. G. Jahn, *Physics of Electric Propulsion*, Mineola: Dover Publications, Inc., 2006, pp. 241

[130] R. G. Jahn, *Physics of Electric Propulsion*, Mineola: Dover Publications, Inc., 2006, pp. 241

[131] R. G. Jahn, *Physics of Electric Propulsion*, Mineola: Dover Publications, Inc., 2006, pp. 241

[132] R. G. Jahn, *Physics of Electric Propulsion*, Mineola: Dover Publications, Inc., 2006, pp. 241

[133] R. G. Jahn, *Physics of Electric Propulsion*, Mineola: Dover Publications, Inc., 2006, pp. 242

[134] R. G. Jahn, *Physics of Electric Propulsion*, Mineola: Dover Publications, Inc., 2006, pp. 243

[135] R. G. Jahn, *Physics of Electric Propulsion*, Mineola: Dover Publications, Inc., 2006, pp. 242

[136] R. G. Jahn, *Physics of Electric Propulsion*, Mineola: Dover Publications, Inc., 2006, pp. 243

[137] R. G. Jahn, *Physics of Electric Propulsion*, Mineola: Dover Publications, Inc., 2006, pp. 243

[138] R. G. Jahn, *Physics of Electric Propulsion*, Mineola: Dover Publications, Inc., 2006, pp. 243

[139] R. G. Jahn, *Physics of Electric Propulsion*, Mineola: Dover Publications, Inc., 2006, pp. 243

[140] R. G. Jahn, *Physics of Electric Propulsion*, Mineola: Dover Publications, Inc., 2006, pp. 244

[141] R. G. Jahn, *Physics of Electric Propulsion*, Mineola: Dover Publications, Inc., 2006, pp. 241

[142] R. G. Jahn, *Physics of Electric Propulsion*, Mineola: Dover Publications, Inc., 2006, pp. 246

[143] R. G. Jahn, *Physics of Electric Propulsion*, Mineola: Dover Publications, Inc., 2006, pp. 246

[144] R. G. Jahn, *Physics of Electric Propulsion*, Mineola: Dover Publications, Inc., 2006, pp. 247

[145] R. G. Jahn, *Physics of Electric Propulsion*, Mineola: Dover Publications, Inc., 2006, pp. 247

[146] M. T. Thompson, "Inductance Calculation Techniques – Part II: Approximations and Handbook Methods", *PCIM*, December 1999.

[147] PowerStream Technologies, "Wire Gauge and Current Limits", February 2007, http://www.powerstream.com/Wire_Size.htm.

[148] R. G. Jahn, *Physics of Electric Propulsion*, Mineola: Dover Publications, Inc., 2006, pp. 244

[149] J. D. Cobine, *Gaseous Conductors*, New York: McGraw-Hill Book Company, Inc., pp. 303

[150] J. D. Cobine, *Gaseous Conductors*, New York: McGraw-Hill Book Company, Inc., pp. 303

[151] R. G. Jahn, *Physics of Electric Propulsion*, Mineola: Dover Publications, Inc., 2006, pp. 30

[152] J. D. Cobine, *Gaseous Conductors*, New York: McGraw-Hill Book Company, Inc., pp. 299

[153] J. D. Cobine, *Gaseous Conductors*, New York: McGraw-Hill Book Company, Inc., pp. 294

[154] J. J. Lowke, R. Morrow, J. Haidar, *A. B. Murphy, Prediction of Gas Tungsten Arc Welding Properties in Mixtures of Argon and Hydrogen*, IEEE TRANSACTIONS ON PLASMA SCIENCE, VOL. 25, NO. 5, OCTOBER 1997

[155] Wikipedia, "Argon", December 2006, http://en.wikipedia.org/wiki/Argon

[156] Department of Physics, Georgia Tech University, "Speed of Sound in Air", http://hyperphysics.phy-astr.gsu.edu/hbase/sound/souspe.html.

[157] J. J. Lowke, R. Morrow, J. Haidar, *A. B. Murphy, Prediction of Gas Tungsten Arc Welding Properties in Mixtures of Argon and Hydrogen*, IEEE TRANSACTIONS ON PLASMA SCIENCE, VOL. 25, NO. 5, OCTOBER 1997

[158] T. K. Bose, *High Temperature Gas Dynamics*, Berkely: Springer, 2004, pp 161-

162.

[159] J. D. Cobine, *Gaseous Conductors*, New York: McGraw-Hill Book Company, Inc.,
pp. 109

[160] Valve Catalog #28, Complete Air Valve Catalog, AAA Products International,
Dallas Texas.